OBSERVATIONS OF THE SUNYAEV-ZEL'DOVICH EFFECT TOWARDS CLUSTERS OF GALAXIES WITH THE APEX TELESCOPE

Dissertation
zur
Erlangung des Doktorgrades (Dr. rer. nat.)
der
Mathematisch-Naturwissenschaftlichen Fakultät
der
Rheinischen Friedrich-Wilhelms-Universität Bonn

vorgelegt von
Martin Nord
aus
Helsingborg, Schweden

Bonn, 2009

Angefertigt mit Genehmigung
der Mathematisch-Naturwissenschaftlichen Fakultät
der Rheinischen Friedrich-Wilhelms-Universität Bonn

1. Gutachter:	Prof. Dr. Frank Bertoldi
2. Gutachter:	Prof. Dr. Karl Menten

Tag der Mündlichen Prüfung: 21. August 2009
Erscheinungsjahr: 2009

Abstract

Results of 150 GHz continuum observations of several X-ray bright clusters of galaxies in the Sunyaev-Zel'dovich (SZ) effect, carried out using the APEX-SZ bolometer array on the APEX telescope, are presented. Follow-up observations of the cluster A2163 with the Large APEX Bolometer Camera (LABOCA) at 345 GHz on the same telescope have been carried out, yielding the largest map of a cluster of galaxies in the SZ increment to date.

Details of possible contaminants affecting the SZ signal are outlined, and a simulated galaxy cluster survey is used to estimate levels of contamination from each source of emission. In agreement with previous studies it is found that primary CMB anisotropies are a weak source of contamination for SZ observations of distant clusters, although massive nearby clusters can be severely contaminated. Radio point sources are found to be of possible concern, but more information on spectral slopes in the millimeter regime is needed before any decisive conclusions can be made. It is found that treating unresolved thermal sources as a source of excess noise yields an excellent approximation of this contaminant, which sets a fundamental confusion limit on single-frequency SZ measurements.

The 1.4 GHz volume averaged radio source luminosity function is constructed from a large sample of galaxy clusters. In contrast to previous studies, an adaptive cluster volume is used to construct the luminosity function. This is shown to yield more robust results on volume averaged source counts, and for the first time a redshift evolution in this luminosity function is found, taking into account the variable effect on radio source confusion with redshift. Due to the large sample size, luminosity evolution and number density evolution can be separated, and it is found that the average luminosity scales with the redshift parameter z as $(1 + z)^{3.3\pm1.2}$, and the number density as $(1 + z)^{2.8\pm0.9}$.

The APEX-SZ and LABOCA instruments are described from an observer's perspective. The analyses of pointing and calibration data are described, and the data quality of each instrument is assessed. The reduction of galaxy cluster data is described in detail, including the steps of time stream reduction, involving the removal of correlated atmospheric noise, and mapping. Losses in source brightness due to the removal of correlated noise are modeled with a transfer function based on the reduction of a point source convolved with the instrument beam. It is shown that this approach is valid for a wide range of source morphologies provided the reduction is done within a set of certain well-defined steps.

Significant detections of 9 clusters of galaxies with APEX-SZ are presented. The clusters are modeled using the well-known isothermal β model, which proves to be sufficient in most cases due to the relatively low significance compared to state-of-the-art X-ray measurements. The SZ signals are found to be in overall agreement with predictions from X-ray measurements. As expected, the isothermal pressure profiles from the SZ measurements are broader than the surface brightness profiles from X-ray experiments.

The possibility of simultaneously extracting gas temperatures and bulk velocities from SZ measurements is briefly discussed. It is found that current data have poor leverage on the problem; reasonable constraints require accurate measurements both at high frequencies ($\gtrsim$ 300 GHz), where confusion due to dust emission becomes increasingly more of a problem, and at low frequencies ($\lesssim$ 90 GHz), where radio point sources can contaminate the signal.

A non-isothermal model of the galaxy cluster A2163 is presented, based on APEX-SZ and XMM-Newton X-ray data. Under the assumption of spherical symmetry, the two data sets are used to de-project the structure of the cluster in terms of temperature and density, and the results are used to derive the gas mass profile. The total mass profile is derived under the assumption of hydrostatic equilibrium, to allow for an estimate of the gas mass fraction. It is shown that the isothermal approximation well approximates the non-isothermal model inside the X-ray core radius, where the mean gas temperature derived from the SZ/X-ray joint analysis is 9.6 ± 0.3 keV. The mass profile from the non-isothermal analysis is in agreement with weak lensing measurements. The APEX-SZ data is also used, in conjunction with LABOCA data at 345 GHz and previously published SZ data at other frequencies, to constrain the central Comptonization and bulk velocity of the cluster, using priors on the temperature of the intra-cluster gas. A line-of-sight peculiar velocity of -140 ± 460 km/s and a central Comptonization of $(3.42 \pm 0.32) \times 10^{-4}$ are found for Abell 2163.

Acknowledgments

This PhD thesis was completed at the Argelander-Institut für Astronomie in Bonn. During the first three years of my graduate studies I was supported by a stipend from the International Max Planck Research School (IMPRS) for Radio and Infrared Astronomy at the Universities of Bonn and Cologne, while during the last 10 months I was supported by a stipend from the University of Bonn. Proprietary data used in this thesis come from the APEX-SZ and LABOCA bolometer arrays on the APEX telescope, a collaboration between the Max-Planck-Institut für Radioastronomie, the European Southern Observatory, and the Onsala Space Observatory. APEX-SZ is funded by the National Science Foundation (USA) under Grant No. AST-0138348.

Parts of the work presented here have been developed in collaboration with others. In particular, much of the research laid out in chapters 4 and 9 has been conducted in close collaboration with Kaustuv Basu. Much of the material in chapters 5 and 6 has been inspired by discussions with other members of the APEX-SZ collaboration (too numerous to list) although it reflects solely my own work where not explicitly stated otherwise.

I am grateful to my supervisor, Frank Bertoldi, and to my second referee, Karl Menten, for their support during my time as a graduate student at AIfA. I have had the great fortune of sharing an office with my friend and colleague Kaustuv Basu, who has often been my de facto thesis advisor. It is no exaggeration to state that this thesis, in its present form, would not have been possible without him. Thanks also to Axel Weiss for providing calibration tables for 345 GHz continuum observations and to Fred Schuller for helping with LABOCA data taking. On the administrative side of things, I am grateful to Christina Stein-Schmitz, Gabi Breuer and Eduardo Ros.

I am much indebted to those who have taken the time to comment on the draft of this thesis (or parts thereof), in particular Frank Bertoldi, Karl Menten, Kaustuv Basu, Kirsten Kraiberg Knudsen and Cathy Horellou. Scientific as well as extra-curricular discussions with my old friend Daniel Johansson are likewise gratefully acknowledged.

I would like to thank Manuel ("Pågen") Aravena for many enjoyable sessions in the AIfA "beer cellar", for discussions in the coffee room, covering a wide dynamic range of seriousness, and for other things too numerous (or inappropriate) to mention. I shall never forget Klagenfurt. I thank Alexandre Beelen for patiently introducing me to bolometer array data reduction, for teaching me the correct pronunciation of *pardon*, and for sharing countless rounds of Weissbier with me in the "Biergarten". *Il existe près des écluses.*

I don't think I would have survived without my family. Lena and Anni-Lotta, thanks for putting up with and supporting a sometimes grumpy boyfriend and father. You are both more important than galaxies, even whole clusters of them. I am deeply grateful to my parents, Karin and Göran, for always having encouraged me to pursue my interests. I would not have been here (or anywhere else) without you.

Bonn, May 2009 Martin Nord

Contents

Chapter 1

Introduction

Predicted by Alpher, Bethe & Gamow (1958) and detected by Penzias & Wilson (1965), the cosmic microwave background (CMB) and its analysis have emerged as one of the most useful tools in observational cosmology. This relict radiation from the Big Bang, imprinted with information from the early universe (e.g. Partridge 1995), is a powerful resource in probing the structure and composition of the Universe. In recent years, observations of the CMB have seen a fast increase in precision with the development of high resolution/sensitivity observing techniques for millimeter waves. On large angular scales (on the order of degrees), the CMB gives information about the geometry of the universe, while on intermediate scales it yields insights into its thermal history and probes the distribution and energy contribution of the mysterious dark matter and dark energy (e.g. Peebles & Ratra 2003, Coles & Luccin 2002), which together are believed to make up most of the energy in the present observable universe.

Technical breakthroughs in the last two decades now allow the study of the CMB down to scales comparable to and smaller than the angular scales subtented by clusters of galaxies. Galaxy clusters have been studied for decades in optical light and in X-rays, but only since very recently do we have the tools to study them through their imprint on the CMB with high precision. This imprint owes to the effect of inverse Compton scattering of CMB photons on intra-cluster gas. Known as the Sunyaev-Zel'dovich (SZ) effect (Sunyaev & Zel'dovich 1970), it has the compelling property of being independent of cosmological redshift (e.g. Carlstrom, Holder & Reese 2002). By studying galaxy clusters in the SZ effect, it is thus possible to probe the evolution of such systems. Many cosmological parameters − such as the mass density and the normalization of the matter power spectrum − can be constrained through number counts of clusters at different redshifts (e.g. Holder et al. 2001, Battye & Weller 2003). In particular, such constraints are independent of and complementary to other cosmological tools (see, e.g., Voit 2004 for an overview), such as the study of supernovae (Perlmutter et al. 1999, Knop et al. 2003, Astier et al. 2006) and the study of primary CMB anisotropies (Fixsen et al. 1996, Bennett et al. 1992, Spergel et al. 2003, Komatsu et al. 2008).

The APEX-SZ project (Schwan et al. 2003, Dobbs et al. 2006), employing a bolometer camera operating at 150 GHz on the APEX telescope (Güsten et al. 2006) at the high altitude site of Llano Chajnantor in Chile, was originally planned as an experiment to deeply map around 100 square degrees of the sky in the SZ effect and extract cosmological information (Schwan et al. 2003). At present, the sensitivity of the instrument does not meet the original design goals, and awaiting an update of the bolometer array the goals of the experiment have had to be somewhat revised. Although a deep survey is ongoing, the APEX-SZ camera is at present mainly used to make deep images of clusters of galaxies well known from other parts of the electromagnetic spectrum (e.g. Halverson et al. 2008, Nord et al. 2009). Such studies are very important in order to understand the detailed physics of clusters; in particular to constrain the relationship between mass, temperature and luminosity, which will become crucial in normalizing the results of future "blind" SZ surveys. High resolution studies furthermore make possible a detailed modeling of the intra-cluster medium (ICM), revealing information on cluster evolution and the processes involved in cluster mergers (Myers et al. 1997, Birkinshaw 1999).

This thesis presents the results of the first two years of observations with APEX-SZ. It furthermore outlines the possible sources of astrophysical contamination affecting SZ observations. The APEX-SZ project is a collaboration of several North American institutes[1], two German institutes[2] and one Swedish partner[3]. While the instrument was designed and built by the North American collaborators, observations and the reduction and analysis of data are co-operative efforts involving all partners. Two analysis pipelines have been developed, one of which is described in detail in this thesis. Extensive comparisons have been made between the two pipelines, and they now produce consistent results. This work focuses on describing the different steps in that analysis and on the results achieved with it. Only a limited account is given of comparisons between the two analyses. The software and analysis tools described in chapter 6 of this thesis are thus very much the result of a team effort, and the beginning of that chapter therefore contains a summary of what tools for the data anlysis have been developed/implemented by the author. It should be stressed that the actual analysis described in chapter 6 and later chapters has been carried out by the author unless otherwise stated.

A brief introduction to galaxy clusters is given in chapter 2, where observational properties and ways to estimate cluster masses are discussed. The SZ effect is introduced, and several applications are outlined.

Chapter 3 outlines the different astrophysical components that need to be taken into consideration in the context of SZ observations, in particular when only one frequency band is available. Although this is a quite general problem, it is complicated by factors such as resolution and frequency; thus the discussion centers on confusion problems for the APEX-SZ survey specifically. The APEX-SZ camera is not properly introduced here, but rather in chapter 5. After a general discussion of the most important contaminants, a simulation to constrain the effects of each component is presented.

A basic but crucial first step in understanding how radio source confusion should be statistically dealt with is to study the source density in galaxy cluster environments. In chapter 4, this is done by deriving the so-called luminosity function – the differential number density of sources as a function of spectral luminosity in a given frequency band – in galaxy clusters. The luminosity function is constructed from a large data set at 1.4 GHz (observed frequency), and its dependence on cosmological redshift is investigated.

Chapter 5 describes the APEX-SZ bolometer camera, and in addition the Large APEX Bolometer Camera (LABOCA), also in operation on the APEX telescope. LABOCA has been used to make a high resolution map of the galaxy cluster Abell 2163 (chapter 9). Both instruments are described from the point of view of an observer, bypassing most technical details and focusing on the basic use of the instruments and on their data. Data reduction techniques are described in chapter 6. The removal of correlated atmospheric noise is discussed, as well as the effects of different reduction steps on data; in particular the attenuation of source signals due to the removal of correlated noise. A way to model the filter function of a pipeline

---

[1] The University of California at Berkeley, the University of Colorado at Boulder, and McGill University (Montreal)

[2] The Max Planck Institute for Radioastronomy and the Argelander Institute for Astronomy, both in Bonn

[3] Onsala Space Observatory

reduction (and thereby the attenuation of the source signal) is presented, along with a simple but effective deconvolution algorithm to compensate for the attenuation.

First science results from the APEX-SZ experiment, including the significant detections of nine clusters of galaxies, are presented in chapter 7. Here, a general pipeline reduction scheme is outlined, and isothermal models of the observed clusters are presented.

Chapter 8 discusses how multi-frequency SZ data can be used to recover cluster ICM temperatures and bulk velocities. Present data have poor leverage on this problem, unless priors on the ICM temperature can be obtained. The latter approach is exploited in chapter 9, which discusses the Abell 2163 cluster of galaxies in detail. This cluster has a significant enough detection by APEX-SZ to allow a robust de-projection of the cluster structure, in terms of temperature and density, when combined with XMM-Newton X-ray data. From the derived profiles, gas and total mass estimates are made. Finally, the central ICM temperature thus derived is used as a prior in extracting the cluster peculiar velocity and Comptonization in conjunction with previously published SZ data of this cluster.

A summary and general conclusions are given in chapter 10.

Chapter 2

Clusters of Galaxies and the Sunyaev-Zel'dovich Effect

2.1 Clusters of Galaxies and the Intra-Cluster Medium

2.1.1 Definition

Galaxy clusters are often described as the largest virialized structures or systems in the universe. Although this picture is not incorrect, one may want to include also non-relaxed systems, since the buildup of galaxy clusters is an ongoing hierarchical process with high dynamical complexity. Birkinshaw (1999) thus describes clusters as the most massive *well-differentiated* structures in the universe, which at least for the purpose of this thesis is a more fitting description.

2.1.2 Origin

The origin of clusters of galaxies and other large-scale structures in the universe can be traced back to the early universe. According to the hot big bang model (see, e.g., Coles & Luccin 2002 for a comprehensive treatment), the large-scale structure seen in the present universe originated as over- and under-densities of matter during the epoch of *recombination*, when electrons became bound to nuclei and radiation no longer was in thermal equilibrium with matter. In particular, at the time of *decoupling* (at a redshift $z \simeq 1100$, when the universe was at a temperature of around 3000 K), the mean free path of photons was larger than the Hubble radius – the distance from an observer at which the recession velocity of an object would equal the speed of light.

At the same time that matter density fluctuations became "frozen" as the seeds of the large-scale structure of the present universe, most of the photons making up what is today observed as the cosmic microwave background radiation (CMB) had been scattered by electrons for the last time. One commonly refers to the *surface of last scattering* at this epoch, although this last scattering did not take place at precisely the same cosmological time everywhere.

The CMB was (accidentally) discovered by Penzias and Wilson in 1965, although it had been predicted by Alpher and Gamow long before (Alpher, Bethe & Gamow 1948). It is very close to isotropic, and can be characterized by a blackbody spectrum with a temperature of $T \simeq 2.7$ K. Due to various inhomogeneities in the early universe (and the less interesting fact that we are moving through the preferred rest frame of this radiation field with some proper velocity), it is in fact not *perfectly* isotropic, and this is what makes the CMB such an interesting cosmological probe (see, e.g., White et al. 1994 and Tegmark 1995 for reviews).

One distinguishes between *primary* anisotropies, owing to effects occurring at or before the surface of last scattering, and secondary anisotropies, owing to effects between the surface of last scattering and the observer. Primary anisotropies include the effects of matter over- and under-densities at recombination causing fluctuations in the intensity of the radiation field through gravitational perturbations and thermodynamical fluctuations (Sachs & Wolfe 1967).

The anisotropies in the CMB are very small − even the dipole component (due to our peculiar velocity with respect to the rest frame of the CMB) is only about one part in 10^3 of the mean CMB temperature. The primary anisotropies have a maximum amplitude of about one part in 10^6 of this temperature. This maximum amplitude contrast occurs on spatial scales of around one degree.

As already hinted at above, the galaxy clusters we see in the universe today were built from the seeds of density perturbations at the time of recombination. Interestingly, these structures still cause alterations of the CMB on a very localized scale. The inverse Compton scattering of CMB photons on hot ionized gas in galaxy clusters causes a change in the apparent brightness of the radiation and a slight displacement of the spectrum towards higher frequencies. This is the so-called Sunyaev-Zel'dovich effect, which has emerged as a very powerful cosmological probe as well as a means of studying the physics of galaxy clusters.

2.1.3 Mass

The mass of stars bound in galaxies constitute only a small part of the total baryonic mass of a galaxy cluster − roughly five to ten times as much mass is in the form of hot gas. This so-called intra-cluster medium, or ICM, is the remnant material from the formation of stars and galaxies.

In turn, the total baryonic mass (stars and gas) constitutes only a small fraction of the total cluster mass, since the latter is dominated by dark matter. The baryonic mass fraction depends strongly on cluster dynamics and ranges from about 10 to 30 % (e.g. White & Fabian 1995, Evrard 1997, Allen et al. 2002). The gas mass fraction is comparable to the baryonic mass fraction because the relative mass in stars is low. Moreover, systematic errors in the determination of the latter are comparable to the estimated difference between the gas mass and the total baryonic mass (e.g. David et al. 1995).

Ways to estimate the total cluster mass from observations are described in § 2.1.5 and § 2.1.6.

2.1.4 Temperature

Clusters of galaxies typically have masses in the range $M = 10^{14}$ to $10^{15} M_\odot$ (smaller systems are usually referred to as groups) with effective gravitational radii extending to scales of several Mpc[1].

Intra-cluster gas in hydrostatic equilibrium within the gravitational potential well must obey the equation

$$k_B T_e = \frac{G M m_p}{2 R_{\rm eff}}, \tag{2.1}$$

where $k_B T_e$ is the electron temperature of the ionized intra-cluster gas and $R_{\rm eff}$ is the effective radius. Typically, this temperature is on the order of several keV[2], at which most of the thermal

---

[1] 1 Mpc (megaparsec) = 3.086×10^{22} m.

[2] An energy of 1 keV (kilo electron volt) corresponds to a temperature of 1.16×10^7K.

emission from the gas appears in the X-ray part of the spectrum as thermal bremsstrahlung. Simply put, the intra-cluster gas becomes observable at X-ray wavelengths because the deep potential wells of galaxy clusters compress the gas and heat it to X-ray emitting temperatures.

The X-ray emission is not the only way of observing the intra-cluster gas. Because the ICM is heated and ionized, free electrons can scatter photons of the CMB through inverse Compton scattering. This is known as the Sunyaev-Zel'dovich (SZ) effect (Sunyaev & Zeldovich 1970a,b, Birkinshaw 1999). The cross-section for this process is the Thomson cross section, σ_T, so that the optical depth is given approximately by $\tau_e = n_e \sigma_\mathrm{T} R_\mathrm{eff}$. On average a single scattering produces a relative shift in photon energy proportional to $k_B T_e / m_e c^2$. Both the cross-section and the relative energy shift are on the order of one per cent; thus the overall brightness change of the CMB is about one part in 10^4.

In contrast to the general distribution of the CMB, the SZ effect is localized, and seen only in the directions toward galaxy clusters. In particular, since the effect is linearly sensitive to electron temperature as well as to optical depth (thus tracing line-of-sight integrated pressure), it becomes very concentrated towards dense and hot regions. As described in § 2.2, the SZ effect also has a very distinct frequency dependence, which makes it possible to decouple it from the primary CMB signal by means of multi-frequency observations.

2.1.5 Optical and Infrared Observations

Galaxy clusters can be identified optically through their individual galaxies observed with optical or infrared imaging and/or spectroscopy. Over-densities in space (subtended angle on the sky combined with redshift) indicate the presence of clusters, and assuming that visible light traces the mass distribution in the universe, a first rough cluster mass estimate can be made from the cluster optical luminosity through a so-called richness parameter (e.g. Yee and Ellingson 2003). Because of the redshift, observations in the infrared are more suited for finding very distant clusters.

Galaxy clusters can also be identified through optical photometry, provided that the data is of good enough quality to obtain photometric redshifts (e.g. Bolzonella et al. 2000, Gladders & Yee 2000, 2005). Images from the The Sloan Digital Sky Survey (York et al. 2000) have recently been used to compile the largest catalog of clusters of galaxies to date (Koester et al. 2007); this sample is used in chapter 4 to derive the 1.4 GHz volume averaged radio luminosity function in cluster environments.

Apart from directly relating the optical luminosity to mass (which in any case requires a way of calibrating the scaling), there are two principal ways of determining cluster mass from optical observations; through the distribution of galaxy velocities and through the observation of gravitational lensing.

Cluster velocity dispersions were first measured by Zwicky (1933, 1937), who thereby estimated the mass of the Coma cluster. Mass estimates from velocities are based on the virial theorem, which relates the average total kinetic energy of a stable system, bound by potential forces, to its average total potential energy. The method is thus applicable only to steady, gravitationally bound systems. A further complication arises from the fact that clusters are not isolated systems − there is no well-defined boundary separating a cluster from the cosmic large scale structure. Ways to deal with this problem are described by Carlberg et al. (1997) and by The & White (1986).

The mass of a cluster can also be measured through the lensing of background galaxies within a certain projection radius inside which the contained mass deflects photons toward the line of sight of the observer. Because the shapes of the lensed galaxies are generally unknown, it is necessary to observe a large number of background objects and rely on the assumption that intrinsic deviations from circular symmetry average out. The technique of so-called weak lensing measurements is laid out in many papers, including Tyson et al. (1990), Hoekstra et al. (1998) and Bartelmann & Schneider (2001). Weak-lensing masses are expected to correlate well with optical richness (Voit et al. 2004).

2.1.6 X-ray Observations

As already mentioned, clusters emit in the X-ray domain because they contain intra-cluster gas, which is heated due to infall into a gravitational potential with a resulting adiabatic contraction of the gas. The gas becomes almost fully ionized, emitting bremsstrahlung. The X-ray spectral surface brightness is

$$S_{\mathrm{X}} = \frac{1}{4\pi(1+z)^4} \int n_e \, n_i \, \Lambda_H \, \mathrm{d}l, \tag{2.2}$$

where the integration is along th line of sight, n_e and n_i are the electron and ion densities, respectively, z is the redshift and Λ_H is the so-called X-ray cooling function, which describes the rate at which the ICM radiates energy. The cooling function can be computed under the assumption that the relative abundances of ions are determined by collisional ionization equilibrium (e.g. Sarazin 1988).

If the ICM is in hydrostatic equilibrium, the gravitational forces are balanced by a thermal pressure gradient;

$$\frac{\partial \ln \rho_g}{\partial \ln r} + \frac{\partial \ln T}{\partial \ln r} = -2\frac{T_\phi(r)}{T}, \tag{2.3}$$

where ρ_g is gas density, r is the radial coordinate and $k_B T_\phi(r) = GM(r)\mu m_p/2r$ is the characteristic temperature of a singular isothermal sphere.

Making the additional assumption that the gas is isothermal leads to the so-called beta model, which is discussed in § 2.2.4.

2.2 The Sunyaev-Zel'dovich Effect

2.2.1 The Diffusion Approximation

The Sunyaev-Zel'dovich effect is the inverse Compton scattering of the CMB photons on hot ionized gas in galaxy clusters, causing a change in the apparent brightness of the radiation and a displacement of the spectrum toward the Wien regime (higher frequencies). To a first approximation, the effect can be computed from the Kompaneets equation (Zeldovich & Sunyaev 1969, Sunyaev & Zeldovich 1970, 1972). A relatively simple derivation of the SZ effect in this non-relativistic limit is outlined by Birkinshaw (1999).

The scattering optical depth of the SZ effect is the Compton optical depth, defined by

$$\tau_e = \int n_e \sigma_{\mathrm{T}} \, \mathrm{d}l, \tag{2.4}$$

where the integration is along the line of sight, n_e is the number density of electrons and $\sigma_T = 6.65 \times 10^{-25}\,\mathrm{cm}^2$ is the Thomson cross-section.

To first order, the SZ effect is linearly dependent on the electron temperature and the optical depth. Thus, a useful frequency-independent measure is the *Comptonization parameter*, y, defined by

$$y = \int n_e \sigma_{\mathrm{T}} \frac{k_B T_e}{m_e c^2} \, \mathrm{d}l, \tag{2.5}$$

where T_e is the temperature of the ICM, and k_B, c and m_e are the Boltzmann constant, the speed of light in vacuum and the electron mass, respectively.

In the case that the emission is unresolved (which is often the case in bolometer observations of distant clusters), a useful parameter is the integrated Comptonization

$$Y = D_A^{-2} \int y \, \mathrm{d}A \propto \int n_e T_e \, \mathrm{d}V, \tag{2.6}$$

where the integration is performed over the projected (angular) area of some part of the sky (usually to cover all the SZ emission from a cluster) and D_A is the cosmological angular diameter distance. The integrated Y parameter represents the total thermal energy of the ICM electrons, thus providing a direct way to measure the gas mass. Of course, Y can also be computed for a (partially) resolved cluster observation.

In terms of change of surface brightness, the SZ distortion of the CMB in the direction of a galaxy cluster can be written

$$\frac{\Delta B_\nu}{B_0} = f(x) y, \tag{2.7}$$

where B_0 is a constant factor with the approximate value of 2.7×10^8 Jy/sr.

The frequency-dependent form factor $f(x)$ uses the dimensionless frequency

$$x = \frac{h\nu}{k_B T_0} \tag{2.8}$$

at physical frequency ν and with T_0 the blackbody temperature of the CMB. The frequency dependence is often separated into two parts as $f(x) = g(x)\, h(x)$ with

$$g(x) = x\frac{e^x + 1}{e^x - 1} - 4, \tag{2.9}$$

$$h(x) = \frac{x^4 e^x}{(e^x - 1)^2}, \tag{2.10}$$

which makes it easy to convert between intensity and temperature (the brightness temperature is related to the surface brightness by a factor $h(x)$).

Apart from the thermal effect on the CMB photons, the motion of a cluster with respect to the rest frame of the CMB will result in an additional change of the radiation intensity. For a cluster moving at velocity v_r, this so-called kinematic effect is to first order approximated by (Sunyaev & Zel'dovich 1980a)

$$\frac{\Delta B_\nu^k}{B_0} = -h(x)\frac{v_r}{c}\tau_e, \tag{2.11}$$

where the sign convention is such that a receding cluster has a positive v_r. Assuming small electron temperatures and velocities, ΔB_ν and ΔB_ν^k can be added linearly. Higher order effects, which have yet to be observationally corroborated, are discussed in § 2.2.3.

Figure 2.1 shows the intensity shift of the CMB blackbody spectrum due to the SZ effect. Because of the small magnitude of the effect, it has been magnified by a large factor for clarity. It is evident that the SZ spectrum has two distinct parts: an intensity decrement relative to the primary CMB, below about 220 GHz, and an increment at higher frequencies.

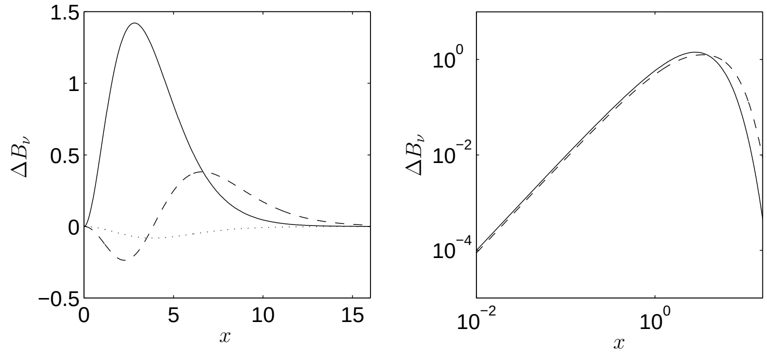

Figure 2.1: Blackbody spectrum of the CMB in units of $(hc)^2/(2(k_BT_0)^3)$ (solid lines), with the SZ spectrum shown for comparison. The dashed line in the left panel shows the thermal effect for $k_BT_e = 5$ keV, while the dotted line shows only the kinematic effect with $v_r = 500$ km/s (receding). The dashed line in the right panel shows the CMB spectrum with the thermal effect added. The SZ intensities have been computed using $\tau = 0.01$ and multiplied with a factor 1000 for clarity.

2.2.2 Temperature and Received Power

From the *intensity* (or intensity distortion) of the SZ effect alone, it is not clear at what frequency or frequencies the effect is detectable with available instruments. Apart from purely astrophysical contaminants (which will be discussed in chapter 3) and atmospheric stability at different frequencies and observing sites, there are many instrument-related factors contributing to the observability of the SZ effect. The following discussion considers single-dish experiments only.

Specific instrument properties are neither easily understood in terms of flux nor in terms of intensity. The flux collected in a telescope beam at a given frequency or in a given frequency range is most naturally described in terms of collected power, corresponding to a change in temperature at the receiver terminals. The noise in the receiver system is readily expressed as a *noise temperature*, since the noise power of a resistor is proportional to its temperature.

The total power available at the receiver terminals scales with the brightness of the source, per unit of solid angle, as

$$P = B_\nu \, \lambda^2 \, \Delta\nu, \tag{2.12}$$

where $\Delta\nu$ is the bandwidth of the observation. This equation explains why it is easier to detect the SZ effect in the decrement than in the increment (Fig. 2.2), disregarding astrophysical contaminants and given a fractional bandwidth.

In radio and millimeter astronomy it is popular to use the *brightness temperature* of an object, by which is meant the temperature corresponding to a given intensity (brightness) if inserted to the Rayleigh-Jeans relation:

$$T_b = \frac{c^2}{2k_B\nu^2} B_\nu. \tag{2.13}$$

Note that this definition is not only valid for blackbodies; it gives a temperature corresponding to a brightness at a given frequency. Furthermore, it can be used freely also where the Rayleigh-

Jeans approximation of the blackbody spectrum is not valid; in such cases the brightness temperature does not correspond to a physical property of the observed object.

In the case of the Sunyaev-Zel'dovich effect, the Rayleigh-Jeans approximation is not valid, since the temperature of the CMB is very low. For this reason, it is not practical to use the brightness temperature when comparing SZ observations at different frequencies. Keeping the simple and straightforward notation of the Rayleigh-Jeans formula, the expression for the change in thermodynamic temperature from the SZ effect can be written

$$\Delta T_{\mathrm{thermal}} = \mathcal{F}(x)\frac{c^2}{2k_B\nu^2}\Delta B_\nu, \tag{2.14}$$

where the correction factor $\mathcal{F}(x)$ is derived in Appendix A.

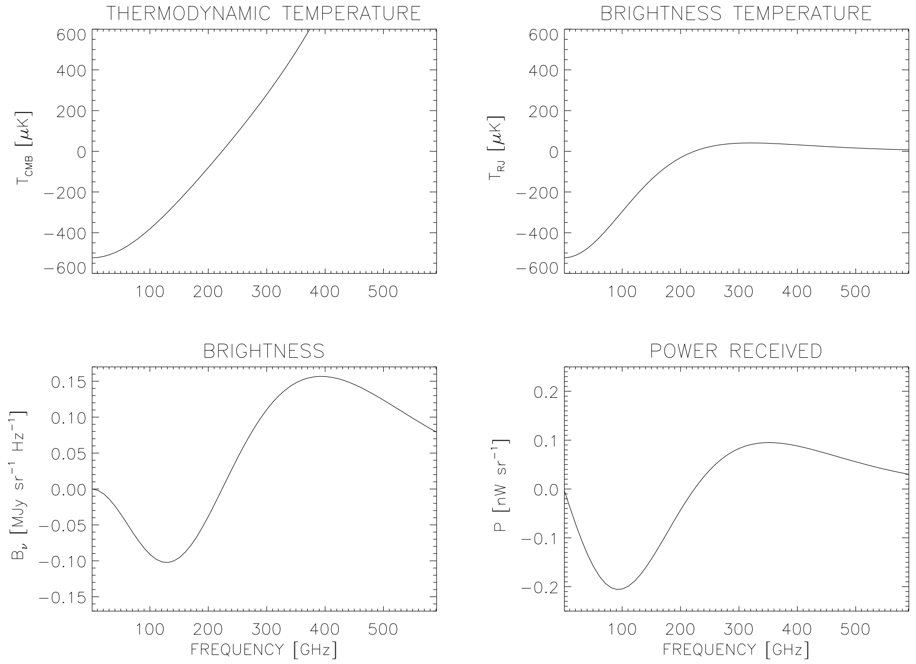

Figure 2.2: SZ effect distortion of the CMB blackbody towards the center of a fiducial cluster with $y = 10^{-4}$, $k_BT_e = 12$ keV and zero peculiar velocity. The top plots indicate the thermodynamic and Rayleigh-Jeans brightness temperature changes with respect to the CMB as a function of frequency. The bottom left shows the change in brightness (intensity), and the bottom right show the corresponding power received at a telescope (outside the Earth's atmosphere) computed using Eqn. (2.12) and assuming a fractional bandwidth $\Delta\nu/\nu = 0.25$.

2.2.3 The Relativistic Thermal Equation

Because of the low optical depth to Compton scattering typical for galaxy clusters, $\tau_e \sim 10^{-2}$, most photons are not scattered even once, rendering a diffusion approximation inadequate. The equations in § 2.2.1 are also manifestly non-relativistic, thus inaccurate at high electron temperatures (more than a few keV). Non-thermal relativistic corrections were first calculated by Wright (1979) and Fabbri (1981). To first order, one can rewrite the spectral shape factor $g(x)$ as

$$g(x, T_e) = \left(x \frac{e^x + 1}{e^x - 1} - 4 \right) (1 + \delta(x, T_e)) \,, \tag{2.15}$$

where $\delta(x, T_e)$ is the relativistic correction to the diffusion approximation.

Rephaeli (1995) calculated the full re-distribution of photons by considering the probability of electron-photon scatterings for a Maxwellian distribution of electrons. The resulting equation is computationally inefficient because it contains triple integrals. Furthermore, higher order effects from clusters moving with respect to the rest frame of the CMB are not taken into account. Itoh et al. (1998) made a diffusion approximation of the Boltzmann equation and arrived at a result consistent within 1% with that of Rephaeli up to electron temperatures of about 20 keV, which is well above the temperature of the hottest known cluster (Tucker et al. 1998).

Peculiar motions of the ICM were incorporated into the relativistic treatment by Nozawa et al. (1998) and by Sazonov & Sunyaev (1998). The results from the latter paper will be used in this thesis for computing SZ spectra, because it does not only consider relativistic effects to second order, but also includes so-called "interference terms", coupling the relativistic effect to the kinematic one.

Two points should be noted about the non-thermal effect. Firstly, it breaks the degeneracy of optical depth (or equivalently the Comptonization parameter y) and the electron temperature T_e, implying that ICM temperatures can be measured from SZ observations alone. Although the current observational leverage on such constraints is poor (chapter 8), SZ observations used in conjunction with X-ray observations can break the degeneracy more effectively, as discussed in § 2.3.1.

Secondly, the so-called crossover frequency, x_0, at which the SZ effect vanishes, is independent of electron temperature in the diffusion approximation, but increases slightly with T_e in the relativistic case. Although the kinematic effect is slight, the peculiar velocity has a stronger influence on x_0, owing to the fact that the peak of ΔB_ν^k (the latter having the same shape as the CMB blackbody) occurs at approximately the crossover frequency of the purely thermal effect, about $x = 3.83$ or $\nu = 217$ GHz.

Figure 2.3 shows the shape of the intensity shift due to the SZ effect for a cluster with $v_r = 0$ at different electron temperatures. The difference between the diffusion approximation and the relativistic treatment is obvious already at a temperature of 6 keV.

2.2.4 Isothermal Gas in Hydrostatic Equilibrium

The isothermal β model, first proposed by Cavaliere & Fusco-Femiano (1976, 1978) is widely used to model the gas profile in clusters. The profile derives from the King profile (King 1962), describing the distribution of stars in a globular cluster of stars. The different energy distributions of the gas and galaxies are both parameterized using the power-law index β (although β does not have to be equal for both components). The radial distribution of the electron density (and thereby the gas density) is given by

$$n_e(r) = n_e(r = 0) \left(1 + \frac{r^2}{r_c^2} \right)^{-\frac{3}{2}\beta} \tag{2.16}$$

where n_e is the density of electrons, r is the radius from the center and r_c is the core radius of the gas.

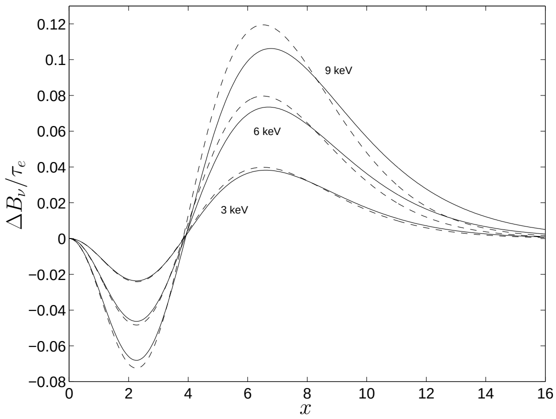

Figure 2.3: Spectral shape of the intensity change ΔB_ν due to the SZ effect, with $v_r = 0$. Solid lines show $\Delta B_\nu/\tau_e$ in units of $(hc)^2/(2(k_B T_0)^3)$, computed using the formalism of Sazonov & Sunyaev (1998) at $k_B T_e = 3$, 6 and 9 keV. Dashed lines show corresponding intensity changes computed from the non-relativistic diffusion approximation (Eqn. 2.7).

With this model, the X-ray surface brightness is

$$\begin{aligned} S_{\rm X}(\theta) &= \frac{1}{4\pi(1+z)^4} D_A \int n_e^2 \, \frac{\mu_e}{\mu_H} \, \Lambda_H(T_e) \, {\rm d}l \\ &= S_{\rm X}(0) \left(1 + \frac{\theta^2}{\theta_c^2}\right)^{-3\beta+\frac{1}{2}} \end{aligned} \tag{2.17}$$

where z is the redshift of the cluster, Λ_H is the X-ray cooling function of the ICM, and $S_{\rm X}(0)$ is the X-ray surface brightness at the center of the cluster. Furthermore, $n_H = n_e\mu_e/\mu_H$, where μ_e is the mean molecular weight of the electrons.

Similarly, the SZ signal from the spherical isothermal β-model is

$$\begin{aligned} \Delta T(\theta) &= g(x, T_e) \; T_{\rm CMB} \; D_A \int n_e \sigma_{\rm T} \; \frac{k_{\rm B} T_e}{m_e c^2} \; {\rm d}l \\ &= \Delta T(0) \left(1 + \frac{\theta^2}{\theta_c^2}\right)^{-\frac{3}{2}\beta+\frac{1}{2}} \end{aligned} \tag{2.18}$$

where ΔT is the *thermodynamic* SZ temperature decrement (or increment), $g(x, T_e)$ is given by Eqn. 2.15 and D_A is the angular diameter distance.

In the more realistic case that the ICM is not isothermal, β models fitted to X-ray measurements tend to underestimate the central surface brightness and overestimate it at large radii (Jones & Forman 1984, Vikhlinin et al. 1999), while SZ measurements tend to overestimate the value of β (Hallman et al. 2007). Given the sensitivity of current instruments, the β model provides an approximation of the intra-cluster gas radial density distribution with which X-ray and SZ observations can still be brought into reasonable agreement (see chapter 7).

2.2.5 Observations of the SZ Effect

Theoretical studies suggest that both the central and integrated SZ signals from a cluster are excellent probes of the cluster mass (Motl et al. 2005). Battye & Weller (2003) and Tang & Fan (2003) normalize the optical depth in terms of the virial mass using

$$\frac{M_{\mathrm{vir}} f_{\mathrm{gas}}}{\mu_e m_p} = D_A^2 \int n_e \mathrm{d}l \mathrm{d}A, \tag{2.19}$$

where f_{gas} is the ICM gas fraction (~ 0.1) and $1/\mu_e = (1+X)/2$ where X is the hydrogen mass fraction (~ 0.75). In terms of the integrated Comptonization Y, this means that for an *unresolved cluster*,

$$Y = \sigma_T D_A^{-2} \frac{M_{\mathrm{vir}} f_{\mathrm{gas}}}{\mu_e m_p} \frac{k_B \langle T_e \rangle_n}{m_e c^2} \equiv Y_0, \tag{2.20}$$

where the *electron density weighted average temperature* is defined by

$$\langle T_e \rangle_n = \frac{\int n_e T_e \mathrm{d}l}{\int n_e \mathrm{d}l}. \tag{2.21}$$

It is expected (e.g. Eke et al. 1996) that the cluster mass scales with temperature as $T_e \propto M^{2/3}$, although the normalization of this relation has yet to be constrained.

Existing techniques for observing the SZ effect can be roughly divided into three categories: detection experiments with heterodyne receivers on single-dish telescopes, detection or mapping experiments with arrays of bolometers, and interferometric imaging (synthesis imaging) experiments.

Though not as sensitive as bolometers, modern heterodyne receivers have sensitivities that far exceed what is necessary to detect the SZ effect from the most massive clusters of galaxies. What makes SZ experiments difficult are the control of systematics, such as poorly understood variations in atmospheric emission and instrumental gain instabilities. For this reason, all SZ observations are differential in one way or another. Another severe problem is the systematics introduced by astrophysical contaminants, such as the primary CMB anisotropies and radio point sources, which will be discussed in chapter 3.

Successful early SZ detections were made with single dish telescopes at cm wavelengths using beam switching techniques to control the systematics introduced by atmospheric emission and ground pickup. Birkinshaw et al. (1978) made an early detection with the OVRO 40m telescope, and the techniques were subsequently refined on the OVRO 5m telescope at 30 GHz by Herbig et al. (1995), Myers et al. (1997) and Mason et al. (2001). Significant detections were also made at the SEST 15m and IRAM 30m telescopes, both employing photometers at 140 GHz (Andreani et al. 1996, Desert et al. 1998).

Interferometric observations of the SZ effect have been successfully carried out with the OVRO/BIMA interferometers (e.g. Reese et al. 2002) and CBI (Rajguru et al. 2005). A major advantage, other than the inherent stability due to simultaneous differential sky measurements, is that different ranges of baselines can be used to recover emission on different spatial scales. This can and has been used to remove radio point source emission from SZ data.

Modern bolometer cameras (or bolometer arrays) which have been used to detect or map the SZ effect include SCUBA (Gear & Cunningham 1995), SuZIE (Holzapfel et al. 1997a,b), BOLOCAM (Glenn et al. 1998) and the key project of the South pole telescope (Carlstrom 2006), through which several previously unknown clusters have recently been discovered through the SZ effect (Staniszewski et al. 2008). In this thesis, mainly data from the

APEX-SZ array at 150 GHz is presented. The resolution of this instrument is one arcminute full-width half-maximum (FWHM), matching the expected core diameter of massive clusters at high redshift (Schwan et al. 2003).

At present, most SZ detections are in the decrement part of the spectrum, i.e. below 220 GHz. Detections in the increment are difficult because of the higher atmospheric opacity, but also because the SZ signal can be partially confused by dust emission from unresolved sub-mm galaxies (e.g. Kitayama et al. 2004). Operating on the APEX telescope at a site with relatively low atmospheric opacity at 345 GHz, the LABOCA bolometer array (Siringo et al. 2007) is barely sensitive enough to overcome the first of these problems. Due to the high resolution ($19''$ FWHM) at this frequency, it is also possible to single out bright isolated sources of dust emission. A first detection of the SZ effect with the LABOCA array is presented in chapter 9.

2.3 Applications of the Sunyaev-Zel'dovich Effect

Physical applications of the SZ effect can be roughly divided into two groups: those concerned with cluster gas distributions and properties, and those using the effect as a cosmological probe. Both sets of applications are briefly introduced in what follows.

2.3.1 Measurements of Cluster Structure

Due to the degeneracies of temperature, velocity and optical depth in the SZ effect, combined with the available instrument sensitivities, little new information on cluster structure can be extracted from SZ observations alone, particularly if data at only one observing frequency is available. However, in combination with optical and X-ray data, there are several interesting possibilities, the most important of which are outlined here.

While the X-ray emission from thermal Bremsstrahlung is proportional to the line-of-sight integrated square of the free electron density, the SZ effect measures the integrated electron pressure along the line of sight, and hence depends linearly on density. Combining spatially resolved X-ray and SZ maps of a galaxy cluster thus in principle allows the modeling of the three-dimensional distribution of the gas properties (density and temperature). In the simple case of a spherical gas distribution, one can directly derive the gas density profile of a cluster by dividing the product of the X-ray derived temperature and line-of-sight integral of the gas density by the SZ derived Comptonization. This is the subject of chapter 9.

Because the SZ signal scales with electron density and X-ray emission with the square of that density, it should be possible to measure the so-called clumping factor $C_n = \langle n_e^2 \rangle / \langle n_e \rangle^2$ (e.g. Birkinshaw 1999) along the line of sight through a cluster. Such measurements, however, depend on the assumption that clumping occurs at constant temperature. No systematic study of the gas clumping inside clusters has been made to date, although constraints have been derived from hydrodynamical simulations of clusters (da Silva et al. 2000, 2001, Springel et al. 2001).

For an isothermal gas distribution, the SZ intensity is directly proportional to the projected gas density. Thus, comparing it to total mass as determined from gravitational lensing provides a direct estimate of the baryonic mass fraction. This estimate is free from any uncertainties due to gas clumping, which is the dominant uncertainty ($\sim 20\%$) in similar analyses with X-ray measurements.

2.3.2 Cosmological Applications

Birkinshaw (1999) points out that the simplest use of the SZ effect is to show that the CMB is indeed a cosmological phenomenon; the mere fact that the effect is observed from a cluster of galaxies at a certain redshift proves that the CMB originates at a still higher redshift. Aside from this elementary application, the SZ effect has been suggested and used as a means of measuring cosmological parameters.

The Hubble parameter H_0 can be determined jointly from X-ray and SZ measurements, again by taking advantage of the different electron density dependences. While the surface brightness of the emitting gas (X-ray) is dependent on a line-of-sight integral of the electron density squared, the SZ effect is proportional to the Compton optical depth, which is a line-of-sight integral with a linear dependence on the electron density. Measuring both quantities thus yields a density weighted measure of the path length through the gas. Comparing this path length to the angular size of a cluster, the cosmological angular diameter distance to the cluster can be estimated. This, in turn, combined with the redshift of the cluster gives a measure of the Hubble parameter. Reese et al. (2002) constrained the Hubble constant to $H_0 = 60^{+4+13}_{-4-18}$ km s^{-1} Mpc^{-1} for a standard ΛCDM cosmology in this way, using isothermal assumptions for the ICM.

It has been suggested that the SZ effect can be used to test the standard scaling of CMB temperature with redshift by measuring the temperature of the CMB at the redshifts of clusters of galaxies (Battistelli et al. 2002, Horellou et al. 2005). An alternative scaling would have profound implications on cosmology, implying the creation of energy in a manner that would still maintain the black-body shape of the CMB spectrum at redshift zero.

The cluster gas mass fraction derived from joint X-ray and SZ measurements can also be used as a tool to constrain cosmological parameters. In particular, the redshift evolution of the gas mass fraction depends strongly on the matter and dark energy components of the universe (e.g. Allen et al. 2004). LaRoque et al. (2006) have shown that SZ measurements significantly reduce the scatter in gas mass fraction estimates compared to X-ray derived values.

From large scale SZ surveys, it is expected that the abundances of dark energy and dark matter can be constrained, along with the normalization of the matter power spectrum. The basic idea is to count all clusters above a certain mass limit as a function of redshift, and to compare these counts with models of large scale structure formation (Press & Schechter 1974, Sheth & Tormen 1999, Jenkins et al. 2001) given a set of cosmological parameters. Predictions for a wide range of future experiments are laid out by Battye & Weller (2003).

A potential problem in number counts of clusters is that of projection: because the SZ surface brightness is insensitive to redshift, it is also sensitive to projection effects from the line of sight throughout the observable universe. On any line of sight, the probability of passing within the virial radius of a cluster of galaxies is of order unity (Voit et al. 2001, White et al. 2002), which means there will be a high probability of overlap in a deep SZ surveys. Powerful constraints from deep SZ surveys will thus have to be derived from the power spectrum of the SZ effect rather than from simple number counts.

Chapter 3

Noise and Confusion Issues in Single-Frequency SZ Surveys

3.1 Introduction

Any astronomical survey requires reliable constraints not only on the noise powers of the instrument and the atmosphere, but also on other astrophysical sources that may offset the results. In the context of SZ observations, this is particularly true for a single-frequency survey like the one currently being carried out with the APEX-SZ instrument (see chapters 5 and 7). In a multi-frequency survey like *Planck* (e.g. Geisbüsch et al. 2005), the survey data itself can, to some extent, be used to disentangle the different sky components, while in the case of a single frequency survey one instead has to rely on prior knowledge of the astrophysical sources, in particular their distributions and intensities, to model the background and foreground.

This chapter discusses what different astrophysical components need to be taken into consideration at the frequency of the APEX-SZ instrument (150 GHz). It is discussed how they can be modeled, and how well such models are constrained at present. Astrophysical contaminants include unresolved flat-spectrum radio sources, dust emission and primary CMB anisotropies. A simulation is carried out including all noise and confusion components, except for atmospheric noise (see chapter 6), combined with the projected SZ emission of a set of real galaxy clusters, to predict survey yields at 150 GHz with APEX-SZ and quantify the statistical contributions of the different contaminants.

3.2 Astrophysical Contaminants

3.2.1 Primary CMB

The power spectrum of the primary CMB from the surface of last scattering has been well constrained out to the third acoustic peak by the *WMAP* satellite (Bennett et al. 2003, Komatsu et al. 2008) and out to the fifth peak by ground based experiments (Kuo et al. 2007, Jones et al. 2006). Because the power spectrum of the CMB is damped on small angular scales (e.g. Hu & White 1997), it is not expected to pose a problem for SZ observations of clusters within angular extents of a few arcminutes. In spite of this, the primary CMB is considered in the simulations part of this chapter to test the reliability of cluster extraction.

3.2.2 Radio Point Sources

An important contaminant to the SZ signal are radio sources within clusters, such as star-forming galaxies, AGN and central cD galaxies (Toffolatti et al. 1999, Massardi & De Zotti 2004), which can offset the SZ decrement, causing underestimates of the SZ decrement flux. The over-density of radio sources in cluster environments is well known (see chapter 4), and for an unresolved cluster, it can even be expected that a point source such as a central cD galaxy with similar flux might completely obscure the decrement SZ signal.

Although some sources associated with clusters have been observed up to 30 GHz (Cooray et al. 1998), there is very little information on spectral properties of radio sources at mm-wavelengths. At low frequencies, this is indeed a limiting factor in constraining astrophysical confusion of SZ signals. Most radio sources have steep spectra ($\alpha > 0.5$, $S_\nu \propto \nu^{-\alpha}$) in the 1−10 GHz regime, and those with lower spectral indices are expected to turn over with steepening spectral slopes above some break frequency, ν_b, where the emitting region is optically thin. Thus, radio point sources pose much less of a problem at higher frequencies.

3.2.3 The Submillimeter Background

While SZ observations at high frequencies are less sensitive to radio source contamination, there can be a significant contribution from unresolved infrared sources. There is, however, no evidence of any overdensity of such sources of such thermal emission in galaxy clusters. Source counts from the SCUBA bolometer array are consistent with an angular density of more than one source per arcminute with a flux density greater than 1 mJy (Smail et al. 1997, Borys et al. 1999). Borys et al. (2003) quantify the source counts at 350 GHz with a phenomenological fit as

$$\frac{dN}{dS_\nu} = \frac{N_0}{S_0}\left(\left(\frac{S_\nu}{S_0}\right) + \left(\frac{S_\nu}{S_0}\right)^{3.3}\right)^{-1}, \tag{3.1}$$

where $N_0 = 1.5 \times 10^4$ deg^{-2} and $S_0 = 1.8$ mJy.

White & Majumdar (2004) extrapolate the IR source counts from Smail et al. and Borys et al. using $S_\nu \propto \nu^\beta$ with $\beta = 2.5$. This gives a source density of 10−100 sources above 1 mJy per square degree at 150 GHz. Thus, IR sources should also be reckoned with for a survey instrument such as APEX-SZ, where deep integrations down to comparable levels are in progress.

Background sub-mm sources can be gravitationally lensed by massive galaxy clusters, often rasing them above the detection limit. This can cause considerable bias in the SZ signal (e.g. Loeb & Refregier 1997), but this effect is not considered here. It is discussed in the context of cluster observations in chapters 7 and 9.

3.3 A Simulated SZ Survey at 150 GHz

A straightforward way of quantifying how astrophysical contamination effects cluster counts is to use a simulation. Rather than simulating every sky component, which would require many secondary assumptions such as in modeling the spatial distribution of clusters of galaxies, an actual piece of sky with as much information as possible is selected here, namely a ∼10 square degree field covered by the Red-Sequence Cluster survey (RCS, Gladders & Yee 2005). The limiting factor is the poor understanding of the spectral slopes of the radio and IR point sources. The RCS survey is also limited by being sensitive to a narrower range of redshift than what will be expected for an SZ survey like the one conducted with APEX-SZ.

3.3.1 Sample

The survey patches RCS 0926+37 and RCS 1329+27 comprise a total of 429 candidate galaxy clusters and groups down to a significance of 3.29 σ with photometric redshift estimates (R_C and z' filters). 241 of these objects are found in RCS 0926+37. The distribution of redshifts for both fields is given in Figure 3.1. Also plotted are the expected differential clusters counts for APEX-SZ at 150 GHz for a five sigma detection threshold, assuming an expected rms noise of 10 μK per 1 arcminute beam (corresponding to a flux of 2 mJy). The counts have been computed as in Horellou et al. (2005) and assuming all clusters are unresolved; thus the actual cluster counts are expected to be somewhat lower, in particular at low redshifts. Note that the selection function of clusters in any optical survey is likely to be vastly different from that expected in a beam-matched SZ survey; however, since present estimates of SZ survey yields vary by as much as 50% from one another, any simulated catalog of clusters is likely to be somewhat sketchy. Here, a very simple approach is taken that allows some input from actual data.

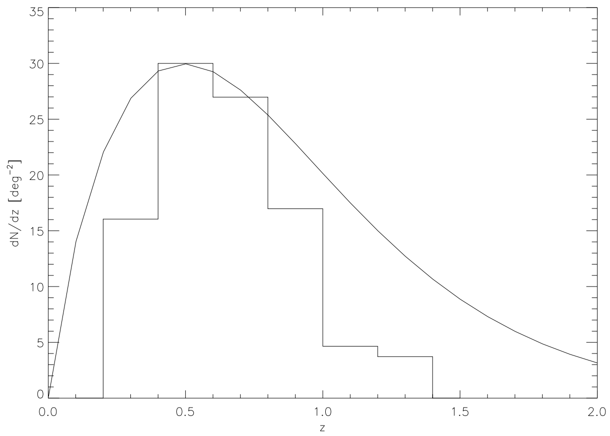

Figure 3.1: Redshift distribution of candidate galaxy clusters in the patches RCS 0926+37 and RCS 1327+29 (arbitrarily normalized histogram), compared to the projected differential cluster counts for the APEX-SZ survey at 150 GHz.

Both RCS patches are covered by the NVSS (Condon et al. 1998) and FIRST (Becker et al. 1995) surveys at 1.4 GHz; the latter will be used considering its superior angular resolution. The FIRST survey is complete down to 1 mJy with a resolution of 5 arcseconds. Both RCS fields were searched for cluster point sources; however, only RCS 0926+37 is used for the full analysis.

3.3.2 Cluster Model

To compute signals from the clusters, a number of assumptions are made. First, all clusters are assumed to be virialized, and model cluster masses and radii are computed from the richness parameter B_{gcR} according to Yee and Ellingston (2003) as

$$\log M_{200} = (1.64 \pm 0.28) \log B_{\mathrm{gcR}} + (10.05 \pm 0.89)\ h^{-1} M_{\odot} \tag{3.2}$$

and

$$\log r_{200} = (0.47 \pm 0.16) \log B_{\mathrm{gcR}} - (1.05 \pm 0.48)\ h^{-1}\mathrm{Mpc}, \tag{3.3}$$

where B_{gcR} is in units of $\mathrm{Mpc}^{1.8}$, and $h = 0.7$ is assumed throughout. The radius inside which the mean mass over-density with respect to the universe as a whole is equal to 200, r_{200}, is rescaled to virial mass using the prescription given by Hu & Kravtsov (2003).

A spherical, isothermal cluster model is assumed. The Compton y-parameter along a line of sight can then be computed as (e.g. Komatsu & Kitayama 1999)

$$y(\theta) = \sigma_T n_{e0} r_c \left(\frac{k_B T_e}{m_e c^2}\right) \frac{\pi e^{1/\xi p^2}}{\sqrt{1 + (\theta/\theta_c)^2}} \operatorname{erfc}\left(\frac{1 + (\theta/\theta_c)^2}{\xi p^2}\right), \tag{3.4}$$

where n_{e0} is the central electron number density, $p = r_{vir}/r_c$ with r_c the core radius, and T_e is the electron temperature in the isothermal model. The virial radius is computed as (e.g. Peebles 1980)

$$r_{\mathrm{vir}} = \left(\frac{M_{\mathrm{vir}}}{(4\pi/3)\rho_{\mathrm{crit}}(z)\Delta_c(z)}\right)^{1/3}, \tag{3.5}$$

and the core radius is

$$(1+z)^{(1/5)} r_c(z=0), \tag{3.6}$$

where $r_c(z=0) = b_0\, r_{\mathrm{vir}}(z=0)$ with $b_0 = 0.14$ (e.g. Geisbüsch et al. 2005).

The central electron number density is

$$n_{e0} = \frac{f_{gas} M_{\mathrm{vir}}}{4\pi r_c^3 p} \frac{X+1}{2m_p}, \tag{3.7}$$

where $f_{gas} = 0.1$ is the ICM gas mass fraction and $X = 0.76$ is the hydrogen abundance. The electron temperature is given by

$$k_B T_e = \eta \mu m_p \frac{G M_{\mathrm{vir}}}{3 r_{\mathrm{vir}}} \tag{3.8}$$

in hydrostatic equilibrium.

Applying this model to all clusters out to the virial radius, a Compton y-map of the entire field is generated. The SZ decrement to the CMB temperature is then

$$\Delta T/T = g(x) y(\theta), \tag{3.9}$$

where $g(x)$ is the spectral shape of the SZ effect (chapter 2). Note that this temperature is a line of sight quantity and that no instrument beam has been applied.

3.3.3 Point Source Distribution

Powerful radio point sources are strongly coupled with centers of galaxy clusters (see chapter 4 for more detail). To quantify the correlation, the over-densities at different radii from cluster centers are computed, the result of which is shown in Figure 3.2. The data points fit a very narrow projected β-profile (Cavaliere & Fusco-Femiano 1976)

$$n = n_0 \left(1 + \frac{r^2}{r_0^2}\right)^{(-3/2)\beta + 1/2}, \tag{3.10}$$

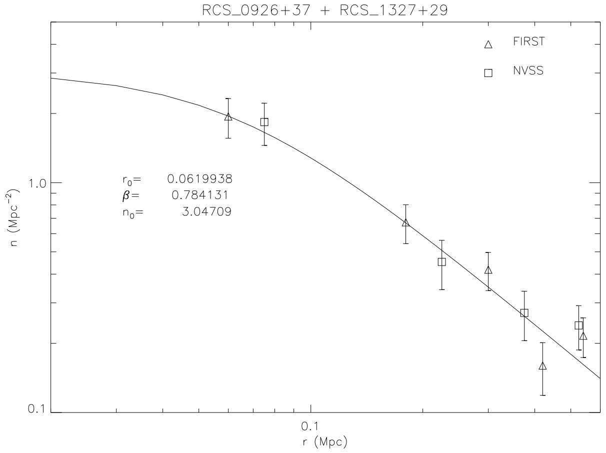

Figure 3.2: Abundance of radio point sources near galaxy clusters in the RCS fields, as a function of distance from the cluster center. Data points show the number density of sources in annuli centered at radii r, from the NVSS and FIRST catalogs at 1.4 GHz. The solid line shows a least-squares fit with an isothermal β-model.

with $\beta = 0.78$ and $r_0 = 0.06$ Mpc. A physically meaningful β-profile, describing the distribution of gas or that of all galaxies (e.g. Reddy & Yun 2004), cannot be this narrow. Lacking a proper physical model, however, it is adopted here as a convenient description of the clearly different distribution of radio sources. The distribution is discussed in detail in chapter 4.

Though the profile is not applied to the subsequent analysis, it can be used together with a cluster source luminosity function (chapter 4) to place point sources inside simulated clusters at higher redshifts. This can in principle be implemented to account for the different sensitivity of an SZ survey across the range of observable redshifts, but such analysis would require detailed information on spectral slopes in order to extrapolate the luminosity function.

3.3.4 Brightness Temperature Maps

Radio Point Sources

After producing maps of SZ decrement brightness temperatures at 150 GHz with an appropriate pixel size of 15 arcseconds (the beam of APEX-SZ is one arcminute), the 1.4 GHz point source fluxes from FIRST are extrapolated to the same frequency using the simple model of Holdaway & Owen (2005). Two thirds of the sources are assumed to have steep spectra and are assigned random spectral slopes according to the distribution of Holdaway & Owen. The remaining one third are assumed to have flat spectra, and could possibly contaminate an SZ survey. For simplicity, these sources are assumed to have the same flux at 150 GHz as at 1.4 GHz. In reality, the contamination should be less severe as there is expected to be a break frequency above which the spectra turn steep.

Instrument Noise

The APEX-SZ bolometer array was originally expected to image hundreds of square degrees with an instrument noise level of around 10 μK per beam (Schwan et al. 2003). This brightness temperature rms level, corresponding to about 17 μK in thermodynamic (CMB) temperature, has indeed been reached on a small field around the cluster XMM-XLSSC006 as discussed in chapter 7. Although the area covered in that field is less than a square degree, the same noise level is used here in anticipation of an upgrade of the instrument which will make possible a survey meeting the original goal.

Primary CMB

From a ΛCDM cosmology with the most recent cosmological parameters from WMAP (Komatsu et al. 2008), a CMB power spectrum is produced using the microwave anisotropy code *CMBFAST*[1] (Zaldarriaga & Seljak 2000). The resulting power spectrum is used to simulate a full-sky anisotropy map using the *HEALPix*[2] software (Gorski et al. 2005). From this anisotropy map, a field matching that of the simulation is extracted and added to the artificial SZ map. Because *HEALPix* can only generate full-sky maps, the procedure is computationally difficult with small pixel dimensions. For this reason, the pixel size is chosen as $1.7'$, and it is assumed that primary anisotropies on smaller scales are negligible.

Sub-millimeter sources

Lacking deep sub-mm data on this field, a distribution of sources is simulated at 350 GHz according to the differential source counts of Borys et al. (2003). Each source is thus assigned a flux at 150 GHz by scaling with some spectral index β such that $S_\nu \propto \nu^\beta$.

Rather than using a constant spectral index, a normal distribution with mean 2.5 and sigma 0.3 is adopted. The sources are distributed randomly in the map. Smoothing the resulting map to the APEX-SZ beam scale yields the pixel distribution shown in Figure 3.3. The beam-

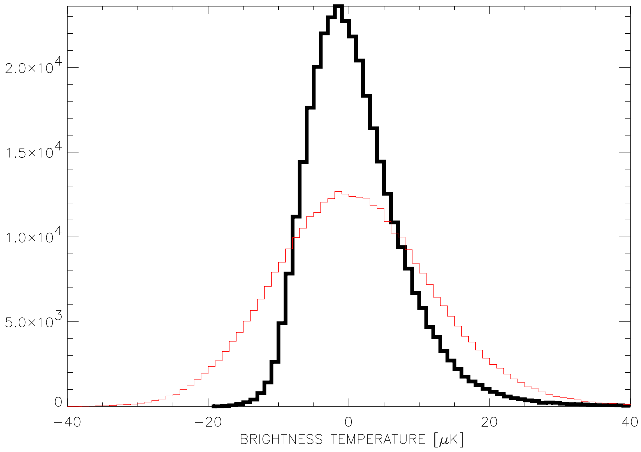

Figure 3.3: Pixel distribution of a beam-smoothed (APEX-SZ) simulated field of sub-millimeter sources (thick line) after the median has been removed. The histogram marked with the thin line shows the corresponding pixel distribution after an instrumental noise component of has been added (see text).

---

[1] `http://www.cmbfast.org/`

[2] `http://www.eso.org/science/healpix/content/Introduction.html`

convolved sub-millimeter source distribution is slightly skewed, but deviations from a Gaussian behavior are mainly seen in the bright end of the distribution. After removing bright sources, the distribution can be modeled quite accurately as a source of Gaussian noise. The standard deviation of this distribution is $7\,\mu$K (brightness temperature).

3.3.5 Cluster Extraction

For extracting clusters from the final (noisy and smoothed) simulated map, the *SExtractor*[3] software (Bertin & Arnouts 1996) is used. To select suitable parameters for running the software, a map with very little noise ($4\,\mu$K/pixel) and no point sources is used. The parameters are then adjusted (see the SExtrator manual for more details) to recover as many clusters as possible and make cluster-cluster confusion the limiting factor. The software detects positive sources only; for this reason a negative map is used in order to detect the SZ decrements and avoid detecting point sources.

The background CMB primary anisotropies, varying on angular scales typically much larger than the clusters, rule out the use of a constant background level. Instead a smoothly varying background is fit to the data with SExtractor, which is approximately equivalent to filtering out large angular scales by Fourier or wavelet transform beforehand.

Figure 3.4 shows a comparison of the massive clusters in the RCS cluster catalog and the clusters recovered by SExtractor at 5σ. Already at this stage, there are clear problems in recovering clusters, in particular in the vicinity of the very extended cluster to the north-east. Using a less efficient cleaning yields more cluster detections, but also many more spurious ones. In this case, 164 of the 241 clusters were recovered. Lowering the noise even more does not significantly change this result.

3.3.6 Results

Including point sources and random noise in the analysis as described above, 78 clusters in total are recovered. The resulting map of the field is shown in Figure 3.5, where the primary CMB component has been removed to emphasize the contrast of the galaxy clusters from the background. Four more clusters are extracted when point sources are removed. For comparison, the procedure is repeated assuming *all* point sources have flat spectra. This unrealistic scenario results in 8 clusters not being detected because of point source confusion; there is also one false detection at 5σ.

Figure 3.7 shows the distribution in redshift and the richness parameter B_{gcR} of the recovered clusters. Note that almost all clusters at redshifts above 1 are recovered; this is in part because these clusters have small angular sizes (1 Mpc corresponds to about 2 arcminutes at $z = 1$, and 4 arcminutes at $z = 0.3$), but also because at high redshifts the red-sequence algorithm (Gladders & Yee 2000) is only sensitive to very massive clusters. APEX-SZ is expected to detect a wider range of masses, as hinted at in Figure 3.1.

3.4 Conclusion

The simple analysis put forth here is limited by the very different selection function of the RCS survey compared to that of SZ surveys. This is clear already from figure 3.1. Nevertheless, recent results indicate that the yield of SZ surveys will be much lower than previously estimated

---

[3] `http://terapix.iap.fr/rubrique.php?id_rubrique=91/`

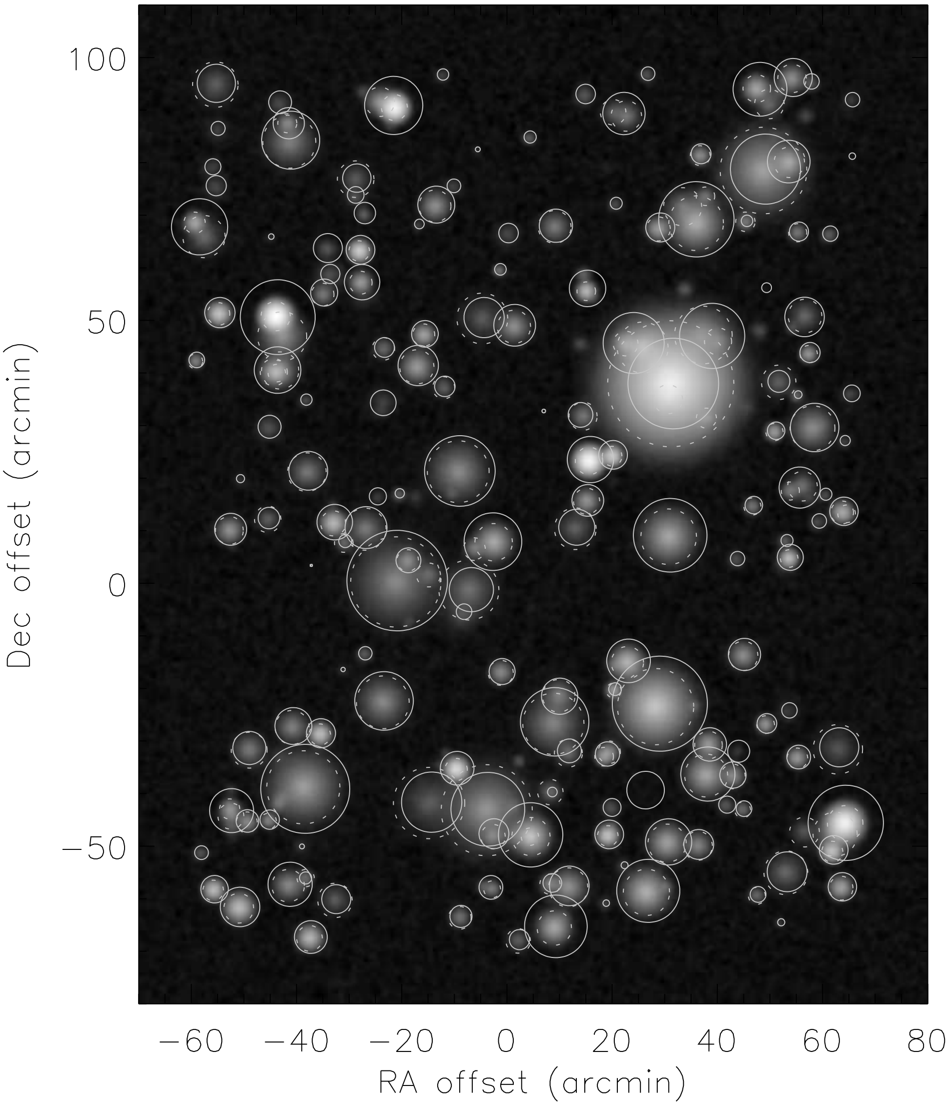

Figure 3.4: SZ model map in the field RCS 0926+37 with only 1/16 of the actual pixel noise in the simulated map added. Dotted circles indicate the virial radii of the "input" clusters from Gladders & Yee (2005) above a threshold of $B_{\rm gcR} = 200\,{\rm Mpc}^{1.8}$. Solid circles indicate clusters recovered by the SEXtractor software (arbitrary radii). The shading is proportional to Log(T). No contaminants have been added, thus cluster-cluster confusion is the limiting factor in recovering clusters.

(Staniszewski et al. 2008), which would lower the number of expected SZ cluster detections not expected to be detected in an optical survey such as the one considered here.

A few tentative conclusions can be drawn about the statistical contribution of the various contaminants to the number counts of clusters detected in the SZ decrement:

1. It is not strictly necessary to quantify the sub-millimeter background as a contaminant since the total contribution is very close to a Gaussian distribution and will show up in any observation as excess noise, unless one integrates down to the level of individual bright sources. It puts an absolute limit on what rms can be reached in any map, unless it is possible to subtract some of this distribution by cross-correlating with observations at other frequencies. However, the effective equivalent rms value of 7 μK derived in this chapter has several sources of uncertainty. White & Majumdar (2004) estimate an uncertainty of a factor 2 in the normalization of source counts at 350 GHz. Furthermore, the extrapolation from 350 to 150 GHz introduces a similar factor in the source counts at 150 GHz, resulting in an effective uncertainty of a factor 3 in the source counts at 150 GHz.

2. Gravitational lensing of background sub-mm sources has not been taken into account. As discussed in subsequent chapters, the effect is only important when a source is detected and removed, and in the nine APEX-SZ detections presented in chapter 7 there is not a single detection of a point source close to a cluster center. Thus with the current sensitivity of APEX-SZ, the effect of lensing is negligible, although it does become important when observing the SZ effect at higher frequencies (cf. § 9.4.3).

3. Assuming the noise levels discussed here, radio point sources can offset *total* number counts of clusters with no more than 10%. This sample is too small to quantify any redshift dependence in this source of contamination. Note that current multi-frequency surveys (Calstrom 2006, Huffenberger et al. 2005) will be able to overcome point source contamination problems much better than a single-frequency experiment like APEX-SZ. Note also that while point source contamination from *flat-spectrum* sources is likely to be overestimated here because break frequencies have not been considered below 150 GHz, the possibility of *inverted* sources, with spectra rising above 1.4 GHz, has not been considered.

4. The primary CMB signal does not affect the cluster extraction in this analysis. Although it is important to consider the CMB as a source of error in absolute decrement values, it poses no real challenge to number counts of clusters of galaxies in SZ surveys.

In this analysis, a Gaussian noise distribution has been assumed from the instrument. In reality, it is to be expected that a certain amount of residual $1/f$ noise, in part residual noise from the atmosphere, is present (see chapters 5−7). It should be noted that the quoted results and conclusions may have to be revised in the light of a more realistic noise distribution.

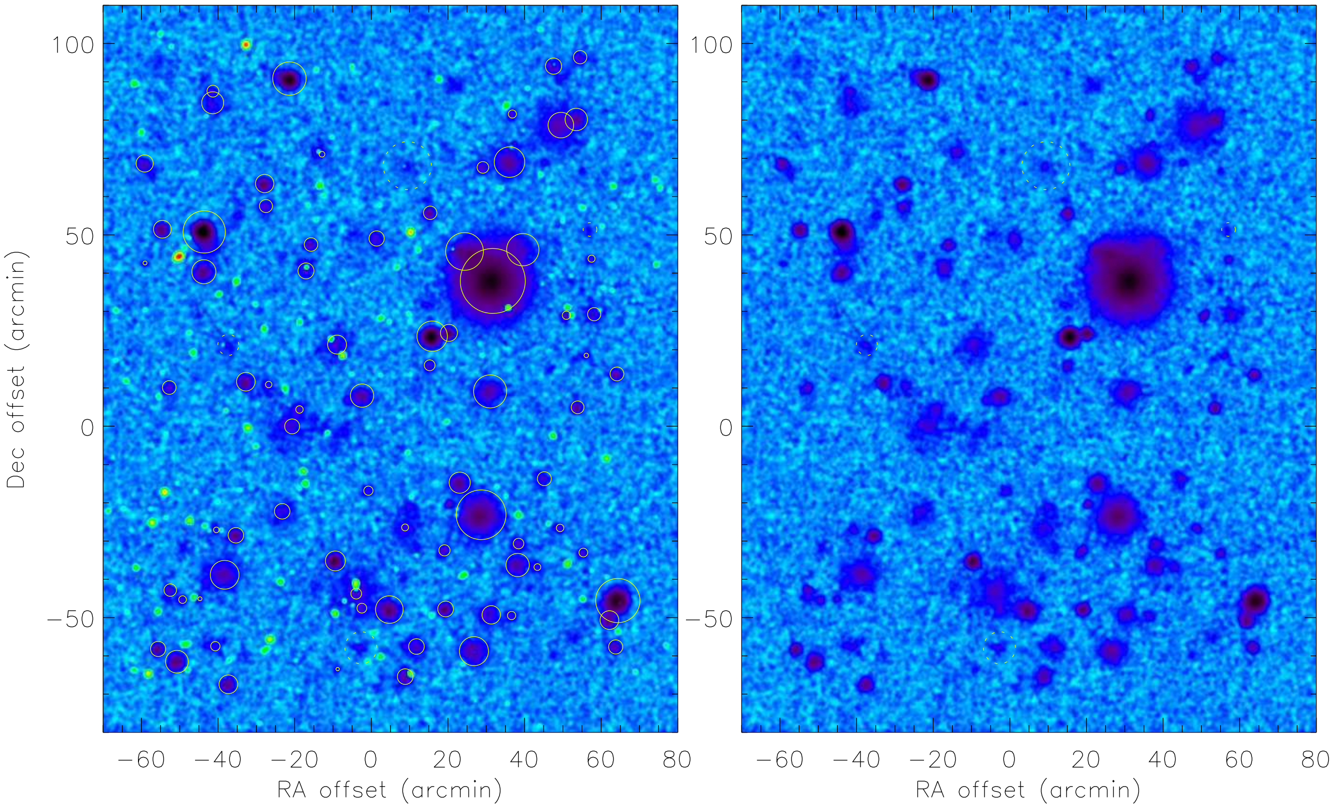

Figure 3.5: Beam-convolved maps of clusters, point sources and noise. The primary CMB component has been removed to make the image clearer. For comparison, the radio point sources have been removed from the image on the right. A total of 78 clusters are detected (left). Dotted circles indicate four clusters that are detected only when the point sources are removed. The shading is proportional to Log(T'), where T' is the brightness temperature scaled to all positive values. The color scale is arbitrary with clusters (negative signals) shown as black to purple, and point sources (positive signals) shown as yellow to green.

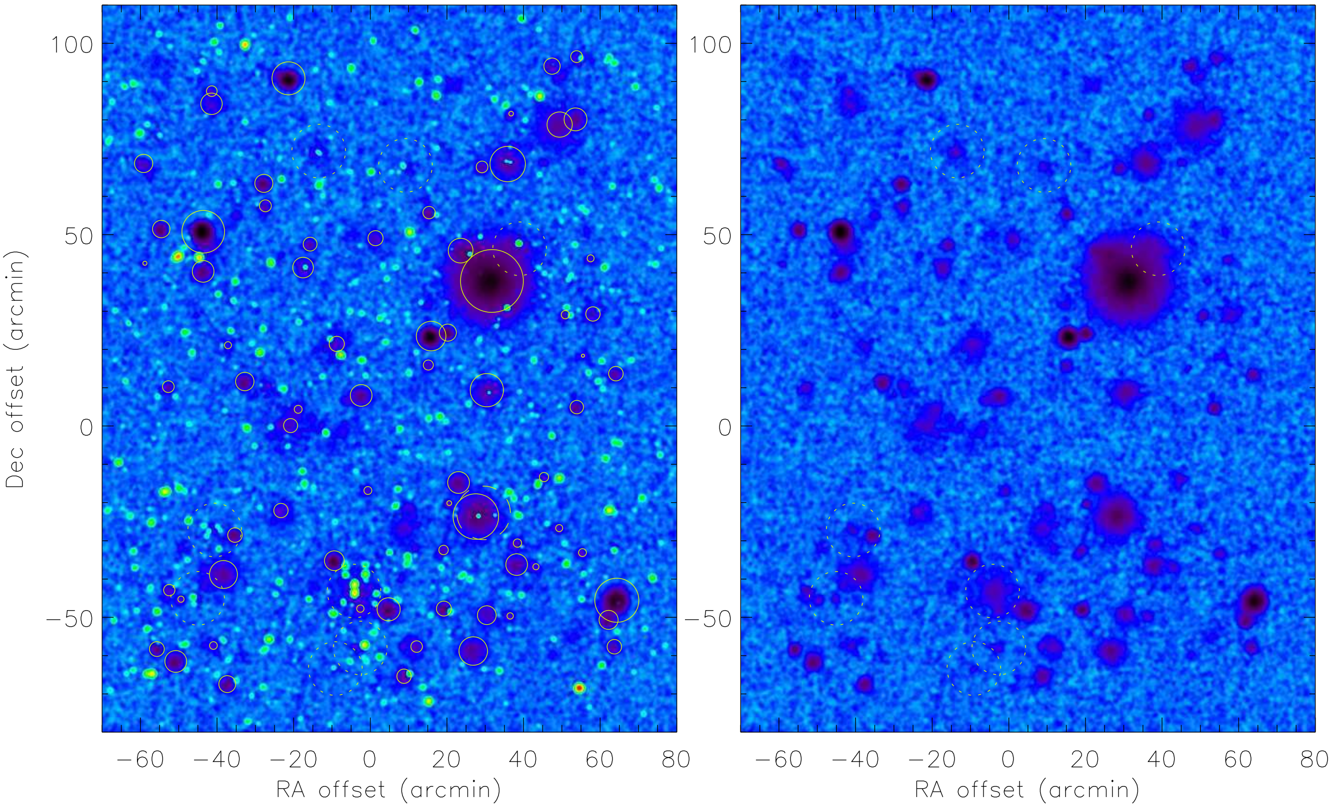

Figure 3.6: Same as Figure 3.5, but (unrealistically) assuming that all radio point sources have flat spectra from 1.4 to 150 GHz. The dashed circle in the left map indicates a spurious detection.

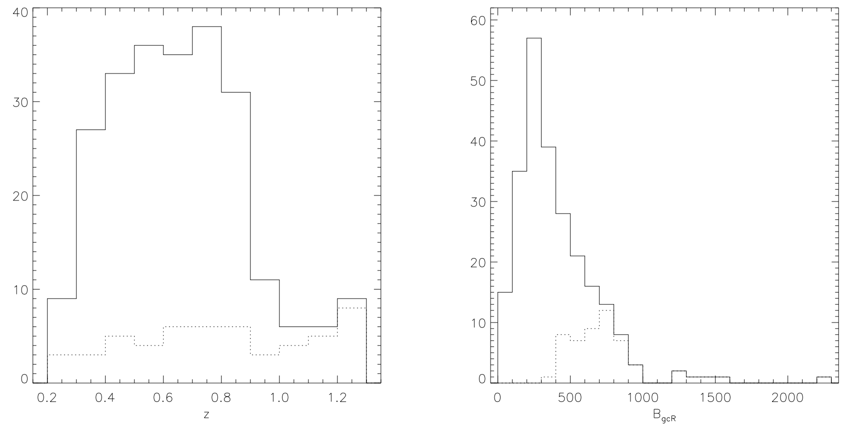

Figure 3.7: Redshift and richness distribution of recovered clusters (dotted lines) compared to the original cluster distribution (solid lines).

Chapter 4

The 1.4 GHz Luminosity Function in Galaxy Clusters

4.1 Introduction

In this chapter, the space and luminosity distributions of radio galaxies residing in clusters of galaxies are investigated. Significant statistical conclusions are made possible by using publicly available optical and X-ray selected cluster catalogs, and the uncertainties are dominated by systematics introduced by the different selection effects present in the construction of such catalogs.

Powerful radio sources are generally associated with early type galaxies that preferentially reside in cluster centers. Apart from the problem of contamination in SZ observations, the study of the radio loud population of active galactic nuclei (AGN) inside galaxy clusters is very interesting in itself, because it can potentially shed light on the interaction between cluster cooling flows and AGN heating/feedback scenarios. Analyzing the radio properties of galaxy clusters can provide direct evidence of heating of the intra-cluster medium by AGN through various stages of cluster formation, although such analysis is beyond the scope of this work.

The distribution of radio sources inside galaxy clusters is quantified in terms of the radio luminosity function (LF). The latter is difficult to define in a robust manner because it is very sensitive to how the cluster volume is defined. It was first constructed by Ledlow & Owen (1996) from a VLA survey of Abell clusters (Abell 1958, Abell et al. 1989), and later by Reddy & Yun (2004) and Massardi & De Zotti (2004) for larger cluster samples. Because of the limited number of cluster detections, there has been little research on the cluster source distribution at high redshifts ($z > 0.4$). In particular, the published results are consistent with no luminosity evolution with redshift in the limited samples so far considered (Stocke et al. 1999, Coble et al. 2006).

In recent years, deep optical and X-ray surveys have provided large cluster catalogs at high redshifts, making it possible to constrain the AGN population with statistical significance at different redshifts. This chapter compares the results from high redshift samples to those coming from larger samples at low redshift.

4.2 Cluster Samples

The clusters selected for this study come from publicly available catalogs of X-ray and optically selected clusters. To make a mostly unbiased comparison possible, both X-ray selected and optically selected cluster samples have been chosen, as far as possible, for each redshift range considered.

At low redshifts the largest cluster sample is obtained from the C4 cluster catalogue (Miller et al. 2005), which consists of 748 clusters distributed over 2600 deg^2 of sky in the redshift range $0.02 < z < 0.17$. In the X-ray domain the Northern ROSAT All-Sky (NORAS) cluster catalogue is used (Böhringer et al. 2000). The latter provides a sample of 456 clusters with known redshifts and X-ray luminosity at $0.003 < z < 0.46$. All clusters in these catalogs are covered by the VLA NVSS survey (Condon et al. 1998), and about two thirds of them are also covered by the VLA FIRST survey (Becker et al. 1995).

At high redshifts, the only optically selected cluster catalogue is the RCS sample (Gladders & Yee 2005) which was also discussed in chapter 3. Publicly available cluster catalogs from two fields, RCS $0926+37$ and RCS $1327+29$, covering approximately 10 deg^2 and containing $241 + 184$ clusters in the redshift range $0.20 < z < 1.36$ (photometric redshifts) are used. Groups of low mass ($M_{200} < 10^{11} M_\odot$) have been removed from the sample. The X-ray sample for high-redshift clusters is taken from the ROSAT 160 square degrees survey (Mullis et al. 2003). Clusters with redshifts $z < 0.4$ are removed, as are clusters not covered by the NVSS survey. The resulting sample of 43 clusters with $z \geq 0.4$ is extended with high-z clusters from the WARPS survey (Perlman et al. 2002), the XMM-LSS survey (Valtchanov et al. 2004) and XMM-Newton archive data (Andreon et al. 2005), yielding a total of 56 clusters with known redshifts and $0.1 - 2.4$ keV X-ray luminosities.

The final cluster sample used in this study is the recently published catalogue of 13,823 clusters extracted from the Sloan Digital Sky Survey (SDSS) using the maxBCG method (Koester et al. 2007). This is by far the largest homogeneous cluster sample available today, and the redshift range ($0.1 < z < 0.3$) is similar to that of the sample used in other recent studies (e.g. Massardi & De Zotti 2004, Lin & Mohr 2007).

The distributions of mass and redshift in the different samples are shown in Figure 4.1. The distribution of the X-ray selected NORAS clusters is typical for flux limited samples. The mass of the X-ray selected clusters are derived from their $0.1 - 2.4$ keV band luminosity using the scaling of Reiprich & Böhringer (2002) as

$$\log\left(1.4^2\ L_{\rm X}\right) \ = \ A \ + \ \alpha \log\left(1.4\ M_{200}\right), \tag{4.1}$$

where M_{200} is the mass enclosed within r_{200}. The factors 1.4 come from the choice of the hubble parameter as $h = 0.72$, and the constants A and α are chosen following Lin & Mohr (2007). The masses of the optically selected clusters are estimated from the richness parameter $B_{\rm gc}$ following Yee & Ellingson (2003) as

$$M_{200}\ (h_{70}^{-1} M_\odot) \ = \ 0.7 \times 10.05\ B_{\rm gc}^{1.64}. \tag{4.2}$$

The SDSS C4 cluster catalog provides the line-of-sight velocity dispersion, σ, for the clusters, from which the richness parameter $B_{\rm gc}$ can be estimated (Yee & Ellingson 2003) as

$$\log\sigma \ = \ 0.55\ \log B_{\rm gc} \ + \ 1.26. \tag{4.3}$$

Koester et al. (2007) provide a best-fit relation between the line-of-sight velocity dispersion and the scaled richness parameter $N_{\rm gal}^{r_{200}}$, defined as the number of E/S0 galaxies within r_{200}, as

$$\log\sigma \ = \ 2.40 \ + \ 0.31\ \log N_{\rm gal}^{r_{200}}. \tag{4.4}$$

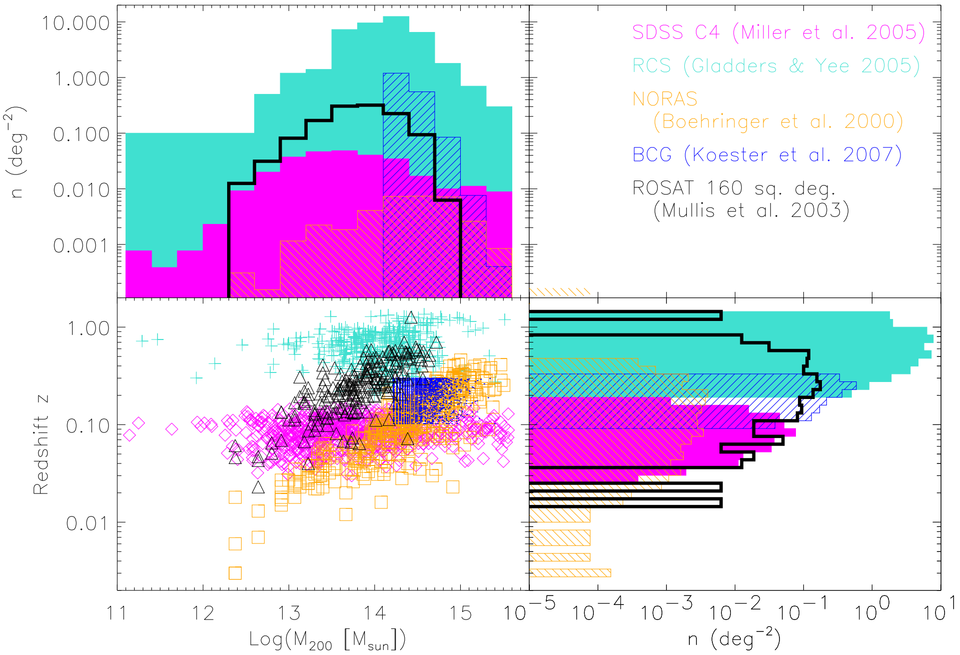

Figure 4.1: Redshift and mass distributions of the cluster samples used in constructing the radio luminosity function. Virial masses are obtained using the scaling relations described in the text. In the lower left scatter plot, the crosses represent the optically selected RCS clusters, diamonds the SDSS C4 clusters, boxes the NORAS clusters, dots the BCG clusters and triangles the ROSAT clusters. The lower right and upper left panels show histograms of the redshift and mass distributions, in the corresponding colors, respectively. Note that from the ROSAT sample, only clusters of galaies with $z > 0.4$ are considered when constructing the luminosity function, although the complete sample is shown here.

The sharp cut-off at the low mass end (Fig. 4.1), comes from the threshold in richness for the cluster catalog, $N_{\rm gal}^{r200} \geq 10$. It is claimed that the BCG sample is 90% complete above this cutoff limit, although the relative number of high-mass clusters is smaller when compared to the C4 sample; thus more work is needed to analyze and compare this catalog with respect to other data. In spite of uncertainties in the completeness and scaling relations pertaining to this catalog of clusters, the *shape* of the radio LF obtained from this sample can be reliably compared to the LF shapes derived from other data sets.

Comparing the optical or X-ray cluster samples at high and low redshifts, it can be seen that there is a relatively higher abundance of high-mass clusters in the low-z data sets. This is to be expected from the hierarchical structure formation scenario, and the fact that the selected X-ray and optical cluster samples independently show this behavior gives some indication that direct comparisons between the samples in terms of their radio luminosity functions are meaningful.

The virial radius of a clusters is related to its mass according to (e.g. Kitayama & Suto

1996)

$$M_{200} \equiv (4\pi/3) r_{200}^3 \rho_c(z), \tag{4.5}$$

where r_{200} defines a region whose mean over-density is 200 times the critical density $\rho_c(z)$ of the universe at that epoch. The virial radius, typically smaller for optically selected clusters, becomes important when constructing the radio luminosity function (§ 4.4), where the search volume for radio sources inside a cluster is defined by the virial radius, instead of using a fixed volume for all clusters.

4.3 Radio Source Distribution

This section describes the selection of radio sources and their projected number density profile inside galaxy clusters. Radio source information comes from archived VLA data (FIRST and NVSS surveys, see previous section), with no information on individual redshifts. Over-densities are thus quantified in terms of the angular density of radio sources near cluster centers. These counts can be converted to projected number densities in physical units (Mpc from the cluster center) using the known redshift of the cluster. The resulting density profile is much narrower than the overall distribution of galaxies. Indications of this have been noted before (e.g. Massardi & De Zotti 2004), but in spite of this the overall distribution has been used by most authors to derive the radio LF in clusters.

4.3.1 Selection of Radio Sources

To search for radio sources associated with clusters, the VLA FIRST survey is used wherever possible. Both RCS patches are completely covered by the FIRST survey, as are almost 90% of the clusters from the C4 (SDSS) catalog. The C4 clusters not covered by FIRST are discarded. For the ROSAT 160 square degree and other high-z X-ray selected clusters, which are distributed all over the sky, the NVSS radio catalog is used in order to retain a statically significant sample. For consistency, the comparison between high- and low-z X-ray clusters is therefore done with the radio source data from NVSS.

There are two reasons why the FIRST catalog is preferred over NVSS. First, the better resolution of the FIRST survey ($5''$ as compared to $45''$ for NVSS) reduces confusion and resolves out extended radio emission. In extrapolating the 1.4 GHz radio LF to higher frequencies, the dominant factor is flat (or inverted) spectrum sources, typically the core component of AGN. Thus, using the radio LF derived from NVSS to obtain radio properties at high frequencies is misleading. Systematic differences between results obtained using the FIRST and NVSS data are discussed in § 4.5. Second, the FIRST flux completeness limit, defined as the point source flux density above which the survey is 99% complete, is 1.5 mJy, compared to 3.5 mJy for NVSS.

A radius of 3 Mpc at the cluster redshift is used to search for radio sources. The radius r is converted into an angle on the sky, θ, using the angular diameter distance D_A according to

$$r = \theta\, D_A(z, \Omega_M, \Omega_\Lambda, h), \tag{4.6}$$

using the cosmological parameters of Komatsu et al. (2008). To avoid counting the same radio source twice, partially or fully overlapping clusters (within a radius of 1.5 Mpc in either physical frame) are not considered. To compute radio luminosities, the integrated flux densities from the radio data are used, assuming isotropic emission.

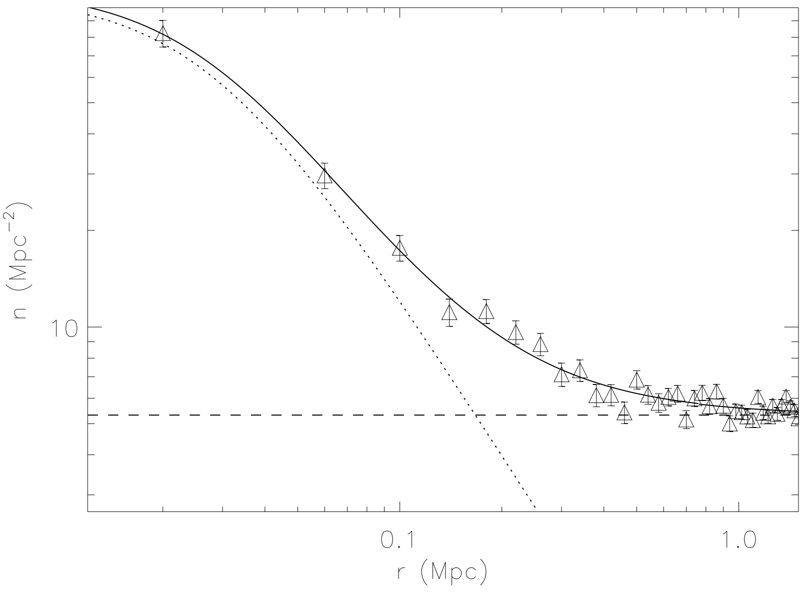

Figure 4.2: Projected 1.4 GHz radio source counts from the FIRST catalog around the cluster centers in the NORAS sample. All distances have been transformed to physical units using the cluster redshifts. The solid line is a fit to an isothermal β model plus a constant background/foreground. The dashed line shows the background level (see text), and the dotted the beta profile only.

4.3.2 Radial Density Profile

The transformation from angular to physical projected distance can be unambiguously done only if the redshifts of the sources are known. However, since there is a significant over-density of sources near cluster centers, the density profile can still be constructed in the physical frame within clusters by assigning the redshift of the respective cluster to sources within a physically meaningful cluster radius. Thus, the projected number density of radio sources can be quantified in terms of their distance from the cluster center, whereas the uniform distribution of “field” sources is constant and can be subtracted. The result of such a computation is shown in Figure 4.2, which clearly demonstrates how the cluster radio sources stand out against the background.

Transforming the angular to physical distances in each cluster field in the sense of Eqn. (4.6) is physically meaningful only for those sources actually associated with the clusters. Nevertheless one can define a “field density in the physical frame”, which is uniquely defined for the ensemble of cluster redshifts in a sample and constant with radius. This quantity can be converted into a true projected angular field source density, knowing the redshifts. Because we are only interested in the statistical distribution of the cluster sources, the density of the field sources can be ignored, as long as the search radius is chosen large enough to separate the two components.

To model the cluster radio source distribution, an isothermal beta profile (§ 2.2.4) is used, which makes a simple de-projection into volume number density very simple.

It should be noted that for the purpose of constructing the radio LF, the exact form of the fitting function is not important; although the density profile is used in constructing the radio LF as discussed in the next section, the LF is only very weakly sensitive to the parameterization of the source density fitting function.

Figure 4.2 shows that the radio sources inside clusters are much more concentrated than the overall galaxy population, with typical scale radii on the order of 30-80 kpc. The optical cluster samples show broader galaxy profiles than the X-ray selected samples, which may be due to greater uncertainties in the central positions of optically selected clusters.

Reddy & Yun (2004) also used the isothermal β model to describe the source density of radio sources in seven nearby clusters and found a core radius of $r_c \sim 700$ kpc (with $\beta \sim 0.8$-0.9, similar to what is found here), clearly inconsistent with the current results. However, for clusters at $z > 0.1$, the FIRST and NVSS catalogs typically only show the brightest radio sources inside clusters, which are usually the AGN located near the cluster centers. In contrast, the radio galaxy sample used by Reddy & Yun consists mostly of starburst galaxies, as their cluster sample is at very low redshift. A 1.4 GHz flux density limit of 3 mJy at redshift $z = 0.2$ corresponds to a radio luminosity $\log(L_{1.4\mathrm{GHz}}) = 23.5$, and only 3 sources out of 114 in the radio galaxy sample of Reddy & Yun have a luminosity above this value. The starburst galaxies are expected to be distributed more like the general cluster galaxy population than AGN; therefore their surface density profile is much broader than that seen in the present samples. Massardi & De Zotti (2004) use a β profile similar to that of Reddy & Yun, although their sample suggests a much narrower distribution.

Figure 4.3 shows the distribution of radio sources (using the FIRST data set) for the maxBCG cluster catalog, by far the largest cluster sample available. It is clear that the distribution has at least two components. To explain this, one should note that the catalog uses the coordinate of the central brightest cluster galaxy (BCG) as the cluster center. In fact, the central narrow distribution is consistent with radio sources residing in the BCG, since the width of a Gaussian fitted to the distribution is consistent with the position uncertainty of the FIRST survey (which at the median redshift of the sample, $z = 0.2$, corresponds to about 3 kpc).

The second, broader, profile for the cluster radio sources in this sample is also smaller than the one shown in Figure 4.2. This can be explained by the typical separation between X-ray centers and the brightest cluster galaxies, which Koester et al. (2007) estimate at around 0.1 Mpc. Adding a random positional uncertainty equivalent to this amount to the maxBCG cluster sample yields a radial distribution that well agrees with the one found from the X-ray selected cluster sample.

4.3.3 Mass-Luminosity Correlation

Best et al. (2007) have demonstrated the prevalence of AGN activity in BCG. Brightest cluster galaxies tend to lie close to the center of the potential wells of clusters and are more luminous than normal ellipticals. Moreover, their properties correlate strongly with their host clusters. It has been shown that BCG are about an order of magnitude more likely than other ellipticals to host AGN (Edge 1991, Lin & Mohr 2004), which can explain the strong clustering of radio loud galaxies near cluster centers.

Conversely, it has also been shown that powerful radio sources are almost exclusively found in luminous elliptical galaxies (Ledlow & Owen 1996). The analysis of Best et al. (2007) shows that galaxies having velocities within two standard deviations of the mean velocity (with respect to the velocity dispersion) and within $0.2\, r_{200}$ of the cluster center have an enhanced probability to host a radio loud AGN. Based on this, it is likely that the brightest radio galaxies considered in this work are associated with BCG in clusters, and in addition to the correlation

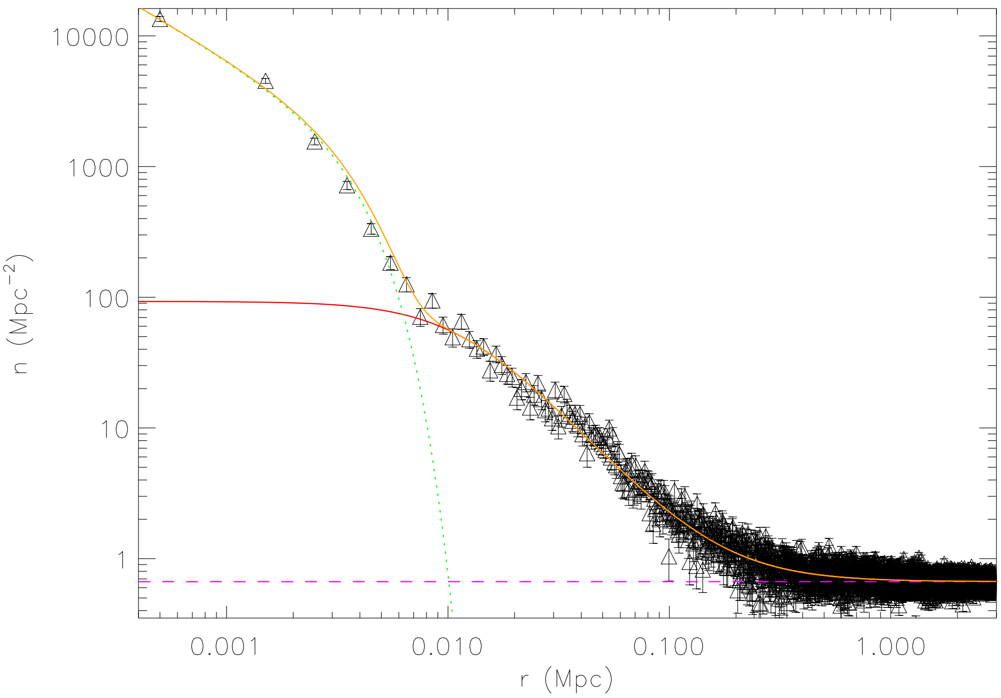

Figure 4.3: Projected number density profile of the FIRST radio sources for the maxBCG cluster catalog. The catalog takes the cluster center as the position of the most luminous BCG, which often also hosts a bright radio source. The excess over a β profile in the innermost part ($<$ 10 kpc) is fitted with a Gaussian, and is consistent with the pointing uncertainty in the FIRST catalog. It does thus not necessarily indicate the presence of an additional narrow component.

between BCG luminosity and cluster mass (Lin & Mohr 2004) it is also reasonable to expect that 1.4 GHz radio luminosities of the central AGN are correlated with cluster mass. This is the reason why r_{200}, rather than a fixed radius, is used in computing the volume averaged radio luminosity function in the next subsection.

Without any redshift information for the radio sources in the present samples, the computation of source luminosity and its correlation with the cluster mass is prone to error. However, by selecting sources only within a small radius from the cluster center, where the over-density of cluster sources is substantial compared to the field, it can be assumed that the sources are associated with the clusters so that luminosities can be computed. The field component is subtracted statistically, and will thus contribute only as an enhanced dispersion in the luminosity-mass correlation.

The luminosity of a radio source is computed as

$$L_{1.4\mathrm{GHz}} \;=\; (4\pi\; D_L^2)\; S_{1.4\mathrm{GHz}}\, \frac{\mathcal{K}(z)}{(1+z)}, \tag{4.7}$$

where $S_{1.4\mathrm{GHz}}$ is the integrated flux density taken from the VLA catalog (FIRST or NVSS), D_L is the cosmological luminosity distance, and $\mathcal{K}(z)$ is the K-correction term for non-thermal radio sources. For the computation of the K-correction it is assumed that at 1.4 GHz, 30% of the sources have flat spectra with with a mean spectral index of 0.0, and 70% of the sources have steep spectra with a mean spectral index of 0.8, where the flux density follows $S_\nu \propto \nu^{-\alpha}$ (cf. Holdaway & Owen 2005). The contribution from this correction is about 10% for sources at $z = 0.2$ and 30% at $z = 0.6$.

In figure 4.4, a correlation between the radio luminosity and the cluster mass can be seen in the X-ray sample, scaling roughly as $L_{\rm tot} \propto M_{200}^{1.0\pm0.1}$ (note that the *scatter* in the distribution is much larger than the estimated uncertainty in the scaling relation, the latter only describing the mean properties of the distribution).

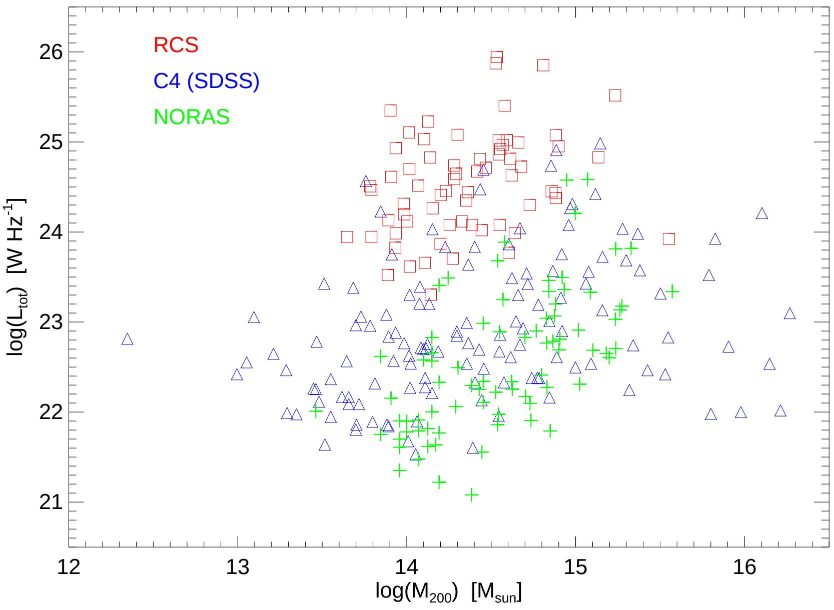

Figure 4.4: Correlation between radio luminosity and cluster mass, for three of the cluster samples considered. ($0.2 \lesssim z \lesssim 1.0$). Each data point shows the *total* radio luminosity from the radio sources within a fixed radius of $r_c = 500$ kpc and subtracting the mean background.

4.4 Construction of the Luminosity Function

The luminosity function $\rho(L)\ d(\log L)$ is the average *number* of radio sources per logarithmic luminosity bin ("magnitude") per unit physical volume of a cluster. Alternatively, one can use the power P per unit solid angle to construct the luminosity function.

Figure 4.5 illustrates schematically how the radio LF in clusters is constructed. For each cluster, a region within some physical radius from the center is searched for radio sources in a particular luminosity bin, using the cluster redshift to convert from flux to luminosity. Although the final result will not be particularly sensitive to the radius chosen, it is taken to be 300 kpc in accordance with the β profile of source counts described in the previous section. From the number of sources found within the search radius, the number of foreground/background sources, $N_{\rm bg}$, is subtracted by integrating the field number density within the flux range ΔS,

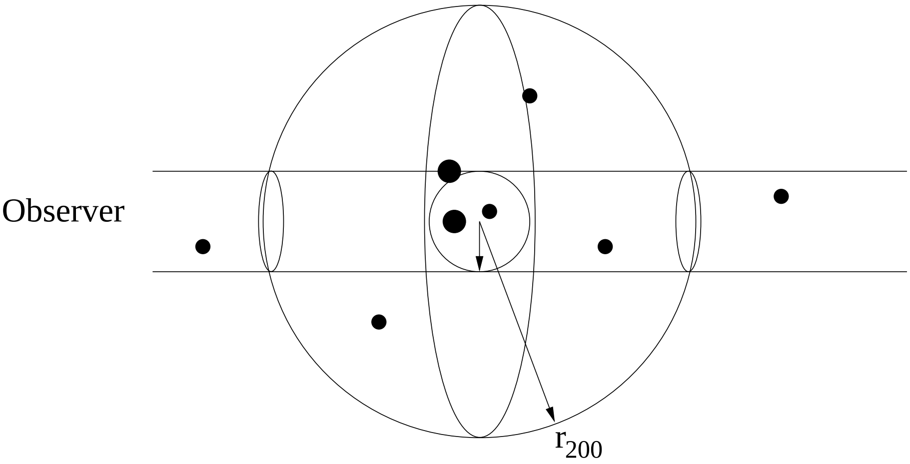

Figure 4.5: Illustration of the method used in obtaining source counts and volume for the computation of the luminosity function of radio sources inside clusters. For each cluster the *sampled* volume is the "line-of-sight cylinder" (radius $\sim$ 300 kpc, see text) The projected number density in this volume is converted to volume density of sources inside the cluster radius (taken as r_{200}) assuming a beta-profile for the volume density of sources.

corresponding to the luminosity bin ΔL, and multiplying by the area of the searched region. The field source density dN/dS at 1.4 GHz is obtained from fitting a functional form to the entire FIRST catalog above the completeness limit. The total number of *cluster* sources is thus $N = N_{\rm counted} - N_{\rm bg}$.

The total search volume is the sum of all cylindrical volumes, as shown in Figure 4.5, for all clusters for which the redshifts lie below a critical value given by the completeness limit of the radio survey. Denoting this volume $V_{\rm cyl}$, we shall have

$$V_{\rm cyl} = 2\pi r^2\, R_{200}\, N(z < z_{\rm cut}), \tag{4.8}$$

where $z_{\rm cut}$ is the redshift above which a source with luminosity L_0 (the central luminosity in a given luminosity bin) will have a flux below the completeness limit of the survey.

the number density of sources thus obtained is valid for the cylindrical volume along the line of sight (Fig. 4.5), and not for the actual cluster volume, which is defined as the sphere with radius r_{200}. To convert the source density inside the cylindrical volume to that inside the sphere, the beta profile from the previous section is used.

In the context of the isothermal β model, the physical (de-projected) density of the sources is given by (e.g. Sarazin 1988)

$$n \;=\; n_0 \left(1 + \frac{r^2}{r_c^2}\right)^{-\frac{3}{2}\beta}. \tag{4.9}$$

Assuming the total number of cluster sources inside the spherical volume is $N_{\rm tot}$, the conversion from cylindrical number density to spherical number density is

$$\frac{N_{\rm tot}}{V_{\rm sph}} = \frac{(N - N_{\rm bg})}{V_{\rm cyl}} \times \frac{N_{\rm tot}}{(N - N_{\rm bg})} \times \frac{V_{\rm cyl}}{V_{\rm sph}}, \tag{4.10}$$

where $V_{\rm sph} = (4/3)\pi r_{200}^3$ is the physical volume of the cluster within r_{200}. The first term on the right hand side of Eqn. (4.10) is the observed source density, the second term the ratio of source numbers inside the spherical and cylindrical volumes, and the last term is obtained from basic geometrical considerations as $(3/2)r^2/r_{200}^2$. Since $N_{\rm tot}/V_{\rm sph}$ in a given luminosity bin is the spatial density of the radio sources, the luminosity function can now be written as

$$\rho(L)\Delta L \;=\; \frac{3}{2}\left(\frac{r}{R_{200}}\right)^2 \; \frac{(N-N_{\rm bg})}{V_{\rm cyl}} \; \frac{\int\limits_{\rm sph} \rho(r\prime)dV}{\int\limits_{\rm cyl} \rho(r\prime)dV} \; \Delta L. \tag{4.11}$$

Equation 4.11 directly shows the importance of choosing a proper density profile for the calculation of the LF. If radio sources were uniformly distributed, there would be no correction term needed for converting the density inside the cylindrical volume to that in the spherical volume. On the other hand, for a very narrow distribution of sources, most cluster sources will be within the search radius, and the density correction term is the geometric volume ratio of the cylinder to the sphere. The amplitude of the luminosity function computed using a broad profile like the one used by Massardi & De Zotti or Reddy & Yun is more than three times higher than the one computed using the narrow profile used here (assuming other variables are fixed for the LF computation). This correspondingly increases the average total radio flux from clusters.

4.5 Source Confusion

Source confusion becomes important when the typical separation of sources is comparable to the angular resolution of the radio survey from which the LF is derived. In particular, a larger beam tends to overestimate the LF at the high luminosity end as several confused low luminosity sources appear as fewer sources with higher luminosity. This effect is redshift dependent through the conversion of angular to physical distance, which complicates quantifying a possible redshift evolution in the LF.

A simple way to quantify the effect of confusion on the LF is to compare the luminosity function as constructed from NVSS (angular resolution 45″) with that constructed from FIRST (angular resolution 5″), using the same completeness cutoff in both surveys. For this comparison a narrow redshift range of $0.15 \le z \le 0.18$ is used, and sources are selected from the NVSS and FIRST catalogs using the maxBCG catalog of cluster coordinates to ensure a sufficiently large statistical sample.

The NVSS based luminosity function can be reconstructed from the FIRST data in a simple way. For simplicity it is assumed that the FIRST sample is free of confusion; confusion is then introduced by applying a larger, fiducial, beam to the high resolution sample. This is done as follows: In each cluster field, the positions and flux densities of each source are recorded. The search radius is increased from the default search radius (previous section) by half the full-width half maximum (FWHM) of the fiducial beam. The brightest source is located, and all sources within the fiducial beam, with the position of the brightest source as the center, are combined into one source. The position of the new source is taken as a weighted average of its parts, and the total flux is the sum of the integrated flux of the parts. The next brightest source is then located, and the procedure is repeated until all sources have been covered. In this way, radio source samples can be simulated from the FIRST data to an arbitrary beam FWHM larger than 5″ (the resolution of FIRST). Figure 4.6 shows the result of a range of resolutions up to 45″. Even using this simple method, the result obtained from degrading

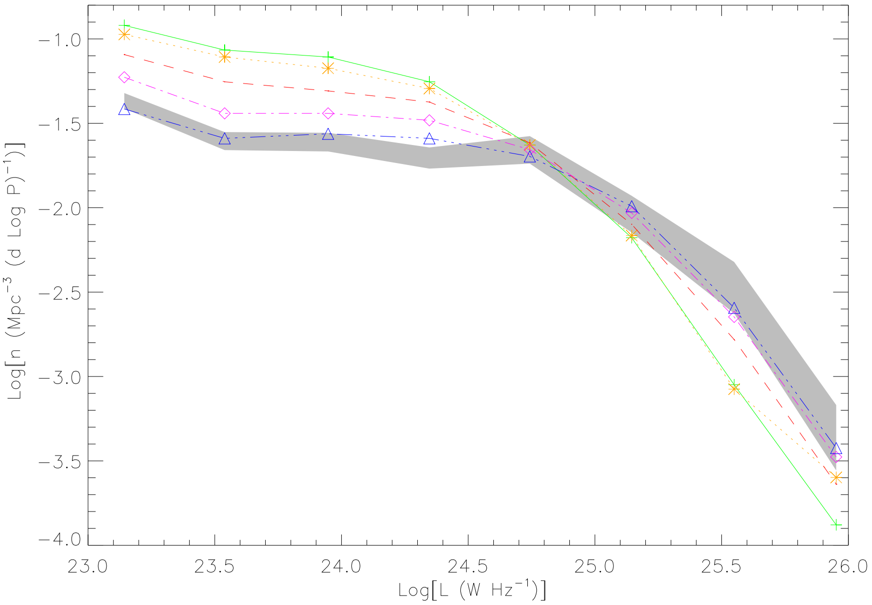

Figure 4.6: Result of artificially degrading the resolution of the FIRST sample of radio sources in maxBCG clusters ($0.15 \leq z \leq 0.18$) to generate mock source catalogs assuming larger values of the beam FWHM. The green solid line and points show the LF computed from the FIRST sample. Yellow (dotted), red (dashed), magenta (dash-dotted) and blue (dash-dot-dotted) lines and points show the results of degrading the resolution to $15''$, $25''$, $35''$ and $45''$. The last of these results is consistent, within statistical errors, with the LF constructed from the NVSS data (shaded region).

the FIRST sample to an effective resolution equal to that of NVSS is in agreement, within statistical errors, with the NVSS counts.

As an improved method, one could instead use the raw maps of cluster fields from the FIRST survey and degrade them to the NVSS resolution before extracting sources. However, this requires a robust source extraction in both maps and is quite complicated for faint sources near the completeness limit of the surveys.

The results presented here will be used to compensate for confusion bias between different redshift bins in quantifying the redshift evolution of the luminosity function in the next section.

4.6 Results

The luminosity functions obtained from the various cluster samples are presented here. r_{200} is fixed as the radius for computing the volume averaged radio LF. Bias due to confusion is compensated for by downgrading the resolution as described in the previous section; for any given cluster sample (or a set of samples to be compared), the resolution at each redshift is degraded so as to correspond to the original survey resolution at the redshift where a given physical size corresponds to the smallest angular scale.

4.6.1 Comparison with Field

Figure 4.7 shows how the radio LF in clusters of galaxies compares to that averaged over the sky in a local sample (Condon et al 2002). For the local sample, AGN can be differentiated from starburst galaxies, revealing two distinct contributions to the radio LF. Above a luminosity of 10^{23} W Hz^{-1}, the radio LF is dominated by AGN. One can therefore also expect that the AGN population dominates the LF in high redshift samples since AGN are much more luminous than starburst galaxies, and the latter drop below the survey completeness limits at high redshifts.

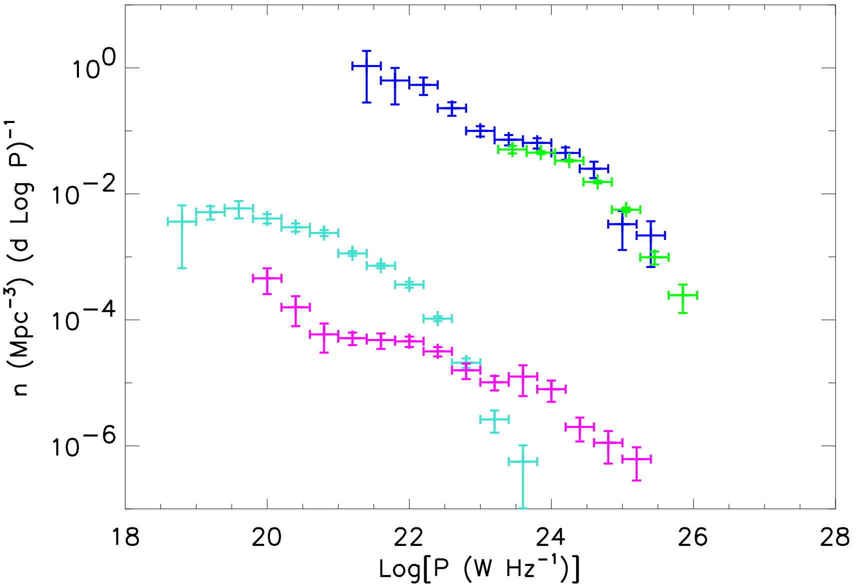

Figure 4.7: Luminosity function for cluster radio sources (blue and green), compared with the corresponding luminosity function for the local universe field sample of Condon et al. (2002). Cyan data points represent the contribution from starburst galaxies, magenta data points the contribution from AGN. For the cluster luminosity functions, blue is the LF derived from the sample of Massardi & De Zotti 2004 (scaled to the conventions used here) and green represents the LF derived from the total BCG sample ($0.1 \leq z \leq 0.3$).

4.6.2 Comparison Between X-ray Selected and Optically Selected Samples

The large number of clusters ($\sim 14,000$) in the maxBCG catalog yields by far the lowest statistical errors of all cluster samples considered. To test the robustness of the LF computed from the sample, however, it is necessary to compare it with the results from the other optical samples and the X-ray samples. Figure 4.8 shows the LF computed from the maxBCG sample compared with that of the C4 sample. The C4 catalog has a mean redshift lower than maxBCG, which can explain its higher amplitude in the lower luminosity bins, as the C4 sample is likely to include a larger number of starburst galaxies (cf Fig. 4.7).

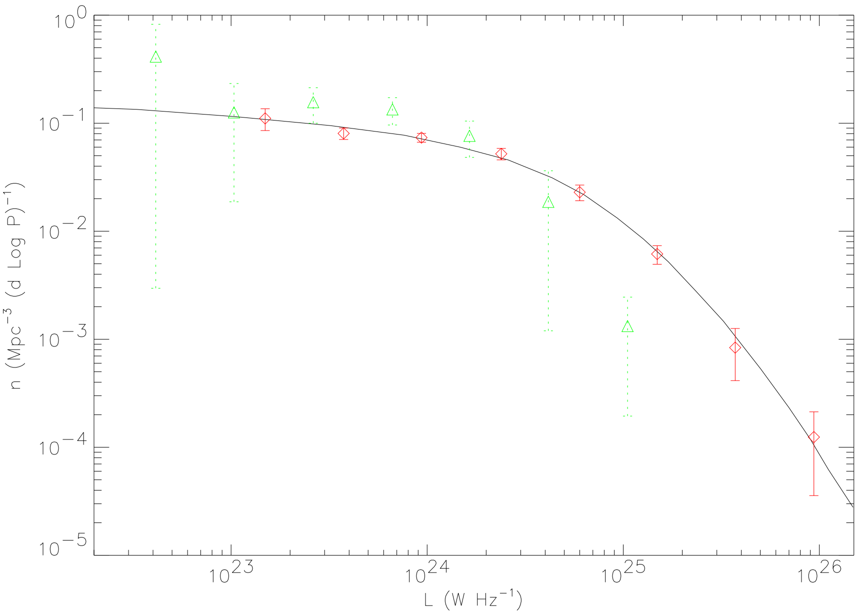

Figure 4.8: Comparison of the cluster radio LF computed from the C4 (triangles with green error bars) and maxBCG (diamonds with red error bars) samples. The solid line is a fit to the maxBCG sample with a Schechter function (Eqn. 4.12). The C4 LF is consistent with this fit within statistical uncertainties.

To find a parametric form for the LF, the data is fitted with a Schechter function (Schechter 1976) of the form

$$\rho(L)\Delta L = \rho^{*}\left(\frac{L}{L^{*}}\right)^{\alpha} e^{-\frac{L}{L^{*}}}\frac{\mathrm{d}L}{L^{*}}, \tag{4.12}$$

where the free parameters are ρ^* (a number count per unit volume), L^* (the "characteristic luminosity") and the power-law index α. Above $L = 10^{23}$ W Hz^{-1}, the C4 LF is consistent with a fit to the maxBCG LF, although the exact shape is somewhat different. The C4 sample is in this case too small to quantify the difference.

The NORAS and C4 cluster samples have similar redshift distributions; however the optical sample contains a larger fraction of low mass systems. In spite of this, the cluster luminosity functions from the two samples are consistent within statistical errors, as indicated in Figure 4.9.

No significant differences are found in the LF computed from the different samples, although the mass selection functions are quite different. Thus, particular attention will be paid to the maxBCG sample in the next section, which deals with the redshift evolution in the radio LF in clusters of galaxies, since it is the only sample large enough to decisively indicate such an evolution.

4.6.3 Redshift Evolution

Machalski & Godlowski (2000) quantified the redshift evolution of the LF under the assumption that the overall shape remains constant in time, an approach first suggested by Condon (1984).

Under this assumption, there can only be changes in overall luminosity and overall number density. The redshift dependence can then be written

$$\rho(L, z) \;=\; g(z)\; \rho\left[L f(z), z \approx 0\right], \tag{4.13}$$

where $g(z)$ quantifies the number density evolution, corresponding to a vertical shift ΔY in $\rho(L)\Delta L(L)$, and $f(z)$ represents luminosity evolution, corresponding to a horizontal shift ΔX:

$$\log\left[\rho(\log L, z)\right] \;=\; \log\left[\rho(\log L + \Delta X, z \approx 0)\right] \;+\; \Delta Y. \tag{4.14}$$

The vertical and horizontal shifts can now be fitted to yield $f(z)$ and $g(z)$. The assumption of shape preservation implies that number density and luminosity scale as powers of redshift; for the luminosity

$$L = L_0 \left(\frac{1+z}{1+z_0}\right)^{\alpha}, \tag{4.15}$$

where α is the power law index. A corresponding relation holds for the number density.

Although a hint of a redshift evolution can be seen from a comparison of the LF found for cluster samples with different redshift distributions (Fig. 4.9), it is possible that the different selection criteria can mimic such behavior; this preliminary result is presented here merely as a consistency check.

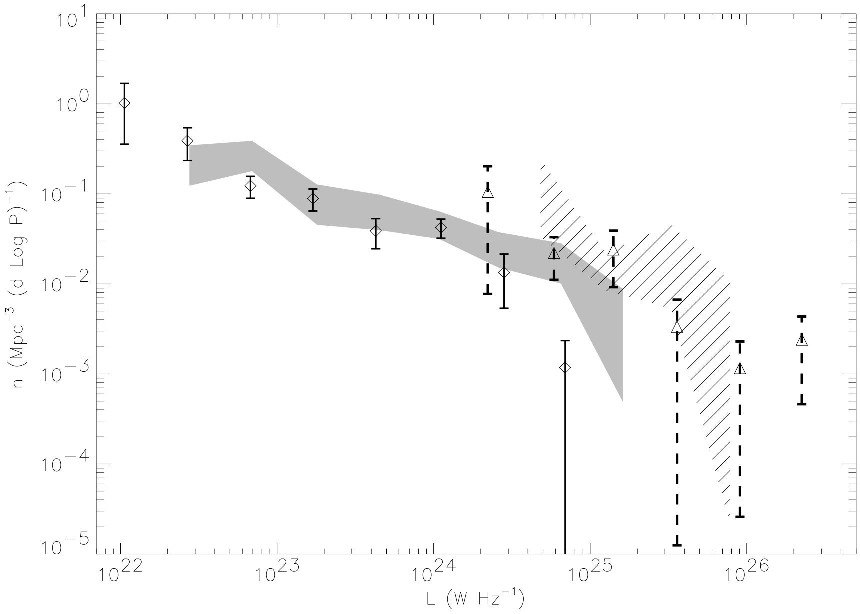

Figure 4.9: Redshift evolution of cluster radio sources through their radio LF. Results from optically selected clusters are shown as error bars; SDSS C4 (diamonds) and RCS (triangles). The redshift separation is $\Delta z \approx 0.4$ between the medians of the respective distributions. Results from the X-ray selected clusters are shown as the shaded (NORAS) and hatched (ROSAT) regions. For the X-ray sample comparison, only NVSS radio data has been used.

To make a more quantitative comparison possible, the maxBCG sample is divided into two redshift bins, with median redshifts $z = 0.13$ and $z = 0.23$, respectively (note that the two bins will contain a very different number of sources). The luminosity function is constructed from each of the two samples, the result of which is shown in Figure 4.10. Following the preceding discussion, the LF is constructed from the low redshift bin using Eqn. (4.12), and it is assumed that redshift evolution preserves the shape of the LF. Thus, the best-fit LF at the higher redshift is constructed by varying ΔX and ΔY in the sense of Eqn. (4.14) and minimizing a χ^2 statistic. To account for errors in the functional fits in both redshift bins, fiducial shifts ΔX_0 and ΔY_0 are introduced in the *low* redshift bin, and the χ^2 statistic is again minimized; this time only to find the Gaussian errors in the shifts (since the best-fit values of ΔX_0 and ΔY_0 are both zero by construction). The uncertainties in ΔX and ΔY can now be constructed by adding in quadrature the respective uncertainties from the two redshift bins.

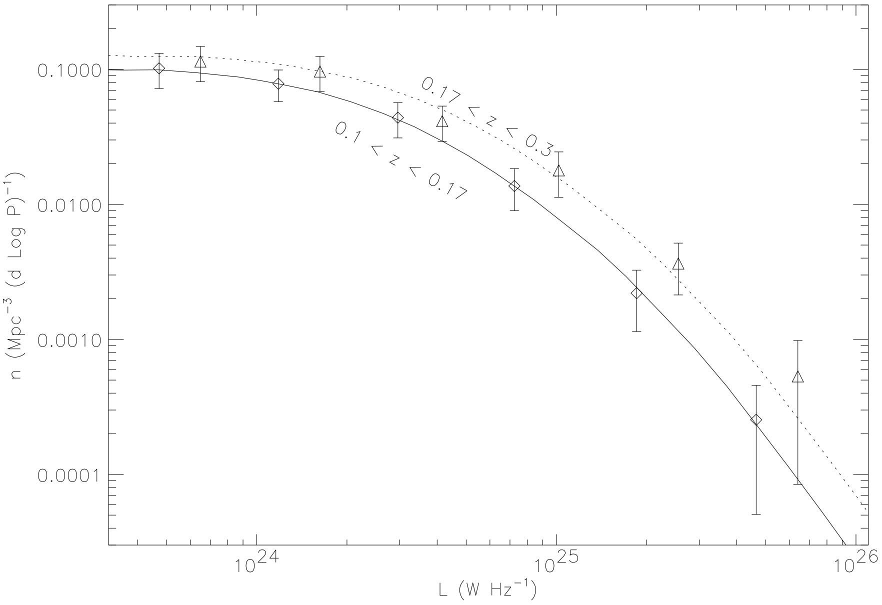

Figure 4.10: Redshift evolution of the radio LF in galaxy clusters using the maxBCG cluster sample and the FIRST catalog of 1.4 GHz sources. The solid curve is the fit to the low-z data set using Eqn. (4.12), while the dotted curve is the best-fit *shift* of this curve using Eqn. (4.14).

The data are neither consistent with a pure luminosity evolution nor a pure number density evolution. The average luminosity scales with redshift as $(1+z)^{3.3\pm1.2}$, and the number density as $(1+z)^{2.8\pm0.9}$ (cf. Eqn. 4.15).

4.7 Conclusion

In constrast to previous studies (Massardi & De Zotti 2004), a clear redshift evolution of the radio LF in galaxy clusters has been shown, with distinct components of both luminosity and number density evolution. The separation of the two components is made possible by the large sample of galaxy clusters up to $z = 0.3$ used here. Apart from the different normalization, the result is consistent with previous studies of the LF in the field population of galaxies, (Dunlop & Peacock 1990, Machalski & Godlowski 2000). The following discussion focuses on the two main results of this chapter, namely (i) the very narrow density profile of radio sources and (ii) the fact that redshift evolution of the cluster radio LF has not been clearly seen in previous studies.

In the work of Massardi & De Zotti (2004), a much broader density profile was assumed *a priori*, artificially assiging extra radio luminosity to the outer-lying regions of clusters. To prevent such bias, one can either use a narrow density profile, or correct for the sources in the central bin separately in the spherical cluster volume. The two approaches yield similar results. Furthermore, Massardi & De Zotti use a uniform cluster radius of 1.5 Mpc for their entire sample of clusters, the effect of which is to artificially assign a too large volume to the total sample and thereby decrease the amplitude of the luminosity function. It is more accurate to take cluster radii in accordance with their mass, which is why r_{200} has been used here. With this approach, clusters with no mass information have had to be excluded. However, without this approach a mass correlation for the density scale length and cluster radio luminosity could not have been established, and the redshift evolution information would have been suppressed.

The redshift evolution of the radio LF in galaxy clusters found in this study may be affected by bias due to cluster and radio source selection effects. However, the fact that a significant redshift evolution is seen in a homogeneous sample (maxBCG) after correcting for confusing bias, taken together with the agreement of the results with the field galaxy luminosity function of Machalski & Godlowski (2000), indicates that the redshift evolution is real, and a few notes on why previous authors have failed to detect it are in order.

In their study of radio sources in galaxy clusters at 30 GHz, Coble et al. (2007) limited their sample to the most massive X-ray selected clusters. In the present study, clusters selected through deep optical and X-ray survey were used, thus the samples used here contain many systems of lower mass (Fig. 4.1). It is possible that the redshift evolution seen in Figure 4.10 is due to the inclusion of this low-mass component. It is difficult to test this hypothesis, however, as mass estimates from optical richness tend to have a large scatter. The cluster sample of Massardi & De Zotti has a small redshift dispersion, centered around $z = 0.1$. The chance of seeing a redshift evolution is thus low, particulary considering the much smaller sample of clusters.

Chapter 5

Bolometer Arrays on the APEX Telescope

5.1 A Short Introduction to Bolometers

There are two basic ways of detecting radiation from the sky: direct (incoherent) detection, and coherent (heterodyne) mixing which preserves spectral information. Bolometers operate on the former principle, and are useful for sub-mm/mm continuum astronomical observations because of their high sensitivity combined with a relatively flat response over a wide bandwidth. For frequencies between tens of GHz and around 1.5 THz, bolometers are the most sensitive instruments to detect continuum radiation (e.g. Gildemeister et al. 1999)

A bolometer in its most basic form can be described as an absorber linked to a heat sink at a fixed temperature T_0 (*stage temperature* or *base temperature*) as shown in Figure 5.1.

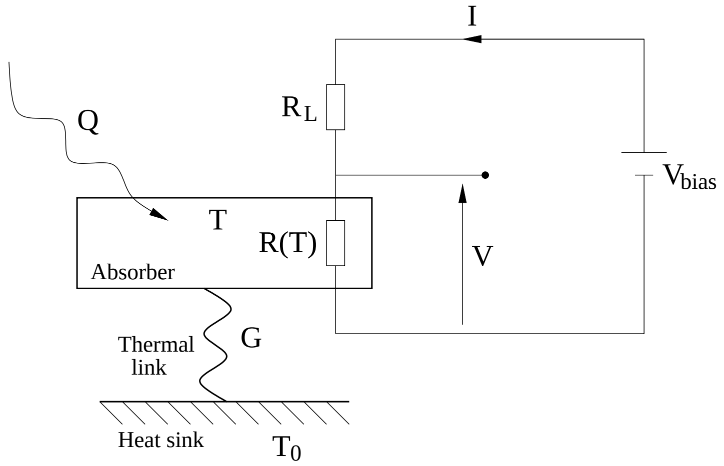

Figure 5.1: Schematic diagram of an ideal bolometer (see text).

Incident electromagnetic radiation of power Q is intercepted by the absorber, causing an increase in temperature $\Delta T = T - T_0$, resulting in excess power flowing through the thermal link, which has thermal conductance G. T (or equivalently ΔT) is measured through the change in the resistance $R(T)$, which in turn is detected as a change in the voltage V when applying a current I to the bolometer in series with a reference load R_L. The absorber is biased with with a voltage $V_{\rm bias}$, resulting in an additional power $Q_{\rm bias}$ in the absorber, and it holds that

$$\Delta T = \frac{Q + Q_{\rm bias}}{G}. \tag{5.1}$$

To achieve good sensitivity, the heat capacity, c, of the absorber should be small, as should the thermal conductance, G. It is also important that any change in temperature causes a change in resistance that is as large as possible. Thus, the bias voltage is chosen to maximize dR/dT, at the so-called *bias point* of the bolometer.

Superconducting transition-edge bolometers, such as APEX-SZ (§ 5.2), utilize the fact that dR/dT is extremely large at the transition of the absorber to superconductivity.

In a *semiconducting* bolometer, the resistance R of the absorber changes with temperature as

$$R(T) = R^* e^{\sqrt{T_g/T}}, \tag{5.2}$$

where R^* is a thermal model parameter and T_g is the band gap temperature of the conducting material. It also needs to be taken into account that the thermal conductance of the thermal link varies with temperature.

To achieve the best possible sensitivity, bolometers are cooled down to a fraction of a degree above absolute zero.

5.1.1 Noise

The NEP (noise-equivalent power) is the radiant power per square root bandwidth that produces a signal-to-noise (S/N) ratio of unity at the output of a detector. It can be written

$$\mathrm{NEP}^2 = \mathrm{NEP}^2_{\rm detector} + \mathrm{NEP}^2_{\rm background}, \tag{5.3}$$

where the detector contribution comes from Johnson and phonon noise, and the background contribution is due to photon noise (with a Poisson distribution) from the sky and the telescope. In practice, to achieve good sensitivity a bolometer should have a large bandwidth. However, this can degrade the performance because the background will also heat up the cooled device, i.e.

$$\mathrm{NEP}^2_{\rm background} = \mathrm{NEP}^2_{\rm photon} + \mathrm{NEP}^2_{\rm loading}. \tag{5.4}$$

Ideally, the overall NEP should be dominated by the thermal photon noise,

$$\mathrm{NEP}_{\rm detector} < \sqrt{2Qh\nu_0}, \tag{5.5}$$

where ν_0 is the frequency of the radiation.

5.1.2 Time Constant

A bolometer can be modeled using a first-order differential equation. From energy conservation it follows that

$$C\frac{\mathrm{d}\Delta T}{\mathrm{d}t} + G\Delta T = Q, \tag{5.6}$$

where $\Delta T = T - T_0$ and C is the thermal capacity of the absorber. For a constant Q, a constant temperature $\Delta T = \frac{Q}{G}$ is reached, so that $\frac{\mathrm{d}\Delta T}{\mathrm{d}t} = 0$.

Now assume the power flow is stopped after some time. Then after time t,

$$\Delta T = \frac{Q}{G} e^{-t/\tau}, \tag{5.7}$$

where $\tau = \frac{C}{G}$ is the thermal *time constant* of the absorbing element. This is a measure of the response time of the bolometer to incoming radiation.

5.1.3 Bolometer Arrays

To cover large areas of sky with good sensitivity, bolometers are usually combined into arrays. The APEX 12m telescope, located on the Llano de Chajnantor plateau 50 km east of San Pedro de Atacama in Northern Chile (Güsten et al. 2006), currently (2008) has two such arrays in operation: the APEX-SZ Camera (ASZCa) at 150 GHz and the Large Apex Bolometer Camera (LABOCA) at 345 GHz. Both are undersampled on the sky, meaning that even for the detection of sources with very limited extent, the array has to be moved around on the sky in some appropriate pattern to achieve full coverage. The two instruments, their modes of operation and their data are described in the following sections, which focus on observations.

Because bolometer cameras have multiple beams, words like *pixel*, *channel* and *signal* often cause confusion. Here, an individual bolometer will be referred to as a channel, while the word pixel is reserved for pixels in maps. *Signal* will refer to the time stream of an individual or several channels, depending on the context. The term bolometer will be used to denote any individual such, and a full array of the former will be referred to as either a bolometer array or a bolometer camera.

5.2 The APEX-SZ Camera

The APEX-SZ bolometer camera (Schwan et al. 2003, Dobbs et al. 2006) is one of the first superconducting transition-edge sensor (TES) bolometer cameras in operation. The APEX-SZ observing band centers on 150 GHz, where the atmospheric transmission is typically in excess of 95% at the APEX site (Peterson et al. 2003).

The detectors are so-called spiderweb TES bolometers (Schwan et al. 2003), employing voltage-biased transiston-edge sensors (Gildemeister et al. 1999), and are read out using superconducting quantum interference devices (SQUIDs, Lee et al. 1996).

The beam width of APEX-SZ is approximately one arcminute (full width half maximum, FWHM), which matches well with the spatial extent of the SZ emission from distant (redshift $z \sim 1$) galaxy clusters. The instrument was commissioned in 2006, and started science observations in early 2007. Until October 2008, nine galaxy clusters have been detected (chapter 7) and deep (10 μK rms per beam) surveys of several blank fields are in progress.

Data is sampled at a rate of 100 Hz. For the reduction of APEX-SZ data, there are two independent pipelines under development: the Bolometer Array Analysis (BoA) software developed in Bonn (chapter 6) and a pipeline written in MATLAB, developed by the North American collaborators of the APEX-SZ project. The two pipelines produce consistent results (see chapters 6 and 7), although the detailed steps for the optimal reduction of different types of data are still being worked out.

5.2.1 Array Parameters

It is important to distinguish between properties of a bolometer array as a whole and the properties of individual bolometer channels. While a telescope pointing correction applies equally to all channels, their individual channel offsets from some reference position must be determined one by one. The latter is a time consuming process, and is generally done at most once every day. Although the channel offsets stay relatively constant over time (the deviations seen over several weeks of observations are consistent with noise) other array parameters, such as gain and channel rms, need to be determined on a daily or close to daily basis as they show non-random variations on a time scale of days. All array parameters are determined from raster scans (see below) of bright point sources, usually planets. Such scans are time consuming because one needs to make sure each channel has sufficient coverage of the source so that the different array parameters can be extracted reliably.

As shall be seen in chapter 6, filtering out correlated atmospheric noise from data is a delicate process. Mars is typically bright enough to be recovered without any such filtering, but to get accurate estimates of beam parameters (such as individual calibration factors and point-spead functions), some correlated noise has to be removed. If it is known *a priori* what channels are optically active, the extraction of array parameters is a relatively simple process, but unfortunately this is not always the case. Dead or very noisy channels can seriously disturb the process of correlated noise removal, which necessitates an iterative approach to determining the array parameters. In a first reduction, only the channels with the best signal-to-noise ratios are considered (typically a third of the array). Then, successively more channels are added into the analysis as the properties of the sky noise of the particular observation are quantified properly.

Figure 5.2 shows the measured beams and relative gains (individual signal powers relative to the median value) for all the optically active bolometers, determined from observations of Mars in April 2007. The individual beams have similar FWHM and are approximately circular across the 0.4° field of view, with a mean measured beam FWHM of $58''$. The tertiary optics for APEX-SZ were designed for diffraction-limited performance, and the measured variations in beamwidth across the array agree well with predictions (Lanting et al. 2007).

Out of 330 channels on the array, 232 are read out. Of these, several are optically blind or are rendered useless due to extreme noise levels. Typically, around 200 channels are used as a starting point for a typical reduction. In the reduction of science data, more often than not additional channels are flagged for various reasons (see chapters 6 and 7).

5.2.2 Pointing Reconstruction

Using a large map (where every bolometer has some coverage of the source) of a point source such as Mars[1] and using the measured offset of each optically active channel in the array in telescope coordinates (azimuth and elevation offsets) from a reference center, it is possible to co-add all the signals from all the channels in the same system and generate a single map of the pointing source (or more generally any source tracked by the telescope). Note that this type of map is done only to determine the co-added beam of the instrument and to determine the position of each bolometer on the sky relative to the reference position. To apply pointing corrections for the telescope it is sufficient to make a smaller map where it is not necessary that all bolometer channels "see" the pointing source.

Figure 5.3 shows the beam shape as determined from the same Mars observations that were

---

[1] Note that the angulat extent of Mars can not always be neglected for APEX-SZ observations

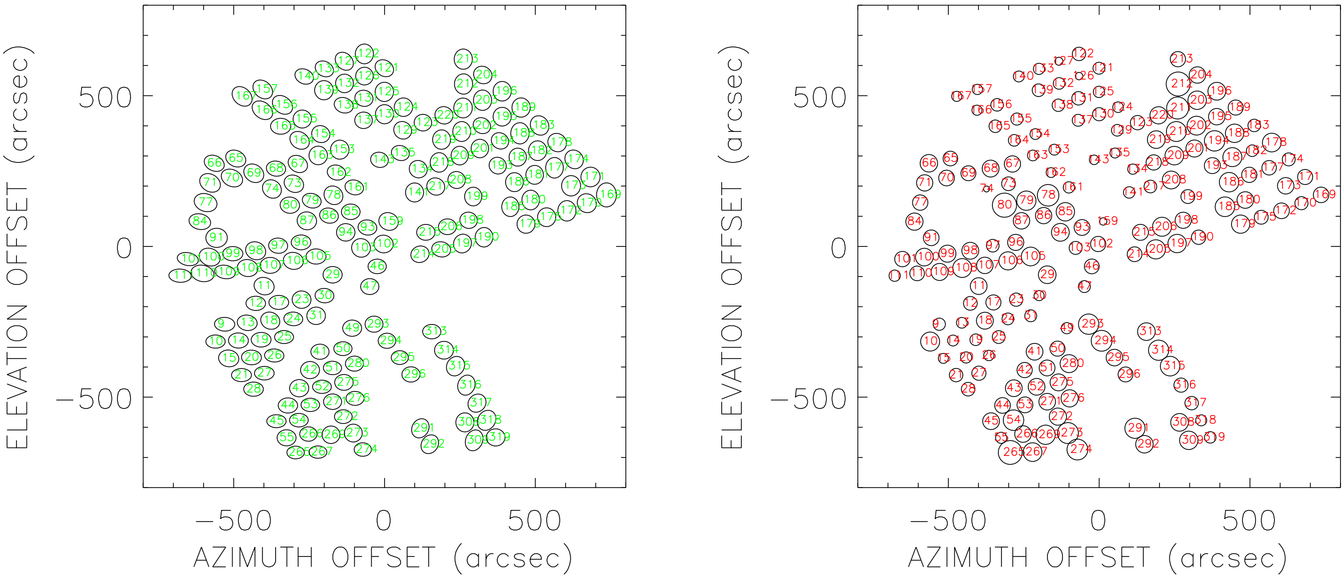

Figure 5.2: *Left:* Beam shapes for optically active APEX-SZ bolometers, determined from observations of Mars in April 2007. *Right:* Corresponding gains, represented as circles with radii proportional to the individual gains (arbitrary units).

used to compute the array parameters in Fig. 5.2. The beam is slightly elongated with a major axis of FWHM 59.6″ and a minor axis of FWHM 56.3″.

The FWHM of the total (co-added) beam, averaged over all angles, is 58.1″. At the time of the observations discussed here, Mars was effectively a point source for APEX-SZ; the semi-diameter of the planet was 2.44″, which is negligible in comparison with the derived beam FWHM.

5.2.3 Calibration

The APEX-SZ data is calibrated with daily raster scans of Mars that include all the elements of the array (cf. Halverson et al. 2008). From these observations, the gain, beam shape and position on the sky is determined for each bolometer as described in the preceding section. After applying relative gains to the Mars observations and correcting for angular offsets, a co-added rms weighted map is made using all optically active bolometers. This map is used to find an overall calibration factor.

The absolute flux of Mars is determined from an interpolation between the 350 μm data of Wright (1976) and the 3.3 mm data of Ulich (1981). Recent measurements from the WMAP satellite (Hill et al. 2008) indicate that the 1976 Wright model is consistently 10% higher than the WMAP measurements. Since the 350 μm temperature of Mars from the Wright model is within 7.5% of the 3.3 mm Ulich (1981) data (Griffin et al. 1986) in the spectral range 3.3mm-350μm, one can conclude that Mars is very nearly a blackbody in the mm/submm region. The

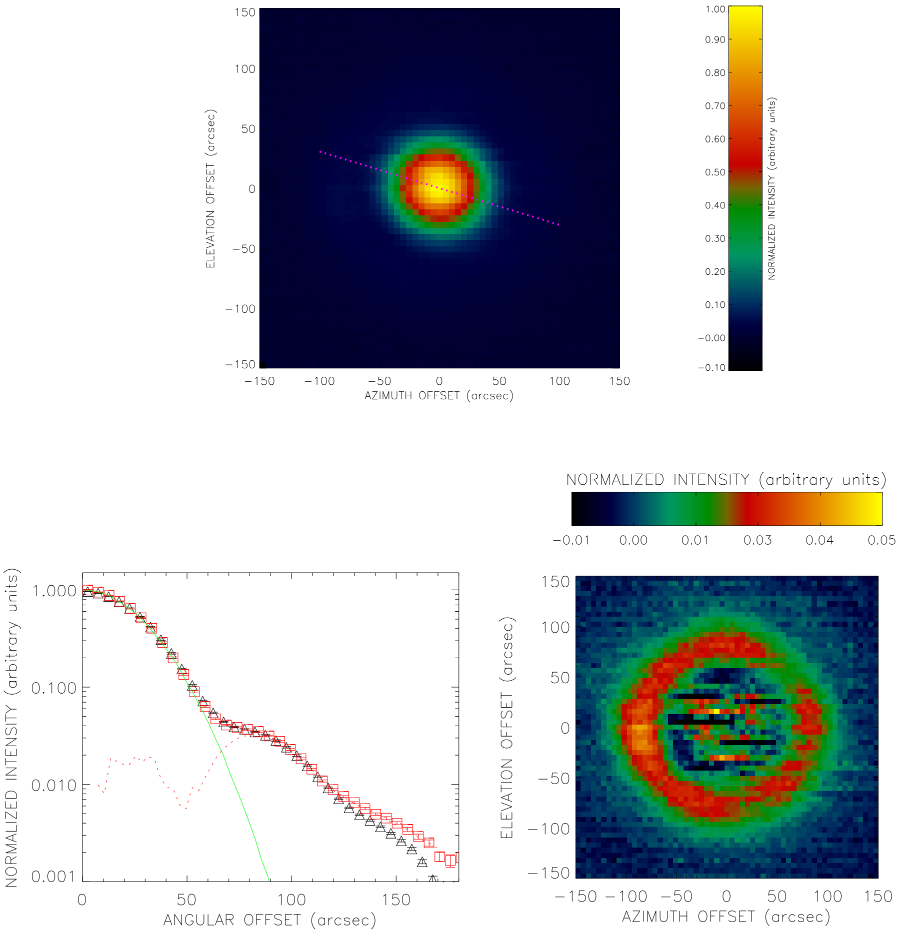

Figure 5.3: APEX-SZ beam shape (top) with the direction of the major axis indicated, and the beam profile averaged over all angles (left) determined from the same observations of Mars as in Fig. 5.2. The scan was reduced using a median sky noise removal algorithm (chapter 6), once with the source flagged out to an 180″ radius (triangles) and once applying the algorithm to the full set of data (squares). The solid line represents a Gaussian fit to the primary beam (major axis FWHM 59.6″, minor axis FWHM 56.3″; the major axis is inclined 17° with respect to the azimuth axis), and the dotted line is the residual. The figure on the right shows the map of Mars after subtracting the best-fit Gaussian, indicating side lobes of the beam.

flux density value for Mars at 150 GHz, obtained as described above, is thus scaled down by 10%. Following Griffin & Orton (1993), a 5 % systematic uncertainty in the absolute flux of Mars is assumed.

In addition to the overall calibration factor, an opacity correction term is applied. The zenith opacity is determined from skydip scans done every few hours. Because the atmospheric transmittance is typically better than 95% at the frequency of APEX-SZ, the uncertainty in calibration due to the opacity correction is estimated to be around 3%. An additional source of error is the uncertainty in the actual center of the frequency band that the bolometer array is sensitive to. Halverson et al. (2008) estimate the resulting calibration error at 1.4% for observations of the SZ effect.

On a time scale of days, variations in the gain stability of about 4% on individual bolometers is found. These drifts are random across the array, and taken together are negligible compared to the assumed systematic uncerteinty in the flux calibration.

The *total* systematic calibration uncertainty combining all the factors mentioned above is estimated at 6% by adding the errors in quadrature.

5.2.4 Low Frequency Drifts

Apart from atmospheric noise correlated across the array, APEX-SZ data has been found to exhibit strong uncorrelated drifts at low temporal frequencies. Major components of this residual noise can be identified with atmospheric components on scales of a few arcminutes (i.e. much smaller than the array), particularly in bad weather conditions (more than 2 mm of precipitable water vapor). Also, low frequency drifts have been identified from sine wave bias generators in the readout system. Due to lack of stability in the generators, small variations in the bias cause the individual signals to vary as well.

To deal with this problem, it is necessary to filter the data in frequency space. Butterworth filters applied to channel time streams have been found to work well, but emission from very extended objects will also be rejected by such filters. Ways to deal with such signal loss are discussed in chapter 6.

5.2.5 Glitches

The term *glitch* can have many meanings in the context of astronomical observations. Here the meaning is limited to spiky and jumpy signal behavior that is correlated across all or parts of the array.

Although glitches occur quite frequently in APEX-SZ data, the causes are not fully understood (and lie deeply in the context of the bolometer technology). Therefore a practical standpoint is taken, and glitches are classified by how they can be avoided. Then, there are two main types, namely (1) those remedied by zeroing the readouts of the bolometers and (2) those remedied by moving the telescope in azimuth (J. Mehl, personal communication). Despite slightly different behaviors of these two types of glitches, they can be effectively removed from data using a common algorithm (see § 6.3).

Figure 5.4 shows a typical example of a scan exhibiting glitches. As in this example, correlated noise removal algorithms (§ 6.2) will typically not remove glitches. There are two reasons for this. Firstly, there tends to be small delays (on the order of a few time stamps) between the onsets of the jumps or spikes in different channels. Secondly, jumps do not necessarily correlate in amplitude or sign.

5.2.6 Sensitivity

The expected sensitivity of an individual channel i is

$$\Delta T_{\mathrm{CMB}}^{(i)} = \frac{\mathrm{NET_i}}{\sqrt{t_{\mathrm{obs}}\,\epsilon\,\frac{A_{\mathrm{bolo}}}{A_{\mathrm{map}}}}}, \tag{5.8}$$

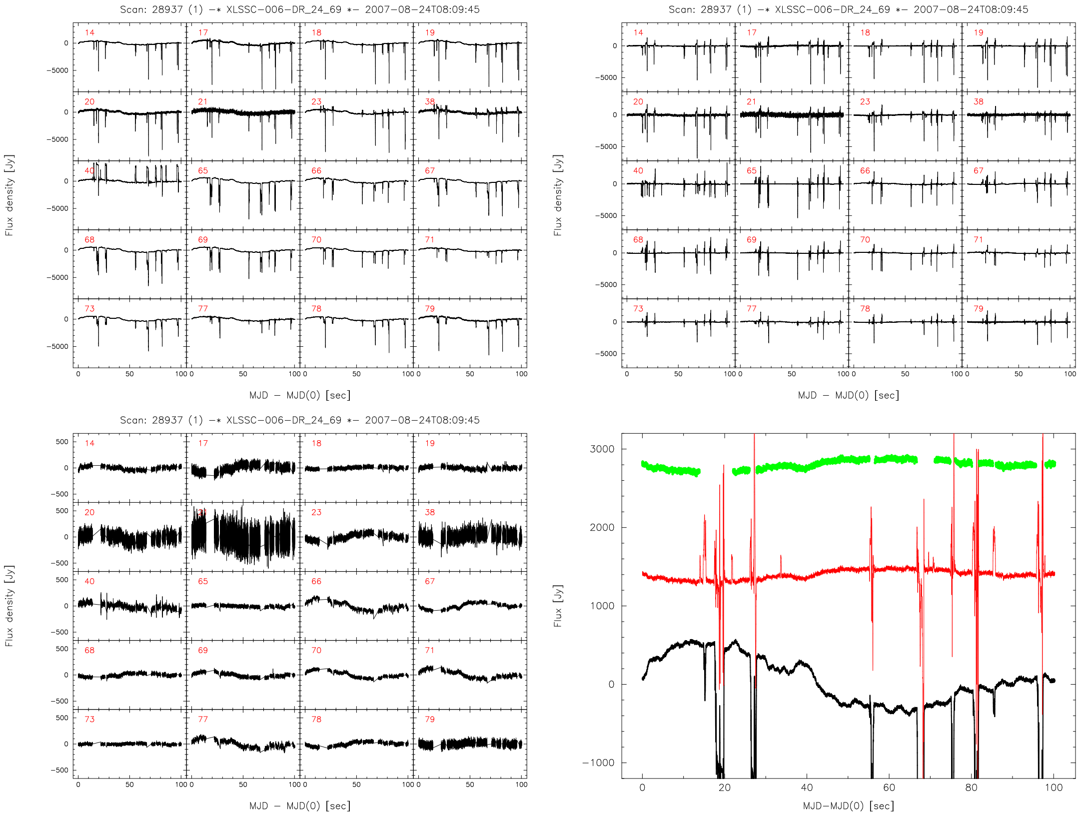

Figure 5.4: Example of a glitchy APEX-SZ scan from observations in August 2007. The raw time signals from a representative subset of channels are shown in the top left. The top right panel shows the same signals after the removal of correlated noise (§ 6.2). On the bottom left, the signal is shown after glitches have been removed by an iterative flagging scheme (§ 6.3). A closer look at a specific channel (numbered 67) is shown on the bottom right, with the signals shifted in the vertical direction for clarity. From bottom to top: raw signal (black), sky noise filtered signal (red) and glitch flagged signal (green).

where NET is the noise equivalent temperature of the channel, $t_{\rm obs}$ is the total observing time, ϵ the efficiency of the observations (time on sky divided by total time including overheads) and $A_{\rm bolo}$ and $A_{\rm map}$ are the channel beam and map areas, respectively.

Rather than converting to weights and summing up the contributions from all the channels, it will be assumed that most channels have similar NET. Then,

$$\Delta T_{\rm CMB} = \frac{\rm NET_{bolo}}{\sqrt{N_{\rm bolo}\, t_{\rm obs}\, \epsilon\, \frac{A_{\rm bolo}}{A_{\rm map}}}}, \tag{5.9}$$

where $N_{\rm bolo}$ is the total number of bolometers used to produce a given map. Using the median measured white noise NET (measured in the absence of a sky component, Dobbs et al. 2006), Eqn. (5.9) predicts a map sensitivity of $73\,\mu$K (thermodynamic) in one hour, assuming $\epsilon = 0.7$.

Comparing the theoretical rms to the rms in an actual map, however, is more complicated because in the above it has been assumed that the noise power spectrum is flat. This is in fact not the case; even after sky noise reduction and additional filtering most time streams exhibit a steepening in the low-frequency ($\sim 0.1 - 1$ Hz) regime. Thus, the map rms which is to be compared to the value given above will depend strongly on three distinct factors:

1. The slope of the power spectrum in time series space, which has been found to vary strongly with weather and airmass;
2. The frequency cut of the high-pass filter applied to the time series after sky noise reduction. This cutoff has to be decided on the basis of corresponding spatial scales (through the speed and shape of the scan pattern) considering the size of the emitting region;
3. The scale in the map at which the rms is computed.

For a complete treatment, one would have to consider the complete power spectra of the time signal and the map. Here, a simple treatment of noise in strongly high-pass filtered data is considered, and the rms is computed only on a scale close to the beam FWHM. To this end, a standard pipeline reduction (see chapters 6 and 7) is carried out on a set of scans of the cluster RXJ1347.5-1145 from April 2007. All frequencies corresponding to spatial scales larger than 3 arcminutes are filtered out from the time series, making use of the fast Fourier transform (FFT) and applying a Butterworth filter in frequency space. The chosen scans were observed as raster patterns in telescope coordinates, making a conversion between spatial and temporal scales unproblematic since the scan speed is nearly constant.

Before producing maps, the number of non-flagged time stamps in each scan are counted in order to allow accurate noise estimates as a function of integration time. Successively co-adding maps and smoothing to the scale of the beam, the map rms is then computed as the standard deviation of pixel values inside a region where the coverage is at least 60% of the maximum. The source region is blanked out before the rms computation. Figure 5.5 shows the resulting map rms measured in this way. In the first four hours, the noise scales down with the inverse square root of integration time, as expected. The presence of sources becomes evident after about five hours of integration.

The actual map rms, even in the "well-behaved" regions where the noise scales as expected, is about 40% higher than what is predicted from Eqn. (5.9). This can be attributed to so-called $1/f$ noise (e.g. Press 1978).

5.2.7 Scan Strategies

The APEX-SZ camera has been tested in several scanning modes, including small and large raster scans and circles with different radii. For observing galaxy clusters, the so-called "drift circle mode" (Fig. 5.6) has been found to give the most even coverage on the sky while allowing for an effective removal of atmospheric noise. In this mode, small circles (a few arcminutes in radius) are traced in the horizontal (azimuth and elevation) system, without tracking the source. After two minutes of observing, the telescope updates the central position of the circle to the (new) source position on the sky and lets the source drift through the pattern again. Alternatively, after two minutes one can start a new scan, but this increases overheads.

5.3 LABOCA - The Large Bolometer Camera

The Large APEX Bolometer Camera (LABOCA, Kreysa et al. 2003, Siringo et al. 2009), is a 345 GHz (870 μm) bolometer array developed at the Max-Planck Institut für Radioastronomie

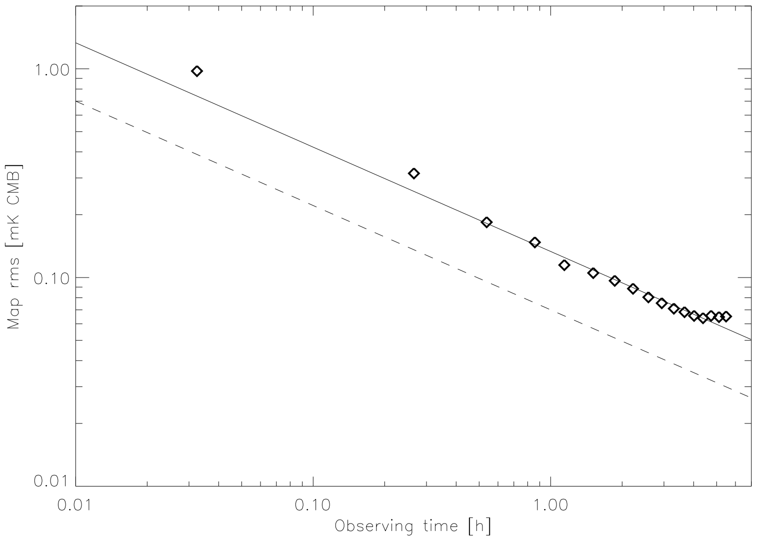

Figure 5.5: APEX-SZ map rms as a function of integration time, computed in a region chosen such that all map pixels in the region have a coverage (number of individual samples dumped into a certain pixel) of at least 60% of the maximum value. The solid line is a best-fit model scaling as the inverse square root of the integration time. The dashed line is the theoretical prediction (see text).

(MPIfR) in Bonn. It has been successfully used to map SZ emission with ∼20″ resolution over a field of view of several arcminutes with close to constant coverage (chapter 9).

The beam width of the co-added beam has been measured as 19.5″ (FWHM), consistent with the individual beams across the array which has a field of view 11′ across. LABOCA has 320 channels in total, about 230 of which are reliable and have low enough noise levels to be used for mapping. Channels are separated by two beams.

5.3.1 Calibration

The procedure for the calibration of LABOCA data is very similar to that of APEX-SZ data (§ 5.2.3). However, because Mars is partially resolved by the 19.5″ beam of LABOCA, Neptune is used as the primary flux calibrator at 345 GHz. In addition, secondary calibrators such as IRAS16293, G10.62, G34.3 and G45.1 are observed frequently (about once every hour) to monitor gain stability and to check the consistency in derived opacity corrections (see below). The secondary calibrator sources have been monitored by the LABOCA team since early 2007 and their 345 GHz flux densities are known to within about 6 % (Siringo et al. 2009).

For the absolute flux of Neptune at 345 GHz, again the approach of Griffin & Orton (1993), based on cross-calibration with Mars, is followed. The limiting factor in the absolute calibration is the model of Mars used, thus the systematic calibration error is again 5%. The absolute flux values derived from Griffin & Orton are scaled down by 10% to be brought into agreement with recent WMAP measurements (cf. § 5.2.3).

Opacity corrections are estimated from frequent (every few hours) skydip measurements combined with tau-meter measurements (the latter estimate the atmospheric optical depth at

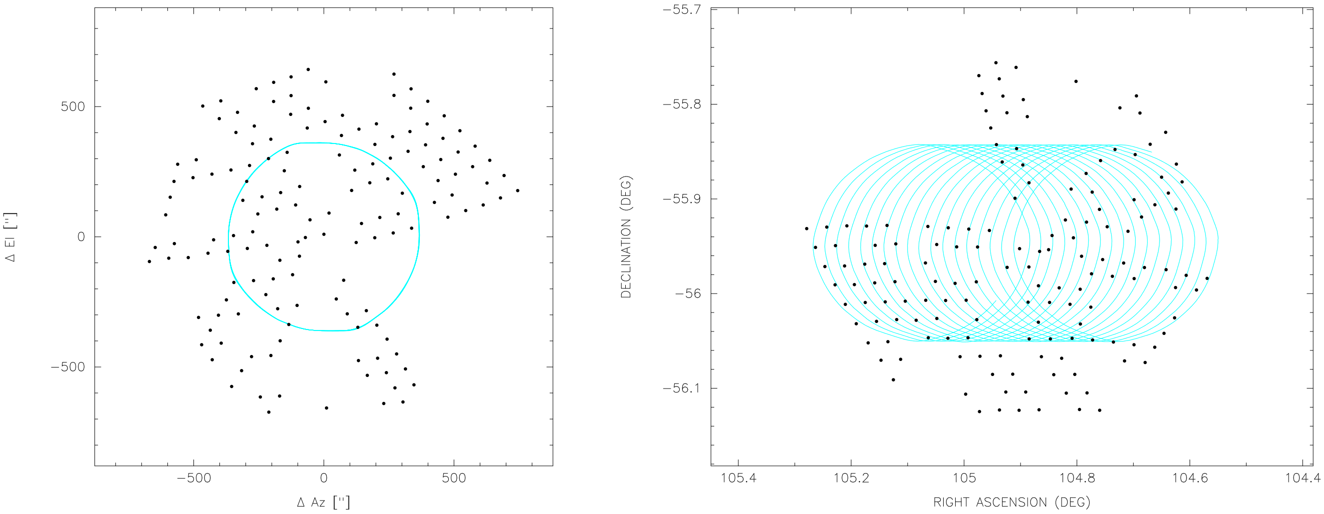

Figure 5.6: Scan pattern of the "drift circle" mode, used for the APEX-SZ array for surveys and individual cluster observations. Shown here is a 6′ radius scan pattern used for observations of the Bullet cluster (1E0657-56) in August 2007. The scan pattern is centered on a fixed coordinate in telescope coordinates (azimuth and elevation, left panel), and the source is allowed to drift through the pattern in the equatorial system; this is shown as the solid line in the right panel. The "footprint" of APEX-SZ is indicated as points in both panels. On the right, it has been rotated into the equatorial coordinate system using the median rotation angle during the scan, and has been placed in an arbitrary position.

225 GHz and thus need to be re-scaled accordingly). To monitor the stability of opacity corrections at different elevations, secondary calibrator measurements are used. Because skydip measurements tend to underestimate opacities at 345 GHz (Weiss et al. 2008), linear combinations with tau-meter readings are constructed such that there is no elevation bias in the estimates. For the results in this thesis, opacity calibration tables have been kindly provided by Axel Weiss. Applying these tables to the secondary calibrators, a random error of 4% in the ratio of expected to measured flux is found. As should be the by construction, there is no noticeable dependence on elevation in the range 30-80 degrees.

5.3.2 Sensitivity

The general discussion from section 5.2.6 of course also holds for other bolometer arrays. Shown in Figure 5.7 is the computed map rms for LABOCA as a function of integration time. The data, covering the central region of the galaxy cluster 1E0657−56, were taken with the spiral scan pattern described in section 5.3.3, and the time series were high-pass filtered to reject all signals on scales larger than one arcminute, effectively removing the emission from the cluster itself. Two bright sub-millimeter galaxies (D. Johansson, personal communication) were removed from the map by masking before computation of the rms. Because the rms does not drop as expected (i.e. with the inverse square root of the integration time), the data was

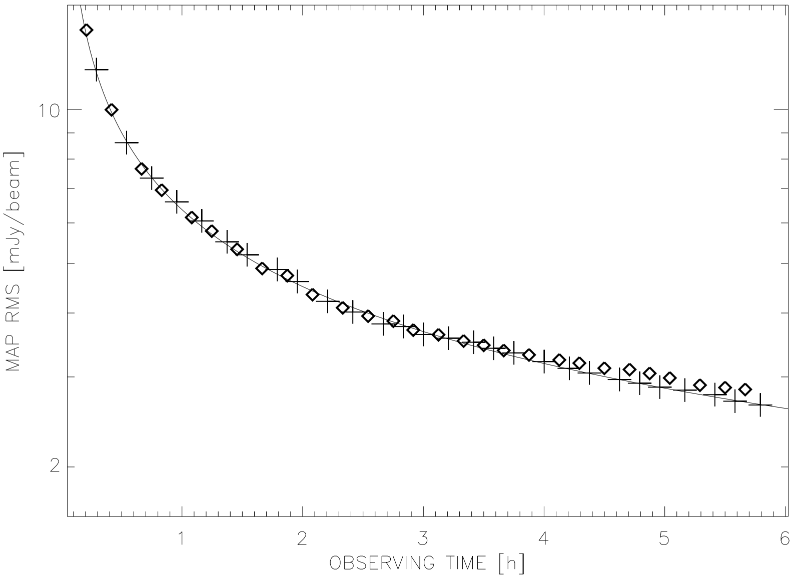

Figure 5.7: LABOCA map rms as a function of integration time (cf. the corresponding plot for APEX-SZ, Figure 5.5). Diamonds show the actual map rms, while plus signs show the rms in maps randomized by inverting half the data to remove any source emission. The rms values have been computed from a heavily filtered data set centered on the Bullet cluster. Effects from emission are evident after four hours of observation (see text). Data courtesy of D. Johansson.

randomized by inverting every other thirty-second interval of the time stream data. Indeed, the rms in the randomized data set drops as expected, indicating that what appears as excess noise in the original data is either directionally dependent residual atmospheric noise or a signal of astronomical origin. Because of the heavy filtering, this is unlikely to be the SZ signal from the cluster (see chapter 6); the most likely explanation is that the sub-mm background (§ 3.2.3) becomes important at a noise level of 2.5 mJy/beam, which is reached after approximately four hours.

5.3.3 Scan Strategies

Like APEX-SZ, LABOCA is under-sampled on the sky. For this reason, even for the detection of point sources the array has to be moved around on the sky in some pattern (unless the source position is known to an accuracy well below the beam FWHM; in such a case one can use an on-on approach with two bolometers alternately covering the source).

By default, small spiral patterns tracking the source are employed. For detection of extended emission, one can either do raster scans or more extended spirals. Figure 5.8 shows an example of the latter.

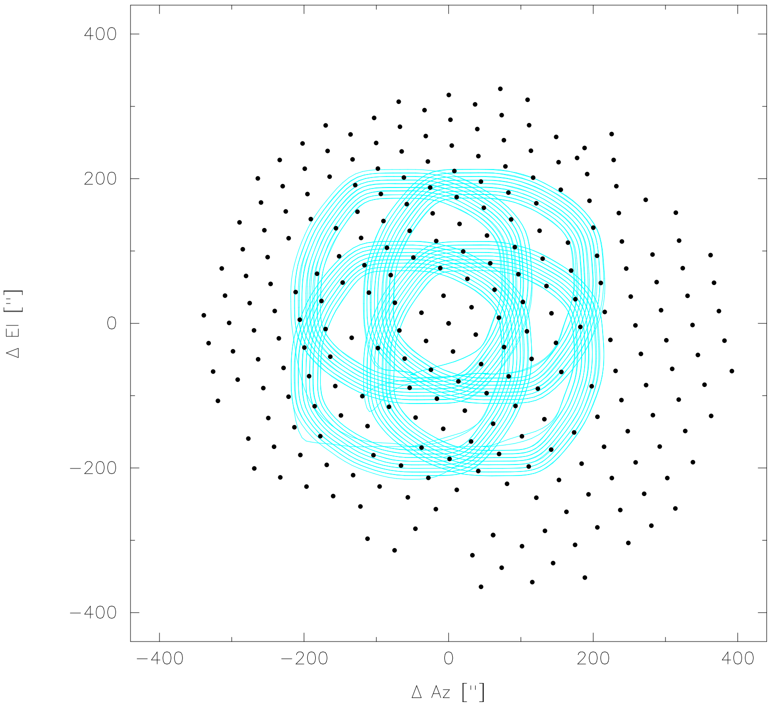

Figure 5.8: Example of a LABOCA scan pattern suitable for recovering extended emission on scales of a few arcminutes. The solid thin lines outline the scan pattern (position of the reference channel in telescope coordinates), and the “footprint” of LABOCA is indicated as points. In contrast to the drift scan mode used for APEX-SZ (Fig. 5.6) The central coordinate of the source is tracked in the equatorial system, so that the scan pattern looks very similar in equatorial coordinates (not shown).

5.4 Conclusion

The two bolometer arrays APEX-SZ, operating at 150 GHz, and LABOCA, operating at 345 GHz, have been introduced. The methods used in extracting array parameters, such as gains and spatial offsets, have been discussed. The details of certain reduction steps associated with this process are discussed in the next chapter.

APEX-SZ time streams are found to exhibit two specific behaviors which limit the performance of the array: glitches and uncorrelated low-frequency noise signals. While the former are relatively easy to remove from data, the latter need to be removed by direct filtering, which also removes some source signal. It is discussed in the following chapter how the source signal can be modeled correctly in spite of such filtering.

LABOCA time streams do not suffer from excessive low frequency noise; however, there are heavy correlations between groups of channels wired together in the readout system. This behavior is relatively easy to deal with; one simply needs to apply correlated noise removal algorithms to these groups of channels separately. This approach is also discussed in the following chapter.

Table 5.1 summarizes the basic parameters of the two bolometer arrays described in this chapter.

Table 5.1: Principal properties of APEX-SZ and LABOCA. The quoted LABOCA values are from Siringo et al. (2007), except where marked with an asterisk (*). The latter values are measured from data used in this thesis, as are all the quotes values for APEX-SZ. Note that several quantities, such as mapping sensitivity and number of channels used for mapping, are highly dependent on reduction (next chapter) and scan strategies. Typical values are given in this table.

	APEX-SZ	LABOCA
Central frequency (GHz)	152 ± 2	345
Bandpass (GHz)	23	60
Beam FWHM (measured)	$58 \pm 1''$	$19.5 \pm 0.6''^{\,*}$
Beam FWHM (theoretical)	$60''$	$18.5''$
FoV (arcminutes across)	23	11.4
Channel spacing (shortest)	$70''$	$36''$
Number of channels (total)	330	320
Number of channels (read out)	232	295
Number of channels (used for mapping)	~ 160	$\sim 230^{\,*}$
Average channel sensitivity, NEP	$10^{-16}\,\mathrm{W\,Hz^{-1}}$	—
Average channel sensitivity, NET	$1150\,\mu\mathrm{K_{(CMB)}}/\sqrt{\mathrm{s}}$	—
Mapping sensitivity (co-added, in one hour)	$75\,\mu\mathrm{K_{(CMB)}}$	6.6 mJy/beam *

Chapter 6

Analysis of APEX-SZ and LABOCA Data

This chapter discusses the general data reduction algorithms used for APEX-SZ and LABOCA data, and the various side-effects that can arise from the individual steps in the data reduction. In particular, it deals with the crucial step of removing correlated signals from an array of bolometers. The reduction algorithms described here apply to weak emission extended on angular scales of a few arcminutes, as expected from clusters of galaxies observed through the SZ effect.

As stated in the introduction, the analysis of data for APEX-SZ is a team effort. Most of the general analysis tools described in this chapter were developed and implemented either within the APEX-SZ collaboration or within the BoA working group in Bonn, and the main task of the author (MN) has been to coordinate and test the pipeline analysis of data. The PCA algorithm for the removal of correlated noise, discussed in § 6.2.1, is well known and documented. Its implementation in BoA has been carried out by MN. The glitch removal algorithms discussed in § 6.3 have been developed and implemented by MN, except the one based on wavelet decomposition.

Sections 6.4 and 6.5 describe the so-called transfer function, which models the attenuation of source signals in map space due to the removal of correlated noise. Filter functions of this type are widely known, and proper credit to previous work is given in these sections. The specific transfer function analysis described in this thesis has been developed by MN in close collaboration with Amy N. Bender and Nils Halverson, and implemented in the analysis pipeline also by MN (the tool is currently not an integral part of BoA).

The discussion of iterative mapping algorithms (§ 6.6.3) is based on the work of Enoch et al. (2006). Substantial modifications to the algorithms of the latter paper have been developed by MN in collaboration with Amy N. Bender and Nils Halverson, inspired by ideas from Florian Pacaud and Axel Weiss. The map deconvolution algorithm discussed in § 6.6.4 has been developed by MN.

6.1 General Considerations

Bolometer time stream signals are typically sampled at frequencies in the range of 50-500 Hz, depending on the backend readout system and the speed of the control software subsystem responsible for writing the raw data to disk. For an array of hundreds of bolometers, this implies a data rate of several thousand samples per second. In spite of such a large amount of raw data, most of the reduction takes place in the time series domain of the original signal. When the data is mapped, it is downgraded in the sense that many time samples are averaged onto a single spatial (map) pixel, effectively causing some loss of information. The removal of atmospheric noise, typically the main source of noise in bolometer observations, relies on the fact that the atmospheric signal is correlated in time between the bolometers. The time stream can also be filtered to reject unwanted spatial or temporal scales.

6.1.1 Recovering Emission on Different Spatial Scales

Data can either be taken "on the fly" (scanning with a continuous pattern) or by switching between positions on the sky using a wobbler ("double beam" data). The obvious advantage of the second method is that it comes with a straightforward way of baselining the time stream data and thus avoiding large contributions from the atmosphere (assuming a fast enough wobbler switch cycle). However, at best half the observing time can be spent on source, unless the emission is point-like and an "on-on" observing strategy can be devised.

LABOCA and APEX-SZ both operate mainly on the fly, as discussed in chapter 5. Thus, sky noise subtraction largely relies on the assumption that there is little variation in the atmospheric emission across the array, or across a fraction of the array that is significantly larger than the typical size scale of the observed source.

To recover the extended emission from astrophysical objects in bolometer observations, there are several spatial scales to consider. These in turn translate to relevant temporal scales through the scan speed across the source. For recovering extended emission while observing on the fly, the important spatial scales (excluding the typical scale of the emitting region itself) are:

1. *The size of the array.* In case the angular extent of the emitting region is comparable to (or larger than) the array size, any correlated noise removal algorithm will remove flux from the source in addition to removing atmospheric noise, unless the source is masked in the time series.

2. *The separation between channels.* Apart from constraining how the scan pattern must be chosen to get a fully and evenly sampled map, the separations between nearest-neighbor channels become important where the emitting region is significantly smaller than the array, but larger then the minimum channel separation. The only case where all the emission can be *completely* recovered (with respect to sky noise removal) is for a source for which the extension is smaller than the separation between channels.

3. *The size of the scan pattern.* Since for each channel one must define a zero signal level, the scan pattern acts effectively as a spatial filter, removing scales larger than the pattern. In general, the only robust way to fix the zero level of a channel is to use the signal of that channel, which means it has to be pointed at an emission-free region ("blank sky") a significant fraction of the time. If the expected region of emission is not well known (making temporary flagging of signals from this region difficult or impossible for the purpose of baselining) an iterative approach must be taken.

Note that the beam size is not of any concern here, as it limits "only" what can be resolved and not what emission is filtered out on large scales.

6.1.2 BoA - The Bolometer Array Reduction Software

The Bolometer array reduction package BoA[1] has been developed (and continues being developed) at the AIfA and MPIfR in Bonn. It is an open-source software implemented in the object-oriented programming language Python. The environment of BoA is basically the same as that of Python, with some added functionality for bolometer array data reduction. This makes scripting very intuitive, and allows for very flexible data reduction also in non-standard cases.

BoA reads so-called Multi-Beam FITS raw data files (MBFits, Muders et al. 2005) and mirrors the contents in a single object, by default called 'data' and henceforth referred to simply as the 'data object'. The data object has several subclass objects. The most important are the 'ScanParam' object, including parameters associated with the time stream, and the 'BolometerArray' object, including parameters associated with the array of channels. After reduction of the time streams is finished, a 'Map' object (also a subclass object of the data object) can be filled by calling a mapping method. This object contains all information on the created map and its projection, and also has several methods for map processing associated with it.

During a typical reduction, the data arrays are modified to remove correlated noise and filter out unwanted frequency components. Flags mark data samples which should not be used to produce the final map, and are handled by three separate subclasses, belonging to the data object (all flags), the ScanParam object (common time stream flags, for all channels simultaneously) and the BolometerArray object (channel flags).

BoA includes a set of well-defined methods applicable for all bolometer arrays. These will be discussed below and include despiking, deglitching, filtering in the frequency domain, baselining of individual channels and map making, as well as several algorithms for correlated noise removal.

The discussion in the rest of this chapter will be kept as software-independent as possible. There will, however, be frequent references to BoA for practical reasons. APEX-SZ and LABOCA will be treated in parallel where it is necessary to distinguish between reduction steps specific to either of the two arrays.

6.1.3 General Reduction Steps

Although the reduction of each data set has to be adapted to the specific circumstances − such as the spatial scale of the emission, the scan strategy used and the weather at the time of observation − a general reduction pattern applicable for almost every data set can be outlined. A typical reduction consists of the following steps:

1. *Removal of dead channels*: A so-called rcp file, containing information on bolometer offsets and gains (chapter 5), is read. This file also contains information on the noise properties of the individual channels, which can be used for excluding noisy channels at the beginning of the reduction.

2. *Flat-fielding and calibration*: The time signals of all channels are multiplied by their respective gains, after which an overall calibration factor is applied. The calibration factor is corrected for the difference in opacities at the calibrator and target elevations.

3. *Subscan subdivision*: The time sequence is divided into segments (subscans) depending on the scan pattern: circular patterns are typically divided into full circles (or multiples

---

[1] `http://www.apex-telescope.org/bolometer/laboca/boa/`

thereof), raster patterns are divided into single sweeps in one direction of azimuth, and spiral patterns are divided into full spirals.

4. *Correlated noise removal*: This step removes noise that is correlated in time and originates from the atmosphere, the antenna and the instrument. Algorithms for this step are discussed in section 6.2. Typically, the correlated noise is removed in several steps, flagging noisy channels (that were previously not recognized as such) in between.

5. *Deglitching*: Mostly used for APEX-SZ, this step removes glitches (§ 5.2.5) from the time stream, flagging intervals of time for all bolometer channels.

6. *Despiking*: Signals exceeding a threshold proportinal to the noise rms in each channel are flagged. This steps sets individual sample flags only.

7. *Fourier filtering of the time signal*: Based on the scan pattern, the scan speed and the angular scale of the source, a cutoff frequency for a high-pass filter can be determined. Frequencies below the cutoff can then be suppressed using a Butterworth filter in frequency space, making use of the fast Fourier transform (FFT). Alternatively, a polynomial can be fitted to the signal of each channel, either by subscan or to the entire time series of a channel.

8. *Baselining*: Here a median, mean or polynomial baseline is applied to the time stream of each channel, again either to the entire time stream in a scan or to each subscan.

9. *Flagging by acceleration and speed of the scan pattern*: At large scan speeds and accelerations, it is not guaranteed that the commanded telescope coordinates agree well with the actual pointing of the telescope. For this reason, it is necessary to flag such time intervals. These include times of turnarounds in raster patterns, and beginnings and ends of circular and spiral patterns.

After the time series reduction is complete, all non-flagged samples are combined into a map. To this end, every time stream sample is assigned a weight that is proportional to the inverse square of the noise rms. Noise rms values can be determined either for whole scans or for subscans, but always separately for each channel. The weights are then used to add each sample into the map (natural weighting). Parallel to building a map from the data, a total weight map is constructed. The latter can be used to co-add maps from different scans.

Maps can be projected in several ways. BoA produces maps in the equatorial system in the GLS projection (Calabretta & Griesen 2002), and horizontal maps in offsets of the telescope system (azimuth and elevation offsets).

6.2 Algorithms for Removal of Correlated Noise

The signal of a single bolometer has many components, some of which are correlated between different channels. In the absence of astronomical signals and disregarding AC offsets and baseline drifts of individual channels, the signal $S_m(t)$ of a channel m can be written as

$$S_m = c_m^{\mathrm{sky}} s_m^{\mathrm{sky}} + c_m^{\mathrm{det}} s_m^{\mathrm{det}}, \tag{6.1}$$

where s_m^{sky} is the sky signal and c_m^{sky} is the dimensionless response to this signal. For simplicity, it is assumed that all correlated noise comes from the atmosphere, and all uncorrelated noise is included in s_m^{det}.

Although the sky signal is expected to be correlated across the array, the factor c_m^{sky} can vary from channel to channel; the sky signal is often orders of magnitude larger than the astrophysical signal, and there may be a nonlinear coupling of the sky signal to the detectors. Furthermore, there can be variations in sky brightness across the array. For this reason, it is typically necessary to flat-field the channels (applying a temporary gain correction based on the low frequency parts of the signals) before correlating them to remove the atmospheric signal.

In this section, two separate algorithms for the removal of correlated noise are described.

6.2.1 Principal Component Analysis

Principal component analysis (PCA) is a mathematical method of linear transformation by which data is transformed into a new coordinate system such that the greatest variance by any projection of the data comes to lie on the first coordinate (called the first principal component), the second greatest variance on the second coordinate, and so on.

As a simple example, for a set of n data points in two-dimensional space the first direction (the first *principal component*) in the transformed coordinate system is the best-fit (in least square terms) straight line through the data set. The second (and, in this case, last) direction is orthogonal to the first. The two components correspond to the eigenvectors of the covariance matrix for the n points.

The method can be used for dimensionality reduction in a data set by removing certain characteristics of the data, corresponding to certain eigenvalues and eigenvectors of the covariance matrix. In the above example, removing the second principal component would force all points to lie on a straight line when transforming back to the original coordinate system.

For the purpose of reducing bolometer array data, PCA can be used to remove the principal components corresponding to the *largest* eigenvalues of the covariance matrix; these components are the ones most correlated across the array and most likely to contain atmospheric signal.

The algorithm for using PCA on bolometer array data is straightforward. Let $D = \{D[m,n]\}$ be the data, where m and n denote the channel and time stamp indices, respectively. This is then an $M \times N$ matrix, with M the number of channels and N the number of timestamps considered. In practice, D is compressed in both dimensions to contain only non-flagged channels and non-flagged time stamps. Individual sample flags cannot be taken into account as this would make the computation of the covariance matrix undefined. The raw data matrix is adjusted so that the mean of each channel is zero. The correlation matrix is defined as

$$C = \{C[p,q]\} = D \times D^T, \tag{6.2}$$

and has the dimension $M \times M$. Now let $V = \{V[p,q]\}$, with p and q ranging from 1 to M, denote the matrix of all eigenvectors of C, sorted such that there is one eigenvector per column. This is the matrix that diagonalizes C,

$$V^{-1}CV = E, \tag{6.3}$$

where E is a diagonal matrix with the eigenvalues of C on the principal diagonal and zero elsewhere. Since it is not necessarily the case that the first eigenvector of V corresponds to the largest eigenvalue, C must be sorted in order of decreasing eigenvalues.

At this point, the eigenvectors that are to be retained in the new basis must be selected. Since the atmospheric signal is not identical across the array and because noise components with varying degrees of correlation are present, this is not an easy task. One can either use a pre-selected number that one might guess from the number of channels (equal to the number of principal components in the data) in the analysis, or one can attempt to infer a number of components to remove based on the distribution of eigenvalues.

By removing the q principal components with the largest eigenvalues, V is reduced to W (which has $M - q$ columns), and the entity

$$F = W^T \times D \tag{6.4}$$

is constructed. Note that W has the dimension $M \times M - q$, so F will have the dimension $M - q \times N$. Finally, to go back to the original basis, the inverse transformation

$$D_1 = W^T \times F \tag{6.5}$$

is carried out, yielding the dimension $M \times N$ for the reduced data matrix D_1, as expected. D_1 is the final result, where components of the signal corresponding to the largest correlations in the data matrix have been removed.

6.2.2 Median Noise Removal

Median noise removal (henceforth MNR) is an intuitively more direct method than PCA for removing correlated noise. It is based upon the simple assumption that the correlated noise component is the same for every channel, save for arbitrary differences in the normalization.

The method requires a separate normalization step, amounting to a (temporary) gain correction of the signal of each channel. The gain factors are determined from the signals themselves as the median ratio between each channel and some specific reference channel. The reference channel can also be chosen as the mean or median of all channels used. These gains are assumed to be specific to the correlated noise and are removed from the data after the reduction step, as the relative channel *calibrations* are determined from scans of bright point sources and not from the science scans themselves. It is quite feasible that correlated noise gains can be different from calibration gains if the bolometers are not quite linear in their response. This is particularly likely to be the case when comparing signals across a large dynamical range; note that in the individual channel time streams, the amplitude of the signal from a cluster of galaxies is several orders of magnitude smaller than variations due to atmospheric noise.

After gain correction, the median of each time stamp across all (non-flagged) channels is removed. Note that, unlike to PCA, MNR can accomodate individual sample flags, as long as for each time stamp there are enough useful samples left so that the median can be computed reliably. This allows a temporary flagging of source regions prior to the correlated noise removal step.

6.3 Glitch Removal

Apart from removing correlated noise and filtering out unwanted low frequencies from the time signal, the removal of glitches (§ 5.2.5) is an important step in the time series reduction of data from APEX-SZ. Since glitches occur near-simultaneously in several channels at once, algorithms for their removal rely on correlating channels taking into account that there can be small delays and that correlations do not have to be positive. This is what makes glitches essentially different from spikes, which are found and flagged individually.

BoA currently has three algorithms implemented for glitch removal:

1. *Glitch removal by sliding rms*

   This algorithm is based on the assumption that glitches cause abrupt changes in the rms, computed on a sufficiently short time scale, of individual channels. The rms is computed for each channel in a sliding window which needs to be larger than the typical delay of glitches between channels, but small enough for the glitches to stand out. Empirically, one finds that time scales in the range 0.1-1 seconds are appropriate for most data.

   This procedure yields a matrix of sliding rms values for each channel, which has the same dimension as the data matrix. The rms values are then collapsed into one array with the dimension of the total number of time stamps, by taking the median value of all (non-flagged) samples at each time. The resulting array will be reasonably uniform if no glitches are present, and will have sharp peaks where glitches occur. An iterative sigma-clipping applied to the array now identifies which time stamps are to be flagged.

2. *Glitch removal by standard deviation*

   The second algorithm is very similar to the first one, but rather than computing the rms values in short intervals of time, the algorithm compares time stamps by computing the standard deviation of samples at each time. Because one empirically finds that the *amplitude* of glitches does not scale with the channel response, the channel signals are weighted by their respective channel rms values (computed for the whole time stream).

   Once the array of standard deviations has been formed, a pre-defined threshold is applied to decide what time stamps (if any) are to be flagged.

   This method does not by default account for small delays between the glitches occurring in different channels. To deal with this, the array of standard deviations can be smoothed with a kernel, whose width is determined by the typical delays (see above).

3. *Glitch removal by wavelet decomposition*

   The third way of removing glitches is based on a wavelet filter developed by F. Pacaud. The basis is multi-resolution analysis, decomposing the signal of a single channel into contributions at different scales. To achieve the latter, a discretized wavelet transform is used. Wavelet transforms are suitable for detecting sharp edges at all scales, thus effectively identifying glitchy boundaries between “well-behaved” regions.

   As this type of analysis identifies candidate glitches in individual channels, it is necessary to collapse the resulting array of flags. This is done by counting the number of glitches found at each time (or within a small time interval) and comparing this to the total number of yet non-flagged samples at the corresponding time. If the ratio of these numbers is greater than a fixed fraction (0.3 has been found empirically to work well), all samples in the given time interval are flagged.

Algorithms 1 and 2 can be said to be “quick-and-dirty” (yet very efficient) methods of finding regions in time where the properties of the data differ from the rest of the scan. Although one of them uses rms in time and the other uses standard deviation at fixed times, their performance can be brought to be nearly identical if the parameters of the processes are suitably chosen. A basic problem with these methods is that they are hardly sensitive enough to be used before sky noise reduction, at a point when the atmospheric signal often dominates completely. It is possible that the correlated noise removal process can be corrupted by not yet flagged glitches, thus introducing artifacts into the data. This makes it necessary, in extreme cases, to perform the removal of correlated noise twice: once to make deglitching possible, and once after deglitching, with the data matrix reset to its original state (but with glitch flags implemented). In very few cases, the correlated noise removal process is so corrupted that deglitching with a quick-and-dirty method is made impossible. However, it is questionable whether the latter category of data is at all useful for astronomical purposes.

The advantage of the multi-resolution wavelet analysis is that it can reliably identify glitches also *before* the correlated noise removal is carried out. At present, however, the multi-resolution analysis implemented in BoA is too slow to be of much use in pipeline data reduction. For this reason, method 2 is currently the default for reduction of APEX-SZ data.

6.4 Modeling the Transfer Function of the Reduction Pipeline

As already mentioned, the choice of scanning strategy and method for the removal of correlated and low-frequency uncorrelated noise can seriously affect the source signal in the reduced data. This is often loosely referred to as “flux loss”.

A simple way to deal with flux loss is to apply an iterative mapping algorithm, such as that described in § 6.6.3. However, such approaches can be extremely slow to converge, especially in cases where the extent of the source is comparable to the size of the scan pattern. An alternative that requires much less computing power is to model the effect of the reduction pipeline on the sky signal with a filter acting in map space. The problem is thus shifted to finding this so-called transfer function (Benson et al. 2003, Reese et al. 2000) for the particular sky distribution observed. This turns out to be very difficult in the general case, but with a few constraints on the reduction algorithm, the problem can be solved by passing a beam shaped function through the same reduction as the actual data. This way not only the reduction pipeline, but also the intrinsic beam dilution from the instrument, is included in the total transfer function.

In cases of significant detections, the reduced map can be de-convolved directly using the transfer function of the pipeline. Since this requires that the noise characteristics of the reduced map are well understood, it has so far been successfully used only on a limited sample of high significance detections from APEX-SZ (see chapters 7 and 9). Where the map properties are less favorable to deconvolution, any model can be fitted to the sky distribution in a straightforward way by convolving the model with the transfer function.

Let k denote the source distribution on the sky. The data d, projected onto map space, is then the sum of k, the correlated noise component c, and an uncorrelated noise component n, all projected onto map space:

$$d = k + c + n. \tag{6.6}$$

Furthermore, let p denote the filter function of the *time stream* reduction of the data d (but still evaluated in map space), such that the reduced data r is the convolution of d with p. In Fourier space,

$$R = PD, \tag{6.7}$$

where upper case letters denote the Fourier transforms of the respective quantities written in lower case.

The goal is to recover the source flux distribution k from the reduced map r. The first step is thus to find the filter function p. The latter can be estimated to first order by by studying what the pipeline does to a *known* source distribution, b, typically a normalized beam map.

From b a time stream is constructed (in BoA this is done with the syntax `addSource`) on which to apply the reduction pipeline. The reduced map, m, of the known source is represented in Fourier space as

$$M = P'B. \tag{6.8}$$

Note that the filter p' representing the pipeline in this case is *not* necessarily identical to p, since the noise properties of b and d are likely to be very different. In particular, if b is chosen as a beam map, it has no noise at all. Although p' does not represent the sought transfer function, since p has also filtered out *atmospheric* correlated signals, it will be argued in the next section that p' can be brought to represent the transfer function. In this case, it is assumed that p has removed all atmospheric noise from d and left all components of the uncorrelated noise unchanged. It is also assumed that p has the same effect on the signal part of the data (in addition to removing correlated noise) that p' has on the model. Then,

$$(K + N) = R\frac{B}{M}, \tag{6.9}$$

where the only unknown (apart from the noise) is the true flux distribution K. The division corresponds to deconvolution in map space, which in general is a very sensitive process. In particular, it is usually not safe to perform a deconvolution by dividing in Fourier space in the presence of noise, since small errors will tend to magnify.

Here one has the advantage of being able to choose B (by choosing b) and thus indirectly choosing M as well. The deconvolution can thus be kept reasonably controlled by not injecting any noise into B (the same assumption as in Eqn. 6.9). Although it is not self-evident that the latter provides a valid estimate of the filter function p, it will be demonstrated in the following that this is indeed an effective and valid approach under a specific set of circumstances.

How the deconvolution can be done in practice is discussed in § 6.6.4.

6.5 The Point Source Transfer Function

In the general case, it must be assumed that the effect of the data reduction pipeline on the apparent flux distribution depends on that distribution; in the notation of the previous section, $p \neq p'$. Where the source flux distribution can be matched with a simple model, the general problem can be solved by using an iterative approach: the model source b is chosen as the result of a first reduction, and the resulting transfer function is used to fit a new model. This model is again passed through the pipeline to yield a new transfer function, and so on. However, this approach is of limited use for several reasons. First, few sources other than point sources are accurately described by simple models; second, the approach is time consuming because it is iterative; and third, it is not guaranteed *a priori* that a model source without added noise will sufficiently describe the filter function of the reduction of the astronomical data.

Surprisingly, a transfer function constructed from a point source (Halverson et al. 2008, Scott et al. 2008) can be brought to describe the filter function of a reduction pipeline remarkably well, which is shown empirically in this section.

6.5.1 Definition and Construction

To model the entire transfer function from the astronomical signal distribution to the reduced map, a beam shaped source, i.e. the image of a bright point source produced by the instrument, is used as the model to be passed through the pipeline. For this, simulated time streams t_t

(without noise) are constructed such that projecting these onto a map would yield the beam shaped source. Because of the difference bewteen this data set and the actual data, the reductions cannot be parallelized. In particular, reduction steps such as flagging by channel noise and flagging spikes are meaningless for a noise free data set. Thus, such flagging steps are carried out on the actual data, after which the flags are copied to the model data. Weights (§ 6.1.3) are also copied directly from the data to the model.

Mapping the model data after reduction yields the point source transfer function. Assuming that the reduction script has affected the data and the model in the same way and that the input model beam is accurate, the reduced map is now the convolution of the true signal distribution with the transfer function (in addition to noise). Any reduction scheme preserving these properties will be referred to as being *linear*. Next, the conditions for a reduction to be linear are discussed, first in the absence of noise, then for noisy data.

6.5.2 Testing on Noise Free Simulations

To test how different reduction steps affect the transfer function in relation to actual source distributions, the reduction steps are applied to a range of simulated sources to investigate how well the transfer function convolved input signal corresponds to the "reduced" simulation. Several types of source models have been tested, including β models, Gaussians, and more complicated structures such as double β models with centroid offsets. The models have been added to the time streams of several types of data, such as raster scans, circular drift scans and scans describing spiral patters.

The general conclusions on which reduction steps preserve linearity are valid for all source models and scan types tested; thus only a few examples are presented here. Figure 6.1 shows the effects of several reduction steps on a β model (chapter 2) using actual drift circle data to create the noise free time streams. The input model (with $\beta = 0.8$, $r_c = 36''$) was convolved with the beam (§ 5.2) to simulate the (noise free) observation prior to carrying out the respective reduction step. A separate transfer function was constructed for each step.

Although not quantitative, Figure 6.1 illustrates clearly what reduction steps are linear. In particular, median noise removal is preferred to PCA for the removal of correlated signals. Polynomial baselines produce no apparent deviations from linearity, regardless of whether baselines are removed from circular subscans or from the entire scan. Median baselines, as expected, affect extended sources more severely than small ones, and the transfer function fails to account for this. Note that a polynomial baseline of order zero is equivalent to removing the *mean*, not the median, of a time stream; this step is indeed linear.

6.5.3 Testing on Noisy Simulations

Thus far, atmospheric and detector noise have been ignored. The effects of noise can be studied by adding artificial sources to actual data, which has been "bootstrapped", i.e. inverting the sign of every other minute of the time stream data in order to remove any astronomical signal, and extracting the sources after reduction using the point source transfer function. To simulate sources, once again the isothermal beta profile is used; it has a simple form and gives a reasonable fit to most cluster detections, thus making it appropriate for the results presented in the following chapters.

Two observations have been used here: six hours of APEX-SZ raster scans of the galaxy cluster Abell 2163 and seven hours of APEX-SZ drift circles of the Bullet cluster (1E0657−56). The two data sets are treated separately to test the effects of the data reduction on the different scan types. Different β models are added to the data, and each set is reduced 100

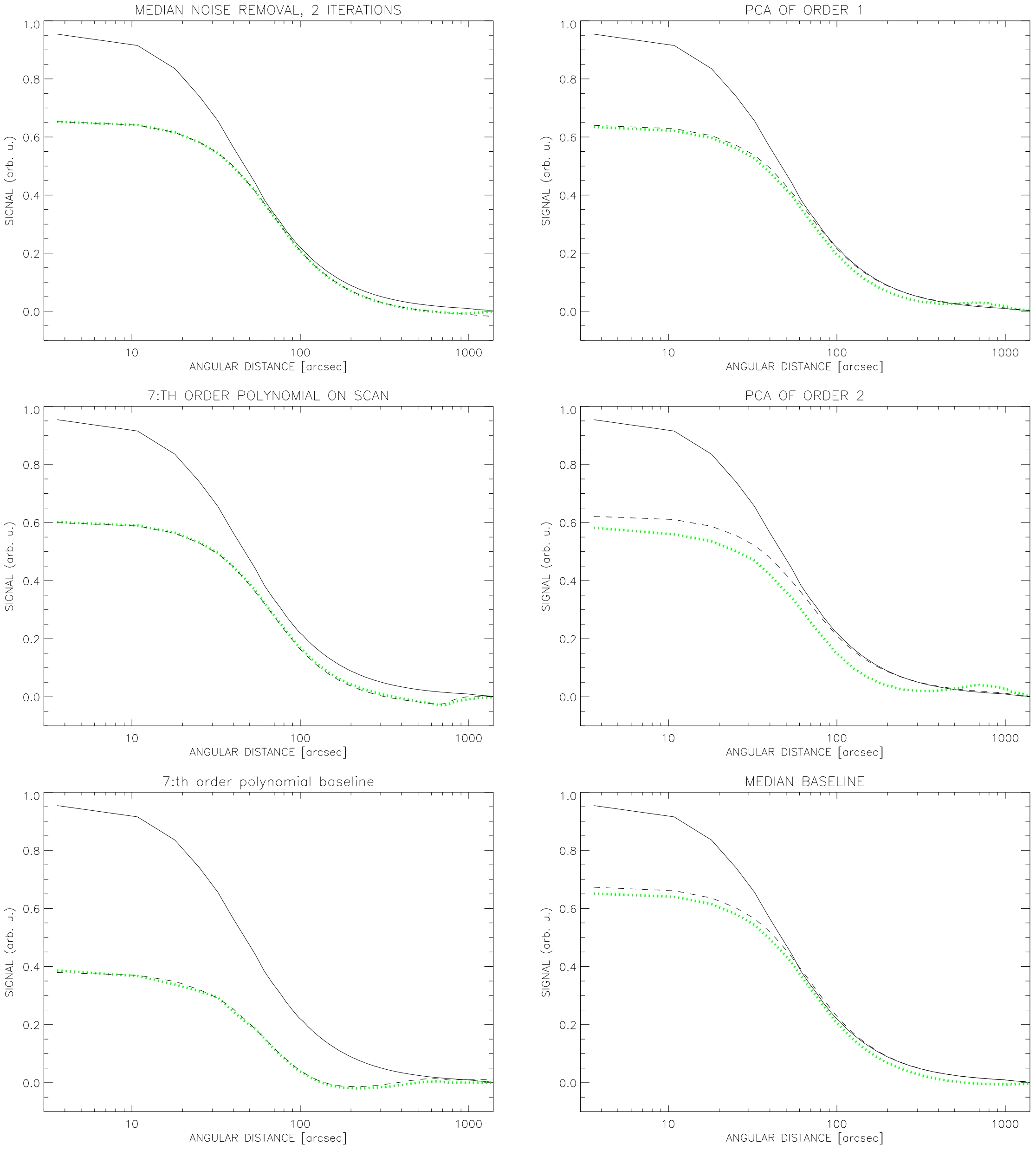

Figure 6.1: Effects of various reduction steps on a beta model with $\beta = 0.8$ and $r_c = 36''$, compared to the input model convolved with the transfer function. Solid lines indicate the radial profile of the input model (same in all panels). Each dotted line indicates the radial profile after the respective reduction step, and the dashed lines indicate the predictions from the respective transfer functions.

times for ten different values of β and r_c, respectively; β varies between 0.5 and 1.55 while r_c varies between $50''$ and $230''$. The entire procedure is repeated three times for different peak temperature values: 1, 4 and 10 $\mathrm{mK_{CMB}}$ (where the subscript CMB indicates thermodynamic temperature). The low value is approximately consistent with the SZ decrements from Abell 2163 and 1E0657−56 (see chapter 7). However, such low peak values imply noisy maps, resulting in large errors on the extracted parameters and making it difficult to draw conclusions. Higher values than 10 mK are impractical because reduction steps such as despiking and deglitching will affect the signal.

To account for instrument resolution, each β model is convolved with the APEX-SZ beam (chapter 5) prior to being added into the data. The reductions applied to the drift circle scans and raster scans are identical to those described in chapter 7. To account for small variations in the transfer function with different data sets, a beam-shaped source is reduced along with each reduction.

After reduction, a co-added map (§ 6.6.1) is produced for each simulated profile, and the respective transfer function is used to convolve the fitting function (β model) while fitting for the model parameters. Because of some degeneracy between β and r_c, each model fit is carried out twice, keeping one of these parameters fixed while allowing the other and the peak amplitude T_0 to assume their best fit values. By comparing to a set of fits where both parameters are allowed to vary freely, it is confirmed that the results are essentially consistent with the exception of an expected large difference in the overall *scatter* of all parameters.

Figure 6.2 shows the ratio of fitted to input parameters for the simulation with $T_0 = 10$ $\mathrm{mK_{CMB}}$ using raster scans. The corresponding results for circular drift scans are given in Figure 6.3. The simulations with lower input T_0 yield similar results, but the scatter in the fitted parameters is much larger, making it difficult to quantify the errors directly as a function of the input parameters. Therefore, a third order polynomial surface is fitted to each set of ratios of fitted to input parameters in $\beta - r_c$ space. The results of this are consistent with those of the $T_0 = 10$ $\mathrm{mK_{CMB}}$ simulation run, in the sense that the fitted surfaces can be brought to agree with the results shown in Figs. 6.2 and 6.3 by varying the parameters of the polynomial surfaces within their uncertainties. In the range 1-10 $\mathrm{mK_{CMB}}$, there is thus no indication of a dependence of the fitted parameters on signal amplitude.

Within the range of β and r_c used in this simulation, the systematic errors on beta models introduced by the reduction are small. The largest errors are found for large core radii combined with small values of β. This is not surprising, since a decreasing β broadens the profile. For typical cluster parameters such as those derived in chapter 7 and in recent X-ray analyses (e.g. LaRoque et al. 2006), the error is consistently less than 20% on β and r_c, and less than 5% on T_0. Note that the latter is comparable to the uncertainty in the absolute calibration of APEX-SZ data (§ 5.2.3).

The central amplitude loss (before transfer function correction) can be as large as 50% for typical values of r_c and β. This is indicated in Figure 6.4, which shows the radial profile of an artificial beta model before and after pipeline reduction. For comparison, the results from the North American MATLAB APEX-SZ pipeline (applied to the same data) are also shown (data reduced by A. Bender). The drift scan data from the Bullet cluster field (see above) was used to generate a realistic noise component. The two reduction pipelines carry out the reduction steps in different order and largely use different algorithms (e.g., for deglitching and high-pass filtering). It is thus not surprising that the uncorrected radial profiles are very different. In spite of this, each transfer function correctly predicts the output map from the input model within statistical uncertainties.

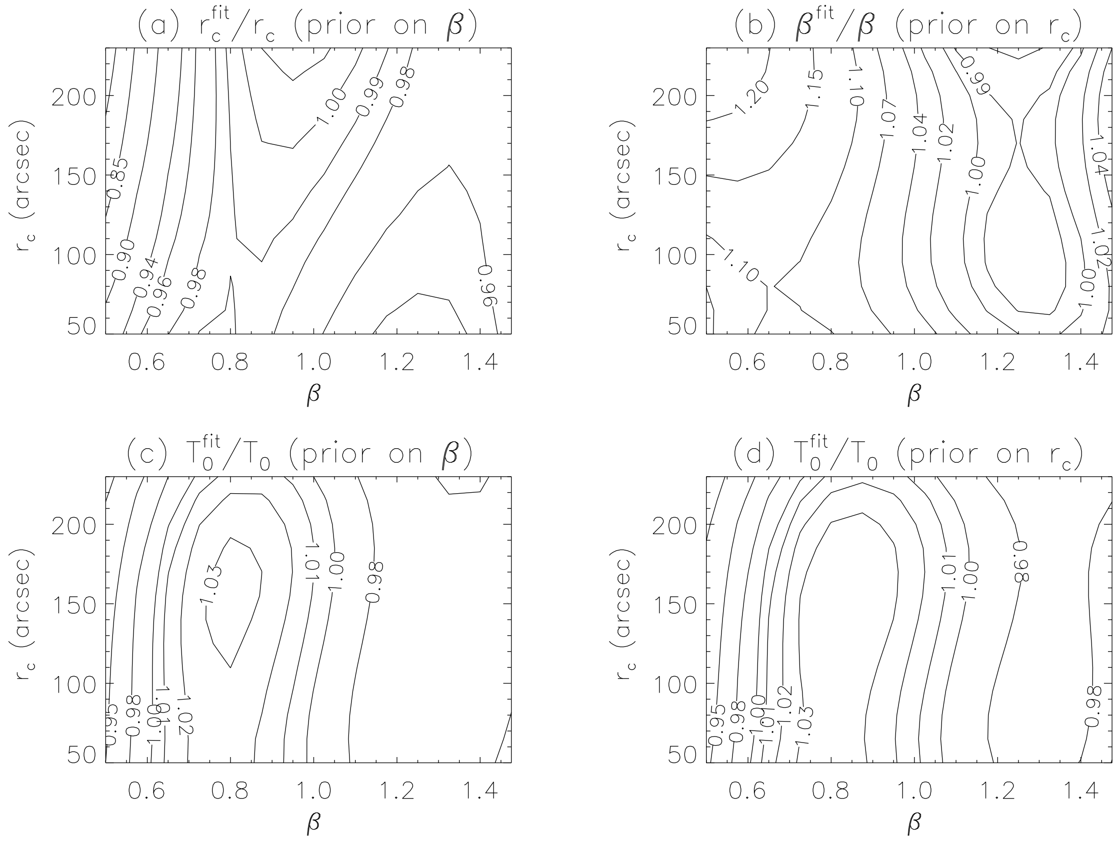

Figure 6.2: Ratios of fitted to input parameters after standard pipeline reduction of a range of beta models added to "bootstrapped" raster scan data. Due to the large degeneracy between the parameters β and r_c, each was fitted with the other one kept fixed. The left-hand panels thus show ratios of parameters fitted while keeping β fixed, while the right-hand panels show ratios of parameters fitted while keeping r_c fixed.

6.6 Map Making

6.6.1 Co-adding of Maps

Maps are made in BoA by co-adding the individual time signals of all non-flagged bolometers using weights associated with each sample. Thus each map pixel has a weight associated with it, and these "pixel weights" are used for co-adding maps from different scans. This is more straightforward than recomputing weights from the noise distribution in the map, since the latter is complicated by the possible presence of bright sources and the typically uneven coverage in a map of a single scan. In some cases, however, it can be necessary to recompute map weights; in particular if the time signals contain low-frequency components at frequencies similar to those characterizing the scan pattern. The latter would be the case, for example, if there remained some atmospheric signal related to the scan pattern through differences in elevation.

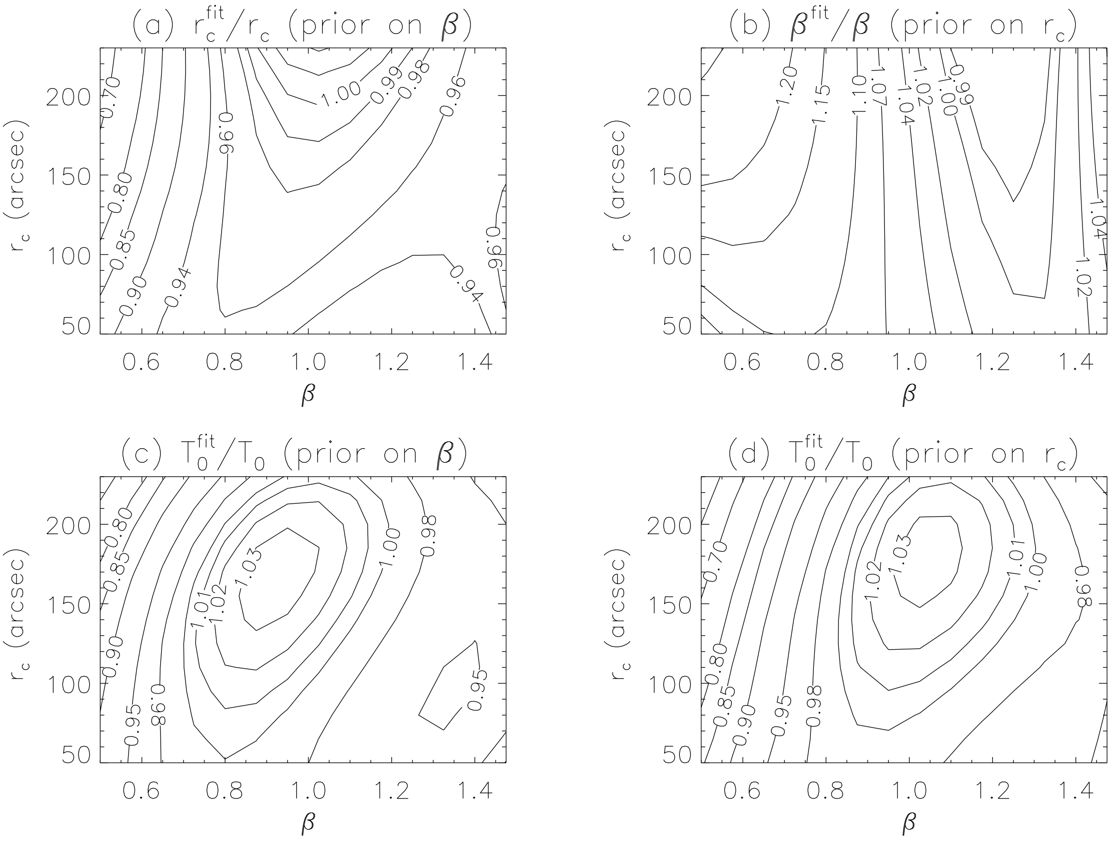

Figure 6.3: Same as Fig. 6.2, but for circular drift scans.

By default, weights scale as the inverse square of the channel rms value (the root mean square of each channel time stream). For LABOCA and APEX-SZ, it has been found that the total map rms does not improve by using local rms values (such as the rms of a subscan in a given channel) because the noise properties of individual bolometers vary slowly in time.

Weighting by channel rms is equivalent to weighting by the total noise power of each bolometer. This is optimal if the *shapes* of the power spectra of the individual channels are similar. While the latter is typically true within scans, in the reduction of large data sets taken over several hours, days or even months (chapter 7), the general behavior of the power spectra can change significantly. For this reason, it can be useful to compute weights based on the integrated power in a selected frequency band responsible for spatial fluctuations of the angular scale that one is interested in.

6.6.2 Map Smoothing

To avoid downgrading the resolution of the data, maps need to be oversampled with respect to the beam size. Typically, a maximum pixel size of one third of the beam full-width half-maximum (FWHM) is advisable in order to preserve the resolution (spatial information), while pixel sizes smaller than one sixth of a beam often result in unevenly sampled maps. To reduce

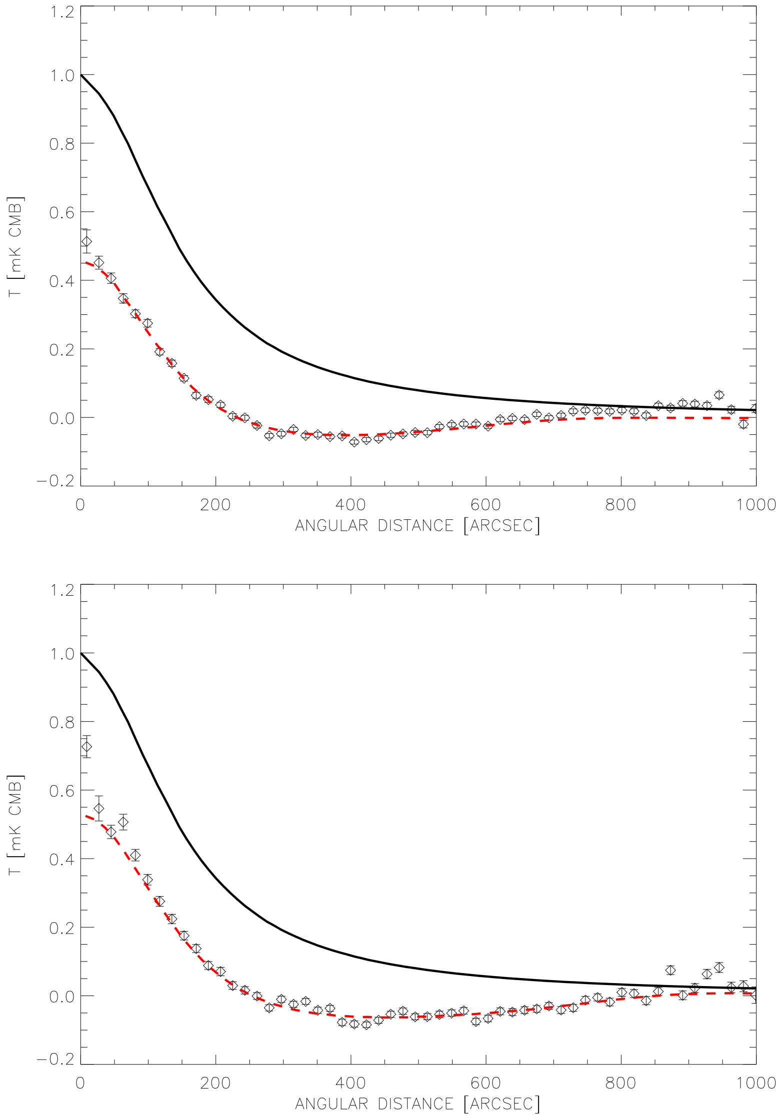

Figure 6.4: Results of the pipeline reduction of a broad beta model with r_c=140″ and $\beta = 1$ produced by BoA (*top*) and the North American MATLAB pipeline (*bottom*). Solid lines indicate the input profile, dotted lines the input profile convolved with the respective transfer function and error bars the actual profiles in the reduced maps.

the sample variance on the beam scale and obtain maps with high signal-to-noise ratios (as well as maps which are easy to view), a typical step before displaying a map is smoothing it with a kernel similar to the instrument beam. In cases where the emission is significantly more extended than the beam size and the sensitivity is poor, it can also be useful to smooth to larger scales to improve the image quality.

Smoothing can be normalized in different ways; usually either to preserve the peak signal of a point source or to preserve its integrated signal. Since this step often causes confusion among reducers of bolometer data, a short discussion may be helpful. For simplicity, it is assumed in what follows that all beams and kernels can be sufficiently described by Gaussians.

In a raw map, the resolution is limited by the instrument beam and the pixel size. It is assumed, however, that the pixel size is chosen small enough that it can be neglected. Furthermore, any pointing errors on individual bolometers are disregarded. Then, the raw map will have the same resolution as the instrument. Smoothing with a Gaussian kernel with the same FWHM as the beam will now downgrade the resolution by a factor of $\sqrt{2}$, i.e. the effective resolution will be equivalent to that of an instrument with a beam FWHM $\sqrt{2}$ times greater than that of the actual instrument (where the data came from). Similarly, the effective beam area of this hypothetical instrument will be a factor 2 larger.

The flux density at the peak of a point source (peak flux) is measured in units of power per solid angle, where a natural choice of units for the solid angle is the beam. Of course, the same entity is measurable anywhere in the map, not only at the peak of a point source. The *integrated* flux is the flux per beam integrated over the entire source. For a point source, the peak flux is equal the integrated flux. Note that two instruments with different beams will "see" the same point source with the same peak flux, provided neither resolves the source.

Normalizing the smoothing kernel to *peak* signal means that the kernel has a peak value of one. This will preserve the peak signal value of a point source in the map, but at the same time the FWHM of the point source will increase by a factor of $\sqrt{2}$. Although it seems the *integrated* flux has thus been increased artificially (by a factor of two), the effective beam width has also changed such that the equivalent beam area has become twice as large. Seen in this way, the map is still consistent with the un-smoothed one, but with a larger effective beam.

Conversely, normalizing to integrated signal (with the integrated kernel volume equal to one) will not conserve the peak flux, but will conserve the total signal of the map. The original (instrument) beam thus applies when converting between peak and integrated flux.

In summary, the two normalization conventions are equivalent when considering the correct beam after smoothing. Since normalization by integrated signal preserves the flux in the map, this is the method that should be used when estimating the rms per beam in a map.

6.6.3 Iterative Map making

The term iterative map making is used quite broadly for algorithms combining a reduced map with the data reduction algorithm in an iterative way. The general idea is to first produce a map from a "blind" reduction (knowing little or nothing about the flux distribution of the source) and subtract the resulting signal, extracted from the map in some way, from the time stream data before proceeding with a second reduction. For emission that is very extended with respect to the beam, this can resolve baseline problems and non-linear flux loss introduced by correlated noise removal. Before the second map is made, the subtracted signal is re-introduced into the time stream; this source component is then safe from flux loss due to the reduction. The new map can be used to extract a new template, with subsequent iterations until the measured signal converges.

The basic iterative mapping algorithm used on LABOCA data in chapter 9 is similar to the one described by Enoch et al. (2006). The description given here will follow the conventions used in that paper. Let i refer to the iteration number, such that $i = 0$ indicates the data before any source model has been subtracted, and let j denote the channel numbers. The first step is to reduce the raw time streams $t_{i=0,j}$ and make a first map, $M_{i=0}$. This map will likely contain artifacts such as negative rings around bright sources (from baselining in the presence of strong emission) and will have some flux loss depending on the source morphology. From $M_{i=0}$ a signal-to-noise map $R_{i=0}$ is constructed by dividing by the *local* rms of the map. The signal-to-noise map is used to select regions of the map where the significance is less than a selected number of standard deviations N_σ, usually 3 or 4. These regions of the map are set to zero in $M_{i=0}$, resulting in the template $T_{i=0}$, which is the current best guess of the source flux distribution.

Now, a set of modified time streams $t_{i=1,j}$ is constructed, subtracting the template $T_{i=0}$ by the appropriate transformation from map space to time series space. The modified time streams are put through the reduction and mapping to yield a map $M_{i=1}$, etc. At this point, Enoch et al. take a conservative approach and derive a new template $T'_{i=1}$ directly from $M_{i=1}$. $T'_{i=1}$ is then added to $T_{i=0}$ to yield the new template $T_{i=1}$. This approach will only add signal to $T_{i=1}$ in regions where the significance of the *residual* map (the map with the first template removed from the reduction) is greater than N_σ. In view of the faint, extended emission from galaxy clusters in the SZ effect, a somewhat more pragmatic approach is taken here. A total map $M'_{i=1} = M_{i=1} + M_{i=0}$ is constructed, and the new template $T_{i=1}$ is derived from $M'_{i=1}$. This will ensure that any significant feature in the *current* best guess of the source flux distribution is carried over to the next iteration step. In what follows, this will be referred to as the *standard iterative mapping approach* .

Although the most straightforward approach to computing the noise map would be to directly compute the rms in each pixel of the map with an appropriate window, this is impractical because the source flux distribution will artificially raise the rms and underestimate the signal-to-noise ratio of the source. For this reason, the rms is computed only in areas of the map where there are no known sources. The actual noise distribution map (the one by which to divide the map) is computed as the inverse square root of the weight map (§ 6.6.1). This map is then normalized using the values and positions of the computed rms values. If time signals from different scans have very different power spectra, it may be necessary to confirm that the map weight distribution of scans indeed scales with the map rms in the expected way.

To further improve the recovery of faint emission on scales extended with respect to the relevant scales discussed in section 6.1.1, another modification to the method described by Enoch et al. is possible. Rather than constructing the template by masking parts of the map, the template is constructed by re-scaling the signal-to-noise map according to $T_i = M_i/R_i$, with

$$R_i = \left(\frac{W_i}{\max(W_i)}\right)^{-\frac{1}{2}}, \tag{6.10}$$

where W_i is the weight map (see above). Such a template has the same signal amplitude as the raw map at the maximum of the weight map, and scales down with the inverse of the noise in other regions. The obvious advantage of this modification is that also signal components below the chosen cutoff are taken into account, although typically they are reduced if they are far from the position of maximal coverage. On the other hand, because of this down-scaling with inverse squared weight, it can require many iterations to recover the full signal distribution, with an increased risk of noise artifacts being amplified by the iterative process as a result.

Figure 6.5 shows the results of reducing one hour of bootstrapped LABOCA data with an added bright artificial source constructed from two beta profiles separated by $100''$. Both profiles have $\beta = 1.5$. The first profile is broad, with $r_c = 120''$ and a peak flux of 0.09 Jy, while the second profile is narrower with $r_c = 30''$ and a peak flux of 0.15 Jy. The beta profiles have been truncated at $3\,r_c$ using the method described by Battye & Weller (2003).

The data were taken using spiral scans with inner and outer radii of $140''$ and $180''$, respectively, with each scan consisting of four spirals separated by $100''$ in azimuth and elevation.

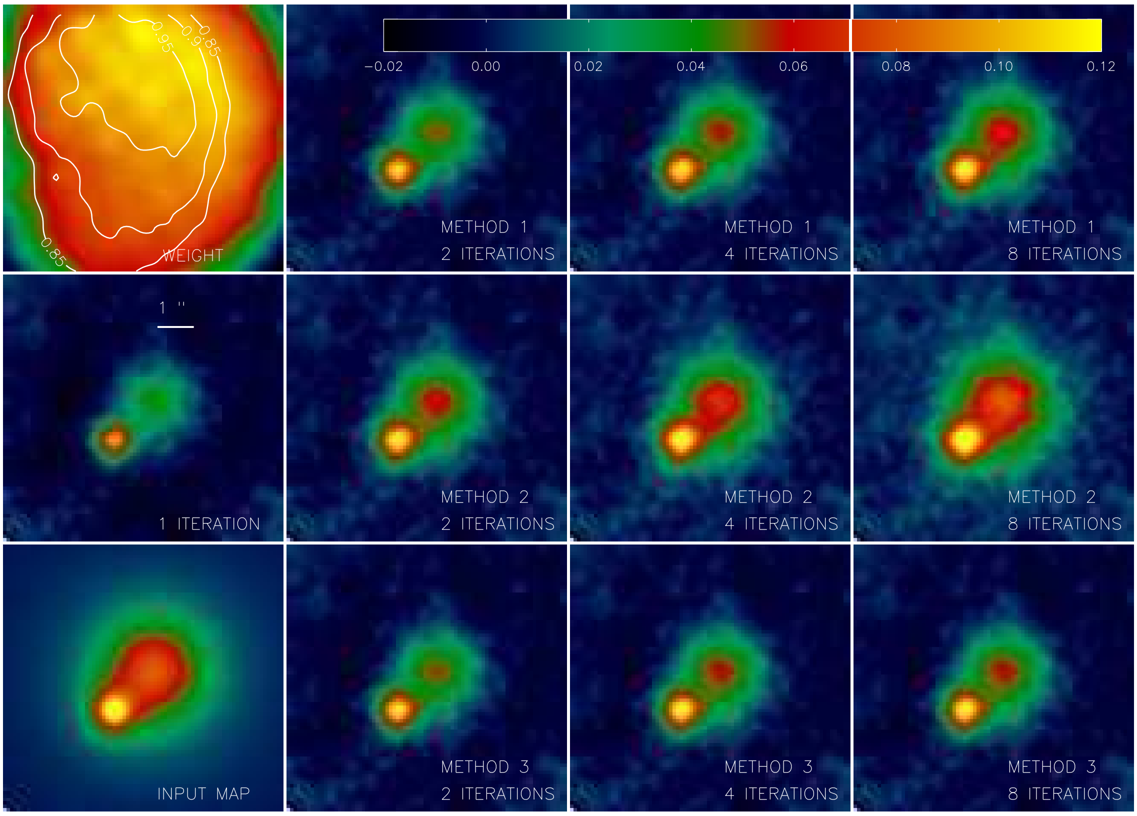

Figure 6.5: Results of reducing a data set with an artificial composite source using three different iterative mapping algorithms; the signal-to-noise map approach (method 1), the standard iterative mapping approach (method 2) and the method described by Enoch et al. (method 3). See text for details.

The region of the simulated emission is thus comparable to the size of the scan pattern, and it cannot be expected that the emission is recovered without a highly specialized reduction algorithm.

The results are consistent with what one would expect; the method of Enoch et al. (method 3 in Fig. 6.5) fails to recover the extended emission no matter how many iteration are done because eventually the recovered flux in the residual map falls below the cutoff limit and is (erroneously) regarded as noise. Using the scaled signal-to-noise map as the template (method 1 in the figure) helps to relieve this problem, but instead regions of low weight are suppressed in every iteration step. The most efficient method in this example case is the standard iterative mapping approach; this is the only method by which the signal in every pixel of the map is consistent with the input map, within the pixel noise, after 8 iterations. It remains the only consistent map after 16 iterations (not shown in the figure).

terative map making provides no universal solution to the problem of recovering extended emission. As stated earlier in this chapter, emission that is completely rejected by various spatial filters (including the filtering effects of the scan pattern) is always irrecoverable; only those spatial scales can be recovered on which a significant fraction of the signal (above the noise) is already recovered in a *single* iteration.

6.6.4 Map Deconvolution

As discussed in § 6.4, any model can be fitted to a reduced map using the transfer function; assuming the filter function of the reduction is linear, the raw map corresponds to the actual source distribution convolved with the beam. In many cases, however, it is desirable to use the transfer function directly to deconvolve the raw map to the resolution of the instrument, e.g. when using the data for non-parametric analyses such as de-projecting the temperature and pressure structure of a complex system (cf. chapter 9).

De-convolving a map is simple, but difficult. It is simple in the sense that the process is well-defined; it corresponds mathematically to a division in Fourier space. This division, however, cannot be done directly in the presence of noise; noise components close to the beam scale will typically dominate the operation, resulting in artifacts on large physical scales in the map. For this reason, iterative deconvolution algorithms such as maximum likelihood or minimum entropy are widely used in varying physical applications where deconvolution is required. However, these algorithms are impractical here since the deconvolution kernel (the transfer function) typically has significant features on angular scales as large as the map itself.

To solve this problem, an alternative iterative approach has been developed. It is similar to the CLEAN algorithm developed for synthesis imaging (Högbom 1974, Schwarz 1978) in that the source is modeled as a sum of many point sources with respect to the instrument beam. A major difference compared to CLEAN is that the process is carried out in map space rather than Fourier space. Furthermore, the transfer function is not strictly a point-spread function as it does not necessarily integrate to one (as the beam point-spread function does), whereas in CLEAN, the "dirty beam" integrates to the same value as the clean beam. De-convolving a bolometer image in this way will thus not conserve the integrated flux in the map.

The iterative deconvolution algorithm is simple. The raw map M_0 is first *convolved* with the beam (§ 6.6.2) to reduce the sample variance on small spatial scales. Each pixel in the map is then divided by the local rms to create a signal-to-noise map N_0, from which the brightest pixel is selected. The point source flux corresponding to this peak pixel value is computed, taking into account both the beam smoothing of M_0 and the complete description of the inherent resolution combined with the effects of the reduction described by the point source transfer function. The resulting point source is re-convolved with the transfer function to represent how the point source is reflected in the raw map. This component is subtracted from M_0 to yield M_1, from which a new smoothed signal-to-noise map, N_1, is constructed. The point source is also convolved with the "clean" beam and added to a (previously empty) map, C, of "clean components". Next, the brightest pixel in N_1 is located, and the process is repeated until M_i is consistent with noise. At this point, M_i is added to the cumulative map C to account for emission that has not been successfully removed as point sources. The process is illustrated in Figure 6.6, in which the deconvolution technique is applied to an APEX-SZ map of the Bullet cluster (1ES0657−56, see chapter 7 for a description of the data and its reduction).

The CLEAN algorithm generally assumes that all sources are positive with respect to the background. Since the SZ signal at 150 GHz is always *negative*, one might argue in favor of iterating only on negative peaks in the map, at least for APEX-SZ observations. However, this approach is not robust since the deconvolution process does not preserve the integrated flux in the map; it is unavoidable that some steps of the iteration will recover components that consist at least partly of noise. Furthermore, actual point sources (radio or sub-mm sources;

see chapter 3) will not be properly taken into account if a purely negative signal is assumed.

Recovering the diffuse and extended emission in the outer regions of a galaxy cluster (beyond the X-ray core radius) requires many iterations since a beam-convolved point source is very narrow, and the SZ emission from a galaxy cluster is expected to decrease slowly with radius in comparison. In general it cannot be expected that any part of the SZ emission has been recovered in a region where no point sources were fitted. Though the deconvolution process is straightforward, it is delicate in the sense that the number of iterations must be carefully chosen: too few iterations will underestimate the SZ flux, while with too may iterations it is possible to introduce noise artefacts by amplifying regions of large-scale variations in the map coming from unfiltered atmospheric noise. A useful strategy is to stop iterating when a roughly equal number of positive and negative point source models are being fitted, indicating that one is starting to de-convolve the noise.

Systematic losses of signal in the combined reduction and deconvolution process are highly dependent on the source morphology, the scan strategy and the transfer function of the reduction used, and are thus difficult to quantify in general. In specific cases, systematic offsets can be easily simulated, and to confirm that a de-convolved map is consistent with the data, it is straightforward to run a reduction with the de-convolved map subtracted in time series space and adding it back in after reduction, in analogy with the iterative mapping algorithm in the previous section.

6.6.5 Spatial Filtering of Maps

Although standard reduction includes direct high-pass filtering of the time signal to limit large scale artifacts, additional filtering in *map* space is sometimes necessary. This is particularly true when the scan speed is not constant over the whole scan, or when the scan pattern itself limits the use of time signal filtering.

Spatial filters can take many forms. For the purpose of filtering maps from APEX-SZ, Butterworth filters are used. In frequency space, this class of filters take the form

$$G = \frac{1}{1 + C\left(\frac{R}{R_0}\right)^{2n}}, \tag{6.11}$$

where R is the frequency image of the map, R_0 is the nominal filter cutoff frequency and C is typically set to 1.0, normalizing the magnitude of the filter at $R = R_0$ to $1/\sqrt{(2)}$. n is the order of the filter, and is usually set to 2. In practice, R_0 scales as the inverse of a number of pixels in map space, corresponding to the desired cutoff scale of the high-pass filter. Filtering is done by Fourier-transforming the map using FFT, then multiplying with G and performing the inverse transform.

Direct filtering of maps using the Fourier filter given by Eqn. (6.11) is possible. However, because of the uneven coverage of co-added bolometer maps even in limited regions, this is not optimal since the high contrast (due to higher rms) in regions of lower coverage can potentially come to dominate the filtering process. For this reason, each map pixel is multiplied by the square root of its weight before filtering. This factor is then divided out again, under the assumption that the weight maps before and after filtering are identical. For numerical reasons, pixels with no data are assigned the value zero during the filtering process.

For reasons of coverage, filtering is preferentially applied to co-added maps rather than individual ones. Consider two maps m_1 and m_2 to be co-added as described in section 6.6.1. Because of the associative property of convolution, it holds that

$$m_{\text{tot}}^{\text{filtered}} = m_1^{\text{raw}} * g + m_2^{\text{raw}} * g = (m_1^{\text{raw}} + m_2^{\text{raw}}) * g, \tag{6.12}$$

where g is the filter in *map* space (not Fourier space; G is the Fourier transform of g). Although it thus formally makes no difference whether one applies the filter g before or after co-adding, the later is preferred because maps containing many pixels without data can be corrupted in the filtering.

At present, BoA contains no function or method to perform spatial filtering of maps. All such filtering, where applicable to maps presented in this thesis, has been performed using the interactive data language (IDL).

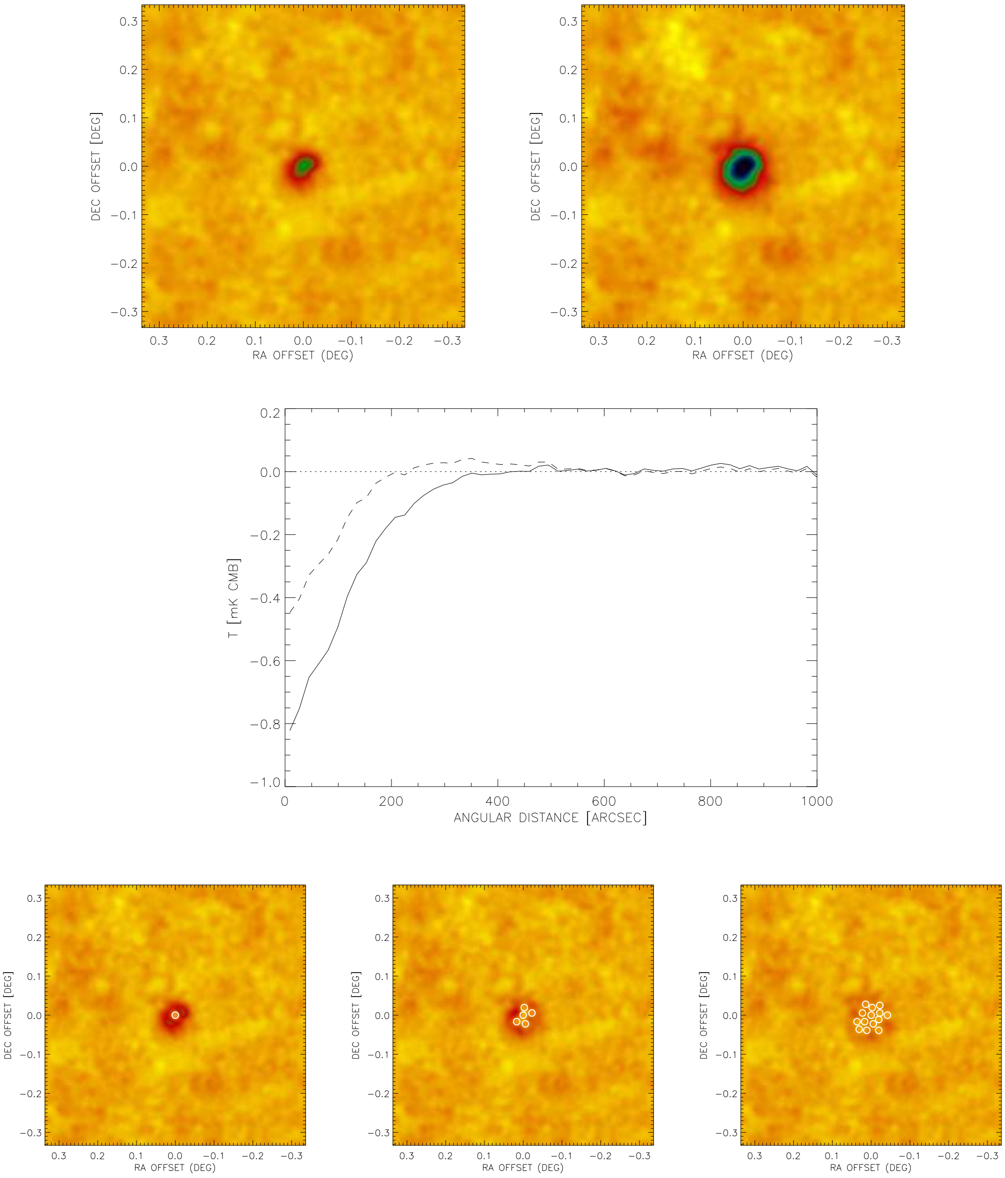

Figure 6.6: Iterative deconvolution using a sum of beam-convolved point sources, applied to an APEX-SZ map of the “Bullet” cluster (1ES0657−56). The top row shows the raw, beam-convolved signal-to-noise map on the left, followed by the de-convolved map after 125 iterations. The radial profiles of the raw and de-convolved maps are shown as the dashed and solid lines, respectively, in the middle panel. The bottom panels show “snapshots” of the deconvolution process, with removed point sources marked with circles (the circle diameter corresponds to the beam FWHM). The residual maps M_i (see text) are shown for $i = 1$, $i = 5$ and $i = 14$. The color scale is arbitrary, but the same in all maps shown.

Chapter 7

First Results from the APEX-SZ Experiment

This chapter summarizes the results of all targeted cluster observations with APEX-SZ between March 2007 and May 2008. Observations were carried out in four observing periods: (I) March 24 – April 14, 2007; (II) August 8 – September 5, 2007; (III) December 11–29, 2007 and (IV) May 24 – June 1, 2008. Out of 13 targeted clusters, 9 significant detections were made. In addition, one tentative detection was made of a previously known, not targeted cluster located close to one of the targets, and of the remaining four targets there are two tentative detections.

The targets cover a wide range in redshift and mass[1]. The detailed modeling of individual nearby clusters, using the tools described in the previous chapter, is made possible by a combination of the high sensitivity, the large field-of-view and the one arcminute resolution of APEX-SZ.

The targets are listed in § 7.1, where the observing strategies used in each case are summarized. § 7.2 outlines the pipeline reduction and basic diagnostics of the data from the different observing runs. The raw reduced maps are presented in § 7.3, and § 7.4 gives the results of modeling each cluster isothermally using the β model discussed in previous chapters. Systematic errors on extracted parameters are discussed in § 7.5. Results are presented in § 7.6, and notes on individual clusters are given in § 7.7. The results are summarized in § 7.8.

7.1 Targets and Observations

All individually targeted clusters in the four observing periods are listed in Table 7.1, which also gives information on the number of hours spent on each target and the observing strategy used. In total, 210 hours were spent on the targets.

All cluster targets in the sample are selected from X-ray observations. The most observing time was spent on XLSSC 006; this cluster field also has an extended region of coverage through large drift circles and additional scans with offsets from the cluster center, mostly from observing periods II and III. In this field, a second decrement was found. The decrement can be identified as the SZ signal of the cluster XLSSJ022157.4−034001 (Andreon et al. 2005) at a redshift of approximately 0.8 (estimated photometrically from the R−z color).

---

[1] Mass projected from X-ray derived ICM temperature; see § 3.3.2 for a description of the mass-temperature scaling used in this thesis, and 7.6 for X-ray determined ICM temperatures in the present sample

Table 7.1: Targets of APEX-SZ observations between March 2007 and June 2008, sorted by ascending redshift.

Name	Alternative name(s)	Redshift z	Total integration time^a (h)	Observing mode^b
RXCJ1632.7+0534	Abell 2204	$0.152^{(1)}$	16.3 (IV)	DRC
RXCJ2014.8−2430		$0.161^{(2)}$	9.6 (II)	DRC
RXCJ0645.4−5413	Abell 3404	$0.167^{(3)}$	4.7 (II)	DRC
			4.0 (IV)	DRC
RXCJ1615.7−0608	Abell 2163	$0.202^{(1)}$	11.9 (I)	OTF
			0.7 (II)	DRC
RXCJ2248.7−4431	Abell S1063	$0.252^{(3)}$	6.8 (I)	OTF
RXCJ2308.3−0211	Abell 2537	$0.295^{(4)}$	14.5 (IV)	DRC
1ES0657−558	Bullet	$0.296^{(5)}$	3.9 (I)	OTF
			7.6 (II)	DRC
RXCJ0014.3−3022	Abell 2744	$0.308^{(6)}$	7.8 (IV)	DRC
XLSSC 006		$0.429^{(7)}$	38.4 (II)	DRC
			30.9 (III)	DRC
RXJ1347.5−1145		$0.451^{(8)}$	7.0 (I)	OTF
			0.8 (IV)	DRC
MS1054.5−0321		$0.826^{(2)}$	1.2 (IV)	DRC
RDCS1252.9−2927		$1.237^{(9)}$	15.6 (II)	DRC
			17.0 (III)	DRC
XMMXCSJ2215.9−1738		$1.45^{(10)}$	11.6 (II)	DRC

[a] In the respective observing periods: (I) March 24 – April 14, 2007; (II) August 8 – September 5, 2007; (III) December 11–29, 2007 and (IV) May 24 – June 1, 2008.

[b] DRC: drift circle, OTF: horizontal raster scan.

References : (1) Struble & Rood (1999), (2) Böhringer et al. (2004), (3) De Grandi et al. (1999), (4) Dahle et al. (2002), (5) Tucker et al. (1998), (6) Mitchell et al. (1999), (7) Andreon et al. (2004), (8) Schindler et al. (1997), (9) Demarco et al. (2007), (10) Stanford et al. (2006)

Most observations were carried out in drift circle mode (cf. § 5.2.7) as this has been found to maximize the signal-to-noise ratio in the target region. Several extended sources, such as the “Bullet” cluster and Abell 2163, were also observed with large horizontal raster scans, because this type of scans make it more straightforward to recover extended emission.

Raster scans of planets (usually Mars) were carried out daily to monitor array parameters (§ 5.2.1) and overall calibration (§ 5.2.3). Because differences in the pointing offsets and gains of individual bolometers from different planet scans within the same observing period are consistent within their uncertainties, only one (averaged) calibration file was made for each observing period. Skydip scans were carried out every few hours to monitor the atmospheric opacity. Typical opacity corrections are in the range of 2 – 10%.

7.2 Pipeline Reduction

7.2.1 Time Stream Reduction

After calibration, gain flat-fielding and bolometer position correction (chapter 5), all data is reduced with the same sequence of basic steps. In parallel with the reduction of each scan, a beam shaped source is reduced to create a point source transfer function (§ 6.5). The main steps are outlined here; see chapter 6 for details on each step.

Correlated noise is removed in three steps of median noise removal (§ 6.2.2), with one iteration in the first step and two iterations in the subsequent ones. Between each step, noisy channels are flagged. Correlated noise gains are computed only with respect to the data; these gains are then also applied to the beam data for the transfer function. Deglitching and despiking at a level of 5 sigma is done prior to the removal of the low-frequency component in the time streams. In all flagging steps, the flags are copied directly from the astronomical data to the transfer function data as described in § 6.5.

Rather than applying a direct filter, such as a Butterworth filter, to the time streams for high-pass filtering, polynomials are fitted to and subtracted from subscans as this method has been found to be more robust on heavily flagged time streams. Subscans are defined as full circles in the horizontal system for drift circle scans. The first full circle of each scans is always flagged due to known problems with telescope pointing. For horizontal raster scans, subscans are defined as the central 90% (in arc length, not in time) of each scan segment with unchanging scan direction in azimuth. The remaining 10% (turnarounds) are flagged. Subscans are similarly defined for equatorial raster scans, although there are very few ($< 1\%$) such scans.

The order of the polynomial baseline applied to each subscan is determined from the arc length of the subscan according to Table 7.2.

Table 7.2: Orders of polynomial baselines applied to subscans of time stream data in different scan modes.

Arc length of subscan ($'$)	polynomial order (rasters)	Arc length of subscan ($'$)	polynomial order (circles)
< 15	3	< 8	1
$15 - 20$	5	$8 - 15$	3
$20 - 25$	7	$15 - 20$	5
> 25	9	> 20	7

For drift circle scans, a further airmass correction is applied to each bolometer time stream by fitting to a normalization, a, of the function

$$a \sec(e)\,, \tag{7.1}$$

where e is the elevation angle.

After polynomial baselines have been applied, the time streams are despiked again, at a level of four sigma. This step is followed by a final flagging of noisy channels before weighs are computed from the rms noise of the subscans. To avoid abnormally large weights due to a lack of data points, subscans with more than half of the samples flagged are removed. This typically corresponds to a very small part of the data; in observing period (I) only 0.3% of the total integration time is flagged due to this criterion.

7.2.2 Diagnostics and Scan Flags

Before co-adding any scans to make maps, care must be taken to remove bad data that has not already been flagged in the time stream domain. Because individual scan maps have already been made at this point, flagging is now limited to the removal of whole scans. In particular, certain properties of the power spectrum of time streams can conspire with the scan speed to create artifacts in a map, such that the weight map (§ 6.6.1) does not provide a meaningful measure of the *map* noise properties, although the weights of the individual time streams give a reasonable description of noise in terms of rms. An example is given in Figure 7.1, where a scan from observing period (III) is shown to exhibit excessive low-frequency power in the map. The weight is computed from rms, which corresponds to integrating along the time stream power spectrum.

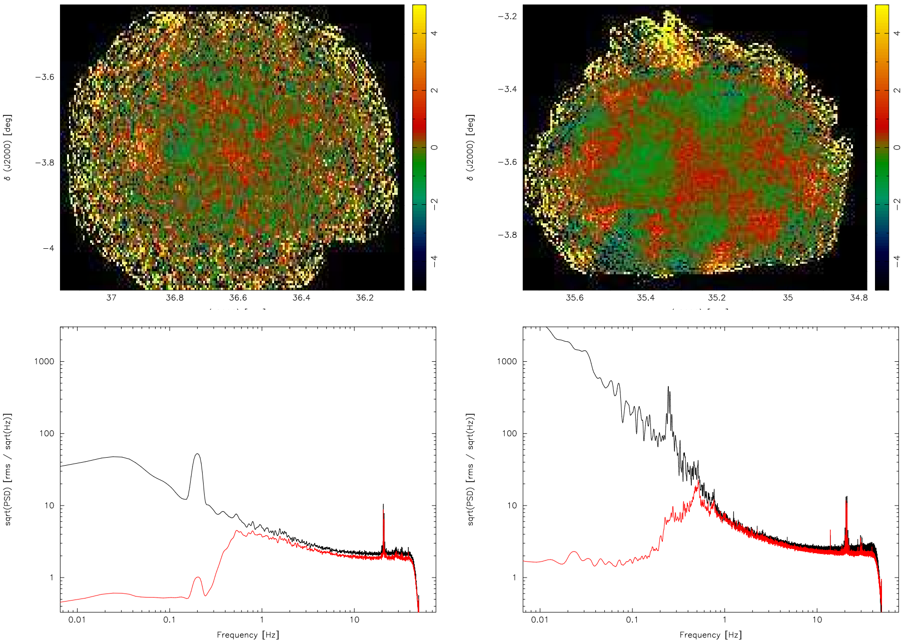

Figure 7.1: Comparison of a typical August 2007 (period II) scan (left) and a December 2007 (period III) scan with a large low-frequency component. The top row shows the raw scans maps, cut at ± 5 $\mathrm{mK_{CMB}}$. The exposure of the December scan is five times as long as for the August scan. The bottom row shows the mean time stream power spectra before (black) and after (red) reduction. The “bump” at 0.2 Hz in the left power spectrum comes from the atmospheric airmass component introduced through the circular scan pattern.

For these reasons, the central rms of each scan map is recomputed independently of the weight map. All central rms values found in this way are compared to the cental weight measures, and scans with rms values exceeding the prediction from the central weight by more than 30% are flagged. This is a particular problem in observing periods (III) and (IV), where over 30% and 20% of the scans, respectively, are flagged for this reason. The main reason for this problem is unsuitable weather (APEX-SZ has been used extensively as a backup instrument in time periods with high opacity), which seems to introduce large amounts of noise correlated on scales of only a few arcminutes. This noise component cannot be removed by algorithms considering the median correlated noise over the whole array. It could be removed using alternative algorithms considering correlations only between groups of strongly correlated channels, but the small spatial correlation scale required for this would also result in the removal of any source signal larger than a point source.

Scans are also flagged on a basis of unusually high noise, as indicated in Figure 7.2. Exceedingly *low* noise levels are also apparent. These are artificial and result from inappropriate gain settings of the instrument at the time of observations, usually immediately preceding the observation of a bright pointing source. Scans with exceedingly low noise are thus flagged in addition to those exhibiting high noise levels. Staring scans (no scan pattern) and scans with median scan speeds of less than $30'' \, s^{-1}$ are excluded, as are scans where more than 30% of the samples have been flagged due to deglitching or despiking.

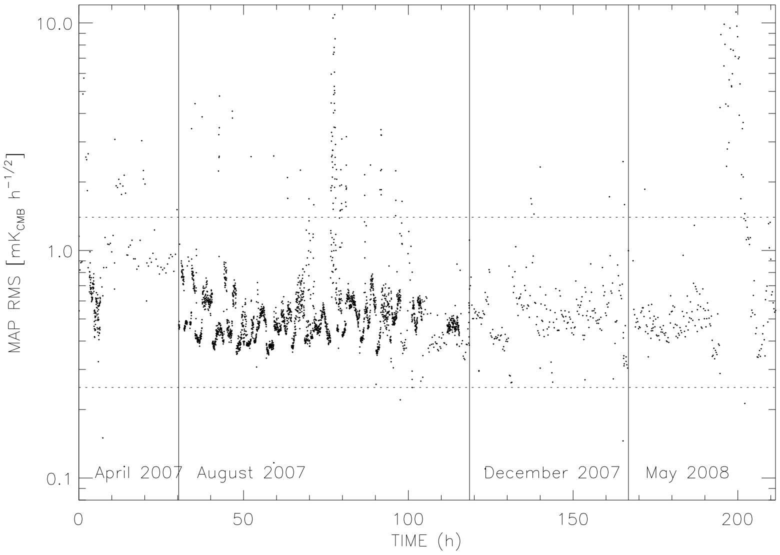

Figure 7.2: Map rms (per square root of integration time) for all reduced scans in four observing periods. The time unit on the x-axis is a cumulative measure of on-source integration time on the targets. Scans with reduced map rms above and below the dotted lines are flagged.

Although the aforementioned conditions are generally quite effective in removing bad data, a number of bad scans remain. Problems include cases of the transfer function being corrupted due to numerical problems, or artifacts in map space that are not identified by the methods discussed. Scans exhibiting such problems are identified by visual inspection.

7.2.3 Mapping

After the automatic and manual flagging steps are complete, all non-flagged scans are combined into one square degree map per target (with the exception of the XLSSC 006 field, where the map size is 1.5° × 1°). The pixel size in each map is $10'' \times 10''$, or approximately one sixth of the beam. The total transfer function for each target field is computed by co-adding all transfer maps corresponding to non-flagged scans.

7.3 Detections and Transfer Functions

Out of thirteen targeted clusters, nine are clearly detected as indicated in Figure 7.3. These clusters all have a peak signal-to-noise ratio larger than 5 in the beam smoothed map.

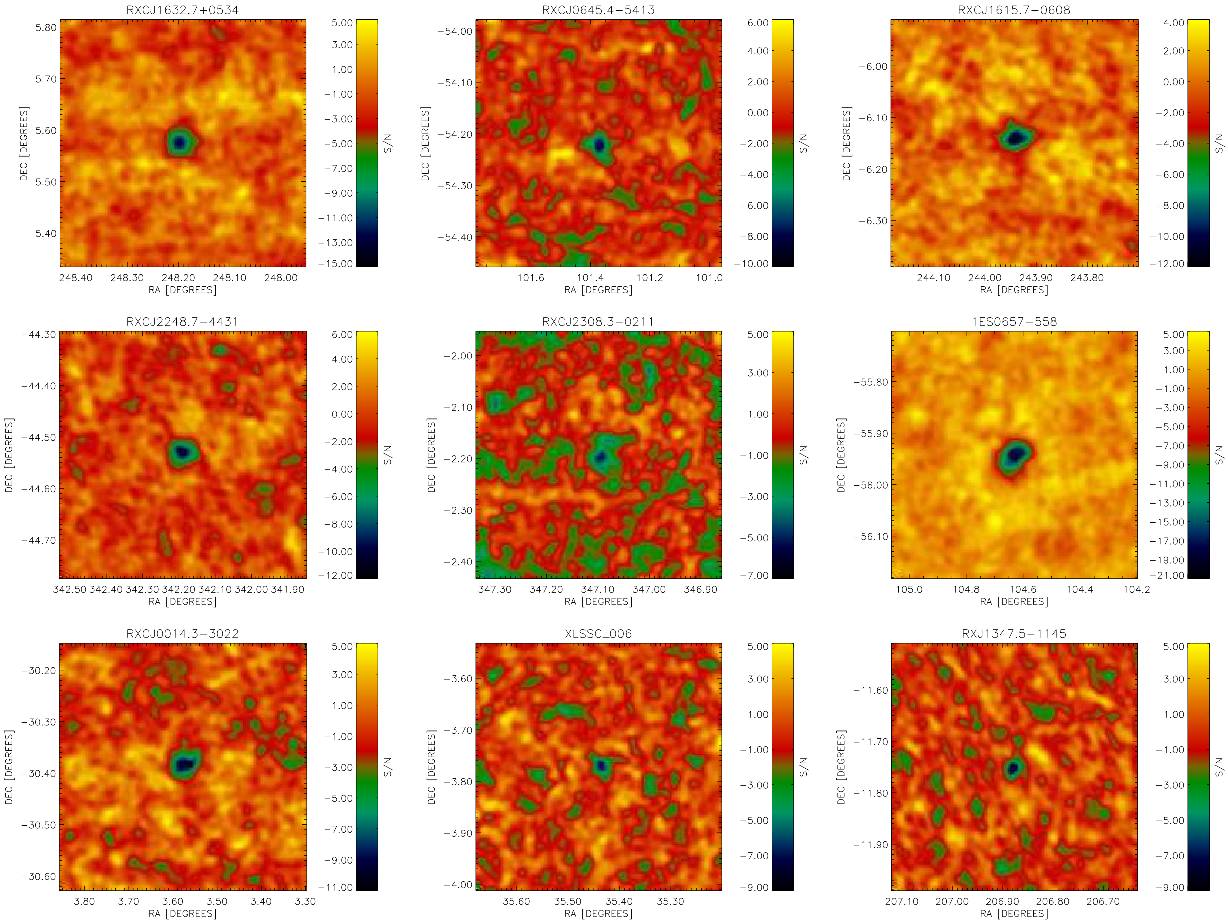

Figure 7.3: Signal-to-noise maps of nine clusters with definite APEX-SZ detections. All maps have been convolved with the APEX-SZ beam.

Marginal detections, defined as having peak signal-to-noise ratios in the range of $3 - 5$, are presented in Figure 7.4. The cluster XMMXCSJ2215.9−1738 at redshift $z = 1.45$ does have a peak decrement consistent with a 5 sigma detection. However, the detection is classified as marginal because the peak signal is inconsistent with the X-ray center of this cluster by more than one arcminute. The cluster XLSSJ022157.4−034001 (not targeted) in the XLSSC 006 field is also marginally detected. Non-detections are indicated in Figure 7.5.

Central noise levels (rms) are computed by inverting and taking the square root of the co-added weight map of each field (see § 6.6.1). Because the noise power spectra of the time

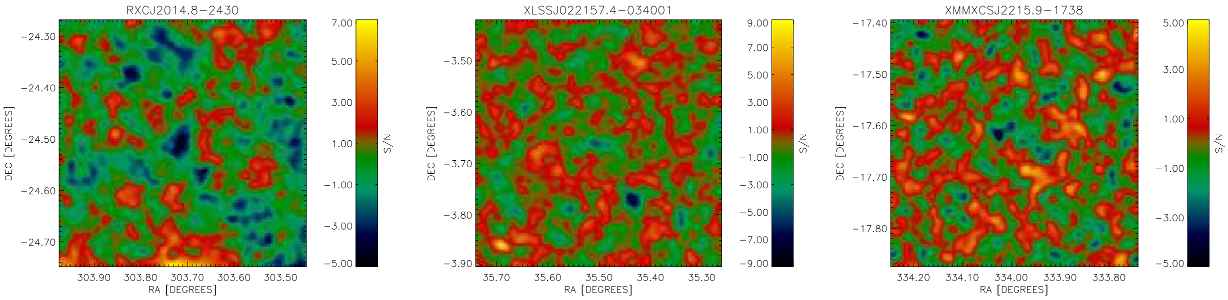

Figure 7.4: Like Figure 7.3, but for the three marginal APEX-SZ detections of galaxy clusters. Although the negative signal in the map of XMMXCSJ2215.9−1738 looks significant, it has a large offset from the X-ray center, which is in the center of the map. In the map of XLSSJ022157.4−034001, the significant detection of XLSSC 006 (Fig. 7.3) is visible to the lower right.

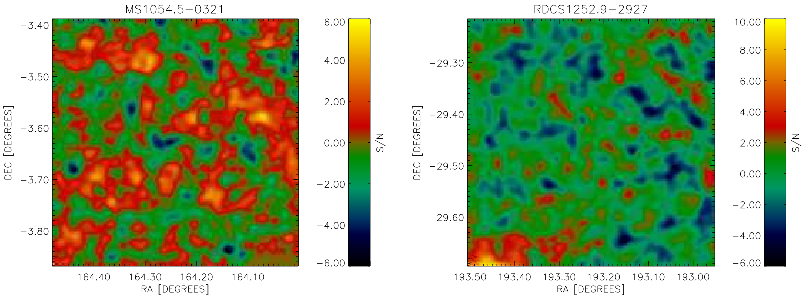

Figure 7.5: Signal-to-noise maps of two targeted cluster fields with no significant detections: MS1054.5−0321 and RDCS1252.9−2927. Note that only about one hour of observing time was spent on MS1054.5−0321.

signals are seldom flat, the result of this operation has to be re-scaled to match the actual noise in the co-added map. For this purpose, the source region and regions of low coverage (less than one tenth of the central coverage) are flagged, and the rms is computed in circular regions with $8'$ diameter.

The median conversion factor (typically in the range 1.05−1.15) from predicted to actual rms is then applied to the whole map to create an rms distribution. The results are presented in Table 7.3 along with the significance of each detection.

It is clear from the central rms values that a significant detection can be made much faster with drift circles than with horizontal raster scans, owing to the fact that the former scan strategy concentrates the coverage on a much smaller region on the sky (roughly half the area covered by the raster scans used for RXCJ1615.7−0608 and RXJ1347.5−1145). The clear advantage of raster scans, on the other hand, is the ability to baseline the data independently for each bolometer in regions where the emission is negligible. However, comparing the data of fields covered in both observing modes (e.g. RXCJ1615.7−0608, RXJ1347.5−1145 and 1ES0657−558) reveals that the difference in the recovered *peak* signal is marginal, and that the point source transfer function does equally well in both cases with respect to modeling the

Table 7.3: Noise levels in maps and significance levels of detections. Significance levels apply to the raw (not de-convolved) maps.

Cluster name	Cental r.m.s.[a] (μK$_{\mathrm{CMB}}$)	Significance (σ)
RXCJ1632.7+0534	21	−13.1
RXCJ2014.8−2430	29	−3.9[b]
RXCJ0645.4−5413	22	−7.9
RXCJ1615.7−0608	35	−11.8
RXCJ2248.7−4431	47	−10.7
RXCJ2308.3−0211	19	−5.3
1ES0657−558	20	−19.7
RXCJ0014.3−3022	31	−10.0
XLSSC 006	9	−7.25
XLSSJ022157.4−034001	9	−3.2[b]
RXJ1347.5−1145	47	−8.7
MS1054.5−0321	80	–
RDCS1252.9−2927	14	–
XMMXCSJ2215.9−1738	15	−5.1[c]

[a] r.m.s. on the beam scale at the position of the source

[b] marginal detection

[c] significant level of detection, but the center position is offset from the X-ray emission (see text)

underlying emission profile. The details of the latter are elaborated in section 7.4.

Figure 7.6 shows a sample of point source transfer functions for six of the targeted fields. Transfer functions from circular scans are typically close to azimuthally symmetric with a negative "side lobe" extending to a radius of several beams. This feature is readily seen as *positive* artifacts around the detections in Figure 7.3. At a radius corresponding to the *diameter* of the scan pattern, a second feature appears as a positive ring. Raster scan transfer functions tend to be affected in the scan direction through the removal of polynomial baselines. For this reason, bright and dark bands appear in directions corresponding to the azimuth direction rotated into equatorial coordinates at different times. Note that a transfer function typically has features on scales comparable to the size of the corresponding map. This is emphasized in Figure 7.7, which shows the radial profile of a transfer function from a field covered by drift circle scans.

7.4 Isothermal Modeling

7.4.1 Method

To make a quantitative description of the emission distribution of each cluster, the isothermal β model (§ 2.2.4) is used. This enables a straightforward way of comparing the gas properties from the SZ measurements to those derived from X-ray observations. The isothermal β model relies on the assumptoion of hydrostatic equilibrium (§ 2.1.6), which is unjustified for several of the target clusters (e.g. 1ES0657−558, Clowe et al. 2006, and Abell 2163, the subject of chapter 9). However, given the sensitivity and spatial resolution of the present observations, the

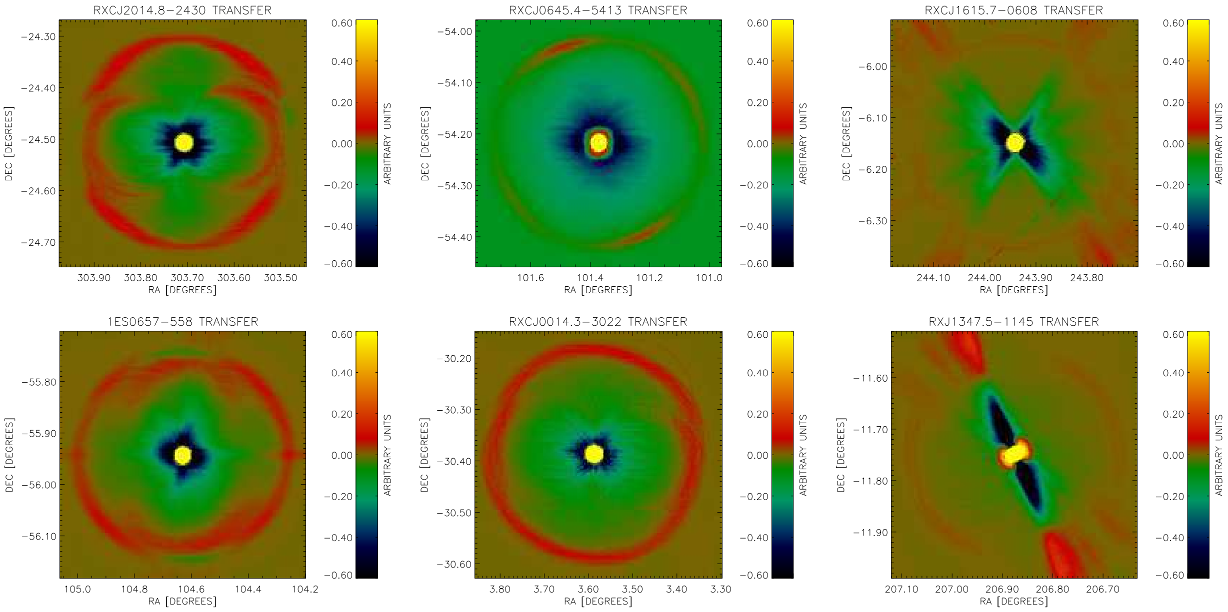

Figure 7.6: Typical point source transfer functions for different scan strategies and combinations thereof. *Left column:* Drift circles with different radii. *Middle column:* Drift circles, all scans using the same circle radius. *Right column:* Horizontal raster scans (*top*) and horizontal raster scans combined with drift circles (*bottom*).

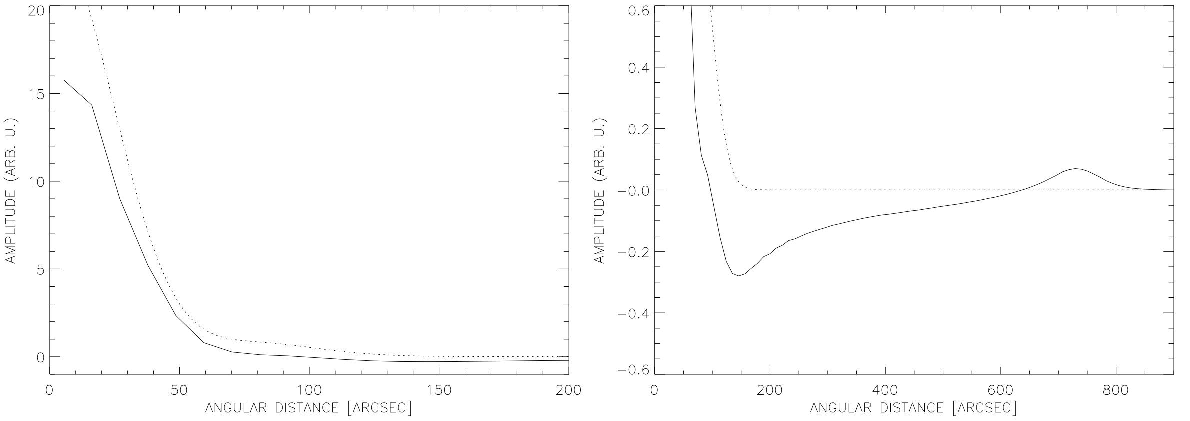

Figure 7.7: Radial profile of the transfer function (*solid lines*) in the RXCJ0645.4-5413 field (Fig. 7.6) compared to a Gaussian model of the APEX-SZ beam (*dotted lines*). The left panel shows the central region only, whereas the right panel shows the details of the low-amplitude part of the transfer function.

model provides a reasonable description of the emission. In particular, an isothermal spherical

β profile can be fitted to each cluster in such a way that subtracting the fitted result from the map yields a residual consistent with noise.

Following Halverson et al. (2008), the fit is done by convolving a model function of the form

$$\Delta T = \Delta T_0 \left(1 + \frac{\theta^2}{\theta_c^2}\right)^{-\frac{3}{2}\beta+\frac{1}{2}}, \tag{7.2}$$

with the point source transfer function, by differencing the convolved model with the data and adjusting the model parameters to minimize a χ^2 statistic. In addition to the normalization (peak SZ decrement) ΔT_0, the power law index β and the core radius θ_c, the model parameters also include the RA and DEC centroid positions. Note that Eqn. (7.2) expresses radial distances in terms of angles on the sky, such that

$$\theta = r/D_A,$$

with r a physical distance (projected in the plane of the sky) and D_A the angular diameter distance.

Due to the fact that the transfer function typically has features on large angular scales, the convolution of the model with the transfer function is done using the fast Fourier transform (FFT). Unlike the analysis of Halverson et al. and the analysis of Abell 2163 described in chapter 9, the present analysis is limited to spherical β profiles.

Given the APEX-SZ beam width and the significance levels of the present detections, the degeneracy between β and θ_c cannot be broken except in certain cases where a high level of significance is combined with the detection of the SZ decrement out to large radii (see chapter 9). Following LaRoque et al. (2006), β is set to a fixed value, and all other parameters are allowed to reach their best-fit values. A sub-sample of the targets is also modeled using β values from X-ray measurements.

7.4.2 Modeling of Statistical Errors

Statistical uncertainties in the fitted β profiles are estimated using a simple Monte Carlo approach. The map data is bootstrapped (chapter 6) by inverting the sign of half the individual scan maps (cf. § 6.5.3), and the maps are co-added to generate a pure noise map. In cases where there are too few ($\lesssim 30$) scans of roughly equal integration time to make this approach possible, the data are further divided by making several maps from each scan. After convolving the best-fit model with the transfer function and adding the result to the noise map, the χ^2 statistic is again minimized to find the best set of parameters for the map with simulated noise properties. The entire procedure is repeated 1000 times, upon which the errors in the respective parameters are taken as the scatter in the distributions of their fitted values (marginal likelihood distributions). Systematic uncertainties arising from the primary CMB, galactic dust, resolved and unresolved point sources and fitting errors originating in the use of the transfer function are discussed in the next section.

7.5 Systematics

7.5.1 Primary CMB

For very extended clusters (such as RXCJ1615.7−0608, 1ES0657−558 and RXCJ0014.3−3022, which all have virial radii extending far beyond ten minutes of arc), the primary temperature anisotropies in the CMB are a potential source of confusion in the SZ measurements. This uncertainty particularly affects the kinematic SZ signal, because the latter has a frequency dependence identical to that of the CMB thermal spectrum. However, due to the indirect high-pass filtering of maps (both through polynomial baselines in the bolometer time series and through the scan pattern), any CMB power on scales $\gtrsim 20'$ contributes very little to the reduced maps.

To quantify the level of contamination, the *HEALpix* software (Gorski et al. 2005, cf. § 3.3.4) is used to generate 100 realizations of the CMB sky in a one square degree field (corresponding to the size of each map from the present sample with the exception of the XLSSC 006 field) with a resolution of $1.7'$. The input power spectrum for this generation is computed using the *CMBfast* code (Zaldarriaga & Seljak 2000) with the WMAP 5-year cosmology (Komatsu et al. 2008). Secondary CMB anisotropies other than the SZ effect are considered negligible.

Each primary CMB map is re-sampled as time streams corresponding to a typical scan of the SZ observations, and run through the pipeline using an approach similar to that described in § 6.5. For a given cluster field, the β model fit is repeated after adding each of the primary CMB realizations. The scatter in the results of each parameter is taken as the 68% systematic marginal error from primary CMB contamination.

To make the realization with *HEALpix* manageable, contamination on scales smaller than $1.7'$ is not taken into account. This is justified because the power drops rapidly on scales smaller than a few arcminutes (Hu & Dodelson 2002, Reichardt et al. 2009). The steep drop in power also means that smaller clusters will suffer less from primary CMB contamination, although factors such as different spatial filtering scales due to different scan strategies will also differentiate the results in the various cluster fields.

7.5.2 Galactic Dust

The FIRAS and IRAS experiments have measured the Galactic dust emission in the far-infrared (Schlegel et al. 1998), which have been used to predict the dust emission at sub-mm and mm wavelengths (Finkbeiner et al. 1999). Although dust proves to be more of a problem for SZ experiments at higher frequencies (cf. chapter 9), excess emission at 150 GHz cannot be ruled out, particularly in cluster fields close to the galactic plane.

To estimate the dust correction in each field, IRAS far-infrared 60μm and 100μm dust maps (Schlegel et al. 1998) are used. In each field, the 60μm map is smoothed to the $4.3'$ resolution of the 100μm map, whereupon both maps are re-sampled such that each pixel has a side of one arcminute. Extrapolation to 150 GHz is done using a grey-body spectrum of dust emissivity,

$$F_d \propto \frac{\nu^{3+\alpha}}{\exp(h\nu/k_{\rm B}T_d) - 1}, \tag{7.3}$$

where α is the dust spectral index. Using $\alpha = 2.0$ (Finkbeiner et al. 1999), a fit to T_d is carried out for every $1' \times 1'$ pixel pair in the two dust maps. Equation (7.3) is then used to extrapolate the intensity at 150 GHz, normalizing at 100μm.

The most simple way of removing the dust component from the data is to subtract it before any filtering is applied by the reduction. Thus, time streams are created corresponding to the extrapolated dust maps on the coordinates covered by APEX-SZ. These time streams are subtracted from the raw data before proceeding with reductions identical to those described in § 7.2. Corrections to the central decrement are given in Table 7.4. It is assumed that contamination on angular scales smaller than four arcminutes is negligible.

7.5.3 Radio Point Sources

There are no direct detections of point sources associated with a cluster in any of the observed fields. This is consistent with what one might expect given the limited resolution and the observing frequency, but since very little is known about the spectral slopes of radio sources, some amount of confusion cannot be ruled out. Systematic uncertainties can be estimated given radio measurements at a few frequencies to estimate the spectral slopes, and extrapolating with some model to 150 GHz. Because of the large uncertainties in spectral slopes, however, this source of confusion is not included in Table 7.4, but discussed separately for each cluster in section 7.7.

7.5.4 Sub-mm Point Sources

Unlike radio sources, extragalactic infrared point sources are not expected to correlate spatially with clusters of galaxies, and a distribution of sources can be well approximated by excess noise in any differential measurement (White & Majumdar 2004), thus having little or no systematic effects on the present SZ measurements.

Although lensing by a massive cluster can significantly increase the number of detected sources in the cluster central region, this effect conserves the total intensity of the background and only becomes important when faint sources are raised above the detection limit and removed, and the unresolved intensity is thereby systematically lowered (e.g. Loeb & Refregier 1997). Since there is no direct evidence of lensed sources in the 150 GHz maps, it is assumed that the systematic errors from lensed sub-mm point sources are negligible.

7.5.5 Modeling with the Point Source Transfer Function

To estimate the effects of the point source transfer function on the fitted parameters, the results of § 6.5.3 are used. For typical fitted values of θ_c the error in the central decrement is less than 3%, assuming the β model provides a good fit to the data in each case, although the systematic error in θ_c itself can be as large as 10%.

7.5.6 Summary of Systematic Uncertainties

Table 7.4 summarizes the systematic contributions and errors outlined in the above. Note that because the effects of galactic dust and the point source transfer function modeling are small in comparison to the absolute calibration and primary CMB errors, only the computed one-sided corrections are given, and no two-sided errors are considered.

7.6 Results

Table 7.5 gives the results of the β model fits with the power-law index β fixed to break the degeneracy with θ_c. All fitted values have been corrected for one-sided systematics (effects of the transfer function and dust emission, see Table 7.4), although quoted uncertainties indicate statistical errors only. Following LaRoque et al. (2006), a universal value of $\beta = 0.7$ is used.

Four of the detected clusters have well documented β values derived from X-ray measurements (Ota & Mitsuda 2004), including 1ES0657−558 which was modeled with X-ray priors on β by Halverson et al. (2008) using the present data. For these four clusters, additional β model fits are carried out using β values fixed to those of Ota & Mitsuda. The results are given in Table 7.6. In a single β model fit to the X-ray data, Ota & Mitsuda find a value of

Table 7.4: Estimated systematic errors and corrections in the central decrement T_0, in the context of β model fits to each cluster. Values are given in % of the fitted values given in Table 7.5. The last two columns give only the corrections to the fitted values.

Cluster name	Absolute calibration[a]	Primary CMB	Galactic dust[b]	Transfer function[b]
RXCJ1632.7+0534	±5.2%	±3.4%	−0.8%	−0.3%
RXCJ2014.8−2430	±5.3%	±2.9%	+1.2%	+1.1%
RXCJ0645.4−5413	±5.1%	±3.0%	+0.1%	+2.3%
RXCJ1615.7−0608	±5.4%	±3.5%	+0.6%	−0.5%
RXCJ2248.7−4431	±5.3%	±3.0%	−0.2%	+0.1%
RXCJ2308.3−0211	±5.2%	±2.8%	−2.2%	−2.5%
1ES0657−558	±5.6%	±3.1%	+0.1%	−2.5%
RXCJ0014.3−3022	±5.3%	±3.8%	−0.1%	+1.3%
XLSSC 006	±5.2%	±2.3%	−2.1%	+2.4%
XLSSJ022157.4−034001	±5.2%	±2.6%	−0.5%	−0.3%
RXJ1347.5−1145	±5.4%	±2.1%	−0.1%	+0.3%
MS1054.5−0321	±5.1%	–	–	–
RDCS1252.9−2927	±5.4%	–	–	–
XMMXCSJ2215.9−1738	±5.1%	±2.9%	−1.6%	−3.0%

[a] Includes uncertainties in the model used to determine opacity corrections. The median observing elevation of each field has been used to determine this uncertainty.
[b] Corrections applied to the fitted results in Table 7.5.

8.0″ for the core radius of RXCJ1632.7+0534. A better fit is found with a double β model, from which the outer core radius is used in the present analysis. Although 1ES0657−558 is also modeled with a double β model, it is dominated by the outer core and it thus makes more physical sense to compare the SZ result with the result of a single β model for this cluster.

The present results for 1ES0657−558 are in overall agreement with those of Halverson et al. (2008), although a different reduction scheme and error analysis technique were used in the latter study. The agreement between the two data reduction pipelines has been further corroborated by comparing the results of β model fits in the RXCJ1615.7−0608 and RXJ1347.5−1145 fields (A. Bender, personal communication).

Figures 7.8 and 7.9 show the SZ decrements of the target clusters at 150 GHz, overlaid on maps of the X-ray surface brightness in the 0.5 − 2 keV band from publicly available XMM-Newton data. The X-ray data has been reduced by F. Pacaud (personal communication) using the algorithm described in Nord et al. (2009) and has not been corrected for point source emission. Adaptive smoothing has been applied to the X-ray maps. For this comparison, the SZ maps with the most significant detections have been de-convolved with the transfer function using the iterative algorithm described in § 6.6.4. Positive and negative peaks in the map were treated indiscriminately, and iteration was continued until at least as many positive as negative peaks were found in any consecutive 20 iterations. Due to insufficient signal-to-noise ratios, the galaxy clusters RXCJ2014.8−2430 and XMMXCSJ2215.9−1738 have not been de-convolved.

A detailed comparison of X-ray and SZ maps is made difficult by the fact that the SZ maps are distorted by the respective transfer functions. Detailed analysis has to be carried out for each cluster to ensure that the de-convolution converges robustly. A detailed account

Table 7.5: Isothermal β model fit results. The power-law index β has been fixed at 0.7 for all clusters.

Cluster name	T_0 ($\mu\mathrm{K}_{\mathrm{CMB}}$)	θ_c ($''$)	RA[a]	DEC[a]
RXCJ1632.7+0534	−542±60	104±21	16:32:46.5±10″	+05:34:34.5±10″
RXCJ2014.8−2430	−249±99	75±33	20:14:52.0±12″	−24:30:44.8±11″
RXCJ0645.4−5413	−543±143	39±20	06:45:30.1±13″	−54 12 57.6±14″
RXCJ1615.7−0608	−758±59	135±18	16:15:45.5±9″	−06:08:27.2±10″
RXCJ2248.7−4431	−1242±270	62±23	22:48:45.3±11″	−44:31:53.7±12″
RXCJ2308.3−0211	−215±77	143±72	23:08:21.7±15″	−02:11:37.3±14″
1ES0657−558	−1015±48	144±17	06:58:31.5±8″	−55:56:47.4±9″
RXCJ0014.3−3022	−653±130	86±28	00:14:16.6±15″	−30:22:52.1±15″
XLSSC 006	−205±69	36±18	02:21:43.9±9″	−03:46:21.0±9″
XLSSJ022157.4−034001	−108±42	101±49	02:22:00.1±11″	−03:39:37.1±16″
RXJ1347.5−1145[b]	–	–	–	–
MS1054.5−0321	< 320[c]	–	–	–
RDCS1252.9−2927	< 30[c]	–	–	–
XMMXCSJ2215.9−1738	−151±49	180±55	22:16:00.2±15″	−17:36:12.3±15″

All uncertainties are 68% confidence intervals in the marginal likelihood distribution of each parameter.

[a] Fitted centroid positions. Units of right ascension are hours, minutes and seconds, and units of declination are degrees, arcminutes and arcseconds. Errors in RA and DEC are in units of arcseconds on the sky.

[b] The core region of this cluster is unresolved in the APEX-SZ beam. A simultaneous fit to θ_c and T_0 is thus not meaningful. A fit using a fixed value of θ_c is given in Table 7.6.

[c] Estimated upper limits from fitting a range of models with $0.6 < \beta < 1.2$ and applying the 68% error on the fitted T_0.

and comparison with the X-ray profile is given in chapter 9 for the cluster RXCJ1615.7-0608 (A2163). Here, a simple comparison is made in terms of fitted central SZ temperatures and the corresponding predictions from X-ray observations where ICM temperatures have been found in the literature (Table 7.7). To predict the SZ decrements, the simple approach of § 3.3.2 has been used.

Considering that different X-ray determined ICM temperatures for the same cluster often deviate by as much as 50% in the literature, and the large systematic uncertainties coming from modeling the SZ emission from X-ray properties, the results on the central temperature distortion due to the SZ can be said to be in reasonable agreement with the X-ray predictions.

7.7 Notes on Individual Clusters

7.7.1 RXCJ1632.7+0534 (Abell 2204)

X-ray observations of Abell 2204 indicate that this is a relaxed system in hydrostatic equilibrium. Projected temperature and density profiles have been constructed from deep X-ray images of this cluster (Sanders et al. 2005, Reiprich et al. 2008). In their isothermal modeling,

Table 7.6: As Table 7.5, but using fixed values of β from Ota & Mitsuda (2004) for a sub-sample of the clusters listed in Table 7.5.

Cluster name	β	θ_c (X-ray) ($''$)	T_0 (μK_{CMB})	θ_c (SZ) ($''$)
RXCJ1632.7+0534	$0.50^{+0.01}_{-0.01}$	56.2±11.7 [a]	−921±59	104±21
RXCJ1615.7−0608	$0.65^{+0.02}_{-0.01}$	87.4±7.2 [b]	−968±46	72±13
1ES0657−558	$1.04^{+0.16}_{-0.10}$	$112.5^{+15.6}_{-10.4}$ [b]	−1003±27	151±16
RXJ1347.5−1145	$0.69^{+0.30}_{-0.37}$	10.3±0.6 [b]	−1905±365	– [c]

[a] Outer core radius from double β model fit of Ota & Mitsuda (2004).

[b] Core radius from single β model fit of Ota & Mitsuda.

[c] Because the X-ray derived core radius is much smaller than the APEX-SZ beam FWHM, only T_0 was fitted, while β and θ_c were both fixed at their X-ray derived values.

Ota & Mitsuda (2004) find this cluster to be best fitted with a double β model, where the inner core radius is dominating.

The APEX-SZ detection is consistent with the overall X-ray properties of the cluster, however, its resolution is not sufficient to make a detailed comparison with the X-ray emission near the center. At redshift $z = 0.15$, one arcminute corresponds to 160 kpc; thus follow-up observations with LABOCA at 345 GHz are planned to compare the gas entropy profile with the X-ray derived value (Basu et al., in preparation).

Cooray et al. (1998) report two radio sources in the field of Abell 2204. They both have steep spectral slopes and are unlikely to be contaminating the SZ signal at 150 GHz.

7.7.2 RXCJ2014.8−2430

There is a large probability of radio source contamination in this cluster, a fact that was unfortunately overlooked in the APEX-SZ target selection. The NVSS catalog (Condon et al. 1998) lists a source approximately 26$''$ from the X-ray center, with a flux density of 230 mJy at 1.4 GHz. Even with a steep spectrum, this would correspond to 5.5 mJy at 150 GHz (assuming a steep spectral index $\alpha = 0.8$ in the conventions of chapter 3). This would offset the SZ decrement by about 140 μK_{CMB}. Comparing the predicted peak SZ flux of -560 μK_{CMB} at this frequency (projected from XMM-Newton) to the observed value of 249 ± 99 μK_{CMB} is indeed consistent with this crude estimate of the point source contamination.

7.7.3 RXCJ1615.7−0608 (Abell 2163)

Abell 2163 is a hot, X-ray luminous galaxy cluster at $z = 0.203$ with a mean X-ray temperature in the central region of $T_X = 12$ keV (Markevitch & Vikhlinin 2001). The X-ray analysis of A2163 suggests that this is a merger system (Elbaz et al. 1995, Govoni et al. 2004), with asymmetric X-ray temperature structures and strong radio halos. The merger scenario is also supported by optical observations, most notably from the presence of not only one but two bright cD galaxies (Maurogordato et al. 2008). This cluster is discussed further in chapter 9.

7.7.4 1ES0657−558 (Bullet)

The "Bullet" cluster is a massive system consisting of two sub-clusters, clearly evident in the X-ray image (Figure 7.8), in the process of merging. It is believed that the smaller subcluster

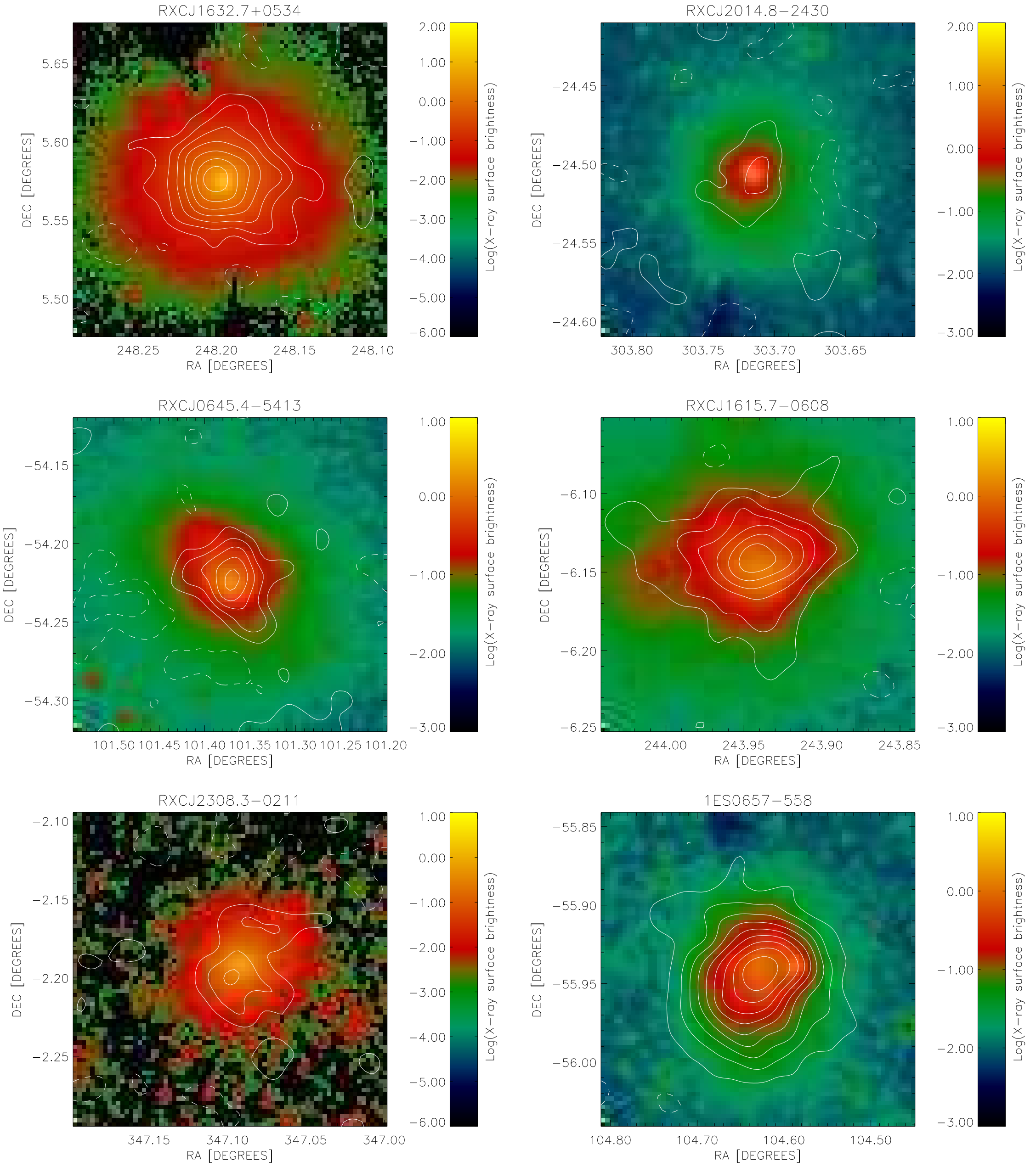

Figure 7.8: X-ray surface brightness (background) and 150 GHz SZ (contours) measurements of each cluster in the sample, excluding clusters for which no XMM data has yet been processed. Contours are multiples of 2σ. Dashed contours indicate positive values. The X-ray maps are in units of $10^{-12}\,\mathrm{erg\,s^{-1}\,cm^{-2}\,arcmin^{-2}}$ and are shown in logarithmic scale to emphasize the extended emission.

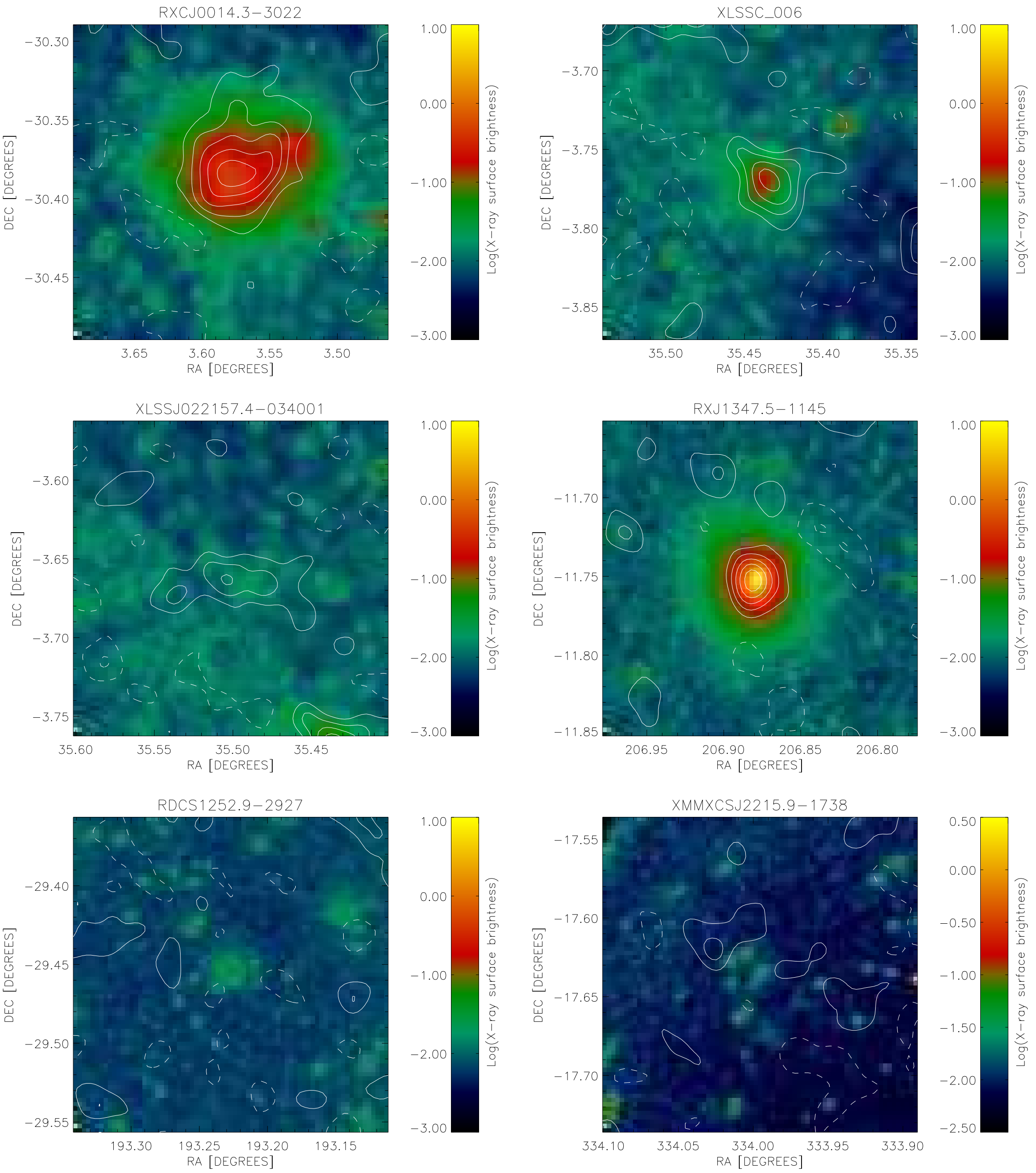

Figure 7.9: Figure 7.8 continued.

Table 7.7: X-ray ICM temperatures and corresponding predicted values of the SZ decrement at 150 GHz, compared to central decrement values measured with APEX-SZ.

Cluster name	kT_e (keV)	T_0 (SZ, measured) (μK$_{\rm CMB}$)	T_0 (SZ, predicted)[a] (μK$_{\rm CMB}$)
RXCJ1632.7+0534	9.1(1)	−542±60	−515
RXCJ2014.8−2430	9.5(2)	−249±99	−560
RXCJ0645.4−5413	–	−543±143	–
RXCJ1615.7−0608	14.8(3)	−758±59	−780
RXCJ2248.7−4431	–	−1242±270	–
RXCJ2308.3−0211	7.9(4)	−215±77	−355
1ES0657−558	13.9(5)	−1015±48	−890
RXCJ0014.3−3022	10.6(6)	−653±130	−565
XLSSC 006	4.8(7)	−205±69	−115
XLSSJ022157.4−034001	–	−108±42	–
RXJ1347.5−1145	12.1(8)	−1035±320	−695
MS1054.5−0321	9.8(3)	< 320	−425
RDCS1252.9−2927	6.0(9)	< 30	−150
XMMXCSJ2215.9−1738	7.4(10)	−151±49	−155

[a] Predictions using the model described in § 3.3.2.

References : (1) Ota & Mitsuda (2004), (2) H. Böhringer (personal communication), (3) LaRoque et al. (2006), (4) Zhang et al. (2006), (5) Govoni et al. (2004), (6) Novicki et al. (2002), (7) Willis et al. 2005, (8) Kotov et al. (2006), (9) Rosati et al. (2004), (10) Stanford et al. (2006).

has passed through the larger one, causing a bow shock with a velocity of several thousand km/s (Markevitch 2006). The direction of collision is perpendicular to the line of sight, yielding a spectacular demonstration of merger dynamics, and hence the cluster has been extensively studied in the X-ray and optical frequencies. Offsets between the peaks in measurements of X-ray surface brightness, tracing baryonic gas, compared to optical lensing measurements, measuring the total gravitational mass, have been suggested as the first direct proof of the existence of collisionless dark matter (Clowe et al. 2006); while the baryonic gas is slowed due to ram pressure, the dark matter components in the two subclusters can pass unhindered through one another.

With the resolution of APEX-SZ, it is not expected that the two subclusters can be resolved, although an elongation consistent with the X-ray measurement is seen is Figure 7.8. Halverson et al. (2008) fit an elliptical β model to the SZ data, yielding results which are consistent with the X-ray data, as is the spherical β model fitted here.

There is no evidence in the APEX-SZ map of contamination from a known bright dust obscured galaxy (Wilson et al. 2008). The source has been detected with LABOCA at 345 GHz (D. Johansson, personal communication), although not with high enough significance to reliably derive a spectral slope in conjunction with the 270 GHz Wilson et al. measurement (considering the small difference in frequency).

7.7.5 RXJ1347.5−1145

Discovered by the *ROSAT* all-sky survey (Schindler et al. 1997), RXJ1347.5−1145 is the most X-ray luminous cluster known. The cluster has a strong cooling flow (Allen 2000), making it very compact with a core radius of merely $11''$. Although the virial radius is expected to be much larger, the present SZ detection is dominated by the unresolved emission from the central part, making it very difficult to reliably fit a model. An alternative analysis is in progress, making use of the iterative mapping algorithm described in § 6.6.3.

The central radio-loud BCG has a well constrained spectrum from 1.4 to 150 GHz (Pointecoteau et al. 2001). A fit to the spectrum of this source yields a flux density of 4.2 ± 0.3 mJy, corresponding to a 100 μK$_{\mathrm{CMB}}$ offset in the SZ decrement. The point source has been removed from the SZ map prior to model fitting (Table 7.5) by subtracting a corresponding beam-convolved source.

7.7.6 MS1054.5−0321

Cooray et al. (1998) report two radio sources in this cluster. One has an unusually steep spectrum in the $1.4 - 30$ GHz range and should be of no concern for the SZ observations at 150 GHz. The spectral slope of the other is unknown, but the low flux density (0.57 mJy) at 30 GHz makes it unlikely to be a concern unless the spectrum is inverted.

7.7.7 XMMXCSJ2215.9−1738

At $z = 1.45$, this is the highest redshift X-ray cluster known to date (Stanford et al. 2006). It is unlikely that the marginal SZ detection is real, since it deviates by almost two arcminutes from the X-ray center (Fig. 7.9).

7.8 Conclusion

The results of several weeks of observing with APEX-SZ has been presented. Out of 13 targeted clusters, 9 have been detected with high significance, two have marginal or doubtful detections, 2 are yet undetected, and one additional, not directly targeted, cluster has a marginal detection. The isothermal β model has been found to describe the SZ emission of all detected clusters well, insofar as the residual maps are consistent with noise. The results of the isothermal modeling are in overall agreement with the results from X-ray observation, although the profiles derived from the present data tend to be somewhat broader.

The automation of APEX-SZ pipeline data reduction has been demonstrated to work well, and a point source transfer function has been used to model both the effects of the instrument beam and losses of cluster signal through the reduction pipeline.

Chapter 8

Cluster Temperature Extraction from Multi-Frequency Sunyaev-Zel'dovich Effect Observations

8.1 Introduction

Multi-frequency observations of the SZ effect can in principle be used to extract three physical quantities of a cluster of galaxies: the electron temperature, T_e, the projected line-of-sight peculiar velocity, v_r, and the central Compton y-parameter, y_0. Measurements at three frequencies should suffice to simultaneously determine all three parameters for a given cluster. However, the degeneracies among the parameters are severe, in particular at low T_e and for receding clusters. Furthermore, systematic effects such as primary CMB anisotropies and galactic dust (chapter 3) introduce additional complications.

Although many reliable observations of the SZ effect have been carried out at a range of frequencies, an accurate determination of a line-of-sight velocity from the SZ effect has yet to be shown.

This short chapter investigates the possibility of constraining peculiar velocities and electron temperatures of hot, compact clusters, utilizing combined measurements at various frequencies, including those of the two bolometer cameras APEX-SZ (150 GHz) and LABOCA (345 GHz) at the APEX telescope.

First, some previous work in this field is summarized. Two different methods of predicting joint constraints are discussed and evaluated. Finally, projected levels of such constraints are presented for a range of observing frequency combinations.

8.2 Previous Work

8.2.1 SZ Observations

Joy et al. (2001) used the interferometer at Owens Valley Radio Observatory (OVRO) and the Berkeley-Illinois-Maryland Association (BIMA) interferometer to perform imaging of three high redshift clusters. Considering only thermal effects, they constrain T_e at around 10 keV (very hot clusters) with uncertainties of a few keV. Only one frequency (28.5 GHz) was used by Joy et al; considerations of hydrostatic equilibrium allows a calculation of the gas mass, thus avoiding the degeneracy with the Compton optical depth. Note that this is only possible when the radial profile of the cluster can be observed. Using similar arguments of hydrostatic equilibrium, LaRoque et al. (2003) derived electron temperatures for an X-ray selected sample of clusters from 30 GHz interferometric observations.

De Petris et al. (2002) measured the SZ effect at four frequencies (14, 214, 272 and 353 GHz) toward the Coma Cluster (A1656). Combining the results with OVRO measurements, the authors were able to estimate the central optical depth to within an uncertainty of 14%.

The most extensive SZ results to date come from the Sunyaev-Zel'dovich Infrared Experiment (SuZIE, SuZIE II). The combined results are presented by Benson et al (2004). From observations at three frequencies (145, 221 and 355 GHz), the central optical depth and radial velocity were fitted for each cluster, assuming X-ray emission-weighted temperatures for T_e. The clusters were modeled with β-profiles, although the analysis shows that the inferred central Comptonization is highly dependent on which intra-cluster gas model is assumed.

8.2.2 Cluster Parameter Extraction Forecasting

First attempts to estimate constraints on T_e from future SZ experiments were made by Pointecouteau et al. (1998) and by Hansen et al. (2002). The degeneracies among the cluster parameters were investigated by Aghanim et al. (2003) and Holder (2004), the latter providing an analysis of the best choice of observing frequencies. The optimal strategy was found to be a combination of data taken in one low frequency (~30 GHz) band, one band around 150 GHz, and one band at a frequency higher than 300 GHz. Using these results, Knox, Holder & Church (2004) found that the simultaneous determination of all three parameters should be possible, given μK sensitivity.

Further work was carried out by Sehgal, Kosowsky & Holder (2005), who applied a change of variables to predict possible constraints on linear combinations of $\tau_e T_e$, $\tau_e T_e^2$ and $\tau_e v_r$.

8.3 SZ Temperature Distortion

From chapter 2, the (thermodynamic) temperature decrement/increment in the CMB due to the *thermal* SZ effect can be written

$$\frac{\Delta T}{T_{\mathrm{CMB}}} = g(x, T_e)\, y, \tag{8.1}$$

where $x \equiv h\nu/k_B T$. For low temperatures, $g(x, T_e) \to g(x) = x \coth(x/2) - 4$ (for a more in-depth discussion see chapter 2). The additional spectral distortion due to a non-zero peculiar velocity with respect to the rest frame of the CMB is

$$\frac{\Delta T}{T_{\mathrm{CMB}}} = -\tau_e \beta, \tag{8.2}$$

where $\beta = v_r/c$ is the radial line-of sight velocity in units of the speed of light, positive for a receding cluster.

8.4 Method

Two different methods are applied to create likelihood contours in the parameter space of T_e, v_r and y_0. The starting point is to assume a fiducial model with a set of true cluster parameters $\{T_e^*, v_r^*, y_0^*\}$, assuming isothermality (so that beam dilution can be easily dealt with) and that v_r is homogeneous (no rotation).

8.4.1 "Quick-and-Dirty" Monte Carlo

In the first approach, a Monte Carlo analysis is carried out with ~10000 realizations of the data from a cluster given the "true" parameters. The data are computed as the theoretical SZ temperature decrements at a number of frequencies and with random Gaussian deviates. For each data set $\{T_1, ...T_n\}$, where T_j is the observed SZ decrement or increment in frequency band j and n is the number of frequencies, the data are fitted to the theoretical SZ model, allowing T_e, v_r and y_0 to reach their best-fit values. In this way, regions of parameter space containing 68% and 95% of the realizations, respectively corresponding to 1σ and 2σ confidence regions, can be mapped out.

8.4.2 The Fisher Matrix Approach

The second method makes use of the Fisher matrix formalism to estimate the *best possible* statistical uncertainties (e.g. Eisenstein, Hu & Tegmark 1999). The Fisher matrix is defined as the ensemble average

$$\mathbf{F}_{ij} = -\left\langle \frac{\partial^2 \ln L}{\partial p_i \partial p_j} \right\rangle_{\mathbf{x}} \tag{8.3}$$

over the observed data $\mathbf{x}$, where p_i is the ith parameter of the model; in this case the model parameters are $\mathbf{p} = \{T_e, v_r, y_0\}$. Writing out the likelihood function, L, explicitly for Gaussian errors and carrying out the ensemble average, one finds (Holder 2004)

$$\mathbf{F}_{ij} = \sum_{\alpha=1}^{n} \frac{1}{\sigma_\alpha} \frac{\partial \Delta \bar{T}}{\partial p_i}(\nu_\alpha, \mathbf{p}) \frac{\partial \Delta \bar{T}}{\partial p_j}(\nu_\alpha, \mathbf{p}), \tag{8.4}$$

where the derivatives are evaluated where $\mathbf{p}$ takes its fiducial values, and $\Delta \bar{T}$ is the model prediction for the SZ decrement in the fiducial model at frequency ν_α.

Gaussian priors on any of the model parameters can easily be applied by adding $1/\sigma_i^2$ to the diagonal element F_{ii} of the Fisher matrix, where σ_i^2 is the variance of the prior on p_i.

The inverse $\{\mathbf{F}\}_{ij}$ of the Fisher matrix is an estimate of the covariance matrix for the fitted parameters. Likelihood contours are constructed as projections of the error ellipsoid, whose principal axes correspond to the eigenvectors of the Fisher matrix evaluated at the fiducial p_i. One disadvantage of this method is that the eigenvectors of $\mathbf{F}_{ij}$ depend (albeit weakly) on how the p_i are scaled. It is common to choose the scaling such that all parameters are weighted equally (Sehgal, Kosowsky & Holder 2005). Here, the parameters are scaled to order unity by dividing through the "characteristic" values $T_e = 8$ keV, $v_r = 500$ km s$^-1$ and $y_0 = 10^{-4}$.

Although the Fisher matrix approach generally leads to likelihood contours that are too optimistic, Figure 8.1 shows that the method gives results comparable to those generated by the somewhat more realistic Monte Carlo approach. The Fisher matrix formalism is thus used for the remainder of the analysis in this chapter, as it is computationally much faster.

As discussed in chapter 2, decoupling T_e from y_0 from SZ observations alone is only possible when the ICM temperture is high enough that the relativistic correction to the SZ effect is

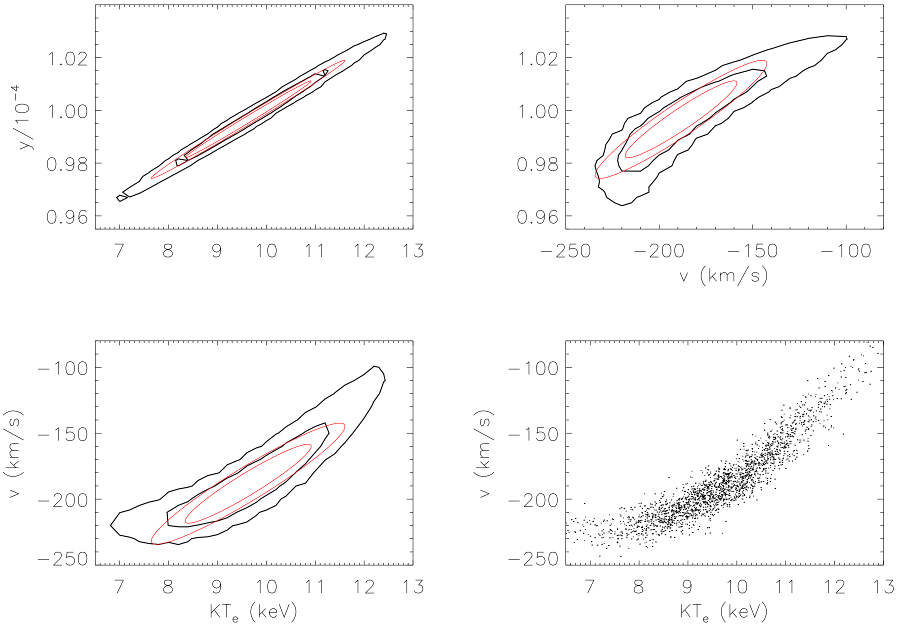

Figure 8.1: 68% and 95% confidence regions on cluster parameters for a hot, massive cluster, from simulated observations at five frequencies (90, 150, 217, 250 and 345 GHz) assuming 10 μK random uncertainties in each frequency band. Thick (black) contours are from a Monte Carlo analysis, while thin (red) contours have been computed using the Fisher matrix formalism. *Bottom right:* scatter plot of best-fit models for a fraction of the Monte Carlo realizations.

measurable. For this reason, only hot clusters in the range $8 - 15$ keV are considered. It will be investigated how errors in v_r and T_e depend on the various parameters, the combination and number of frequencies, and the detector noise level.

Two frequency setups are considered; $\{30, 150, 300 \text{ GHz}\}$ (henceforth referred to as setup I) and $\{90, 150, 217, 250, 345 \text{ GHz}\}$ (setup II). Setup I has been discussed by Holder (2004) and verified by Sehgal et al. (2005) to be the optimal choice of three frequencies for recovering the input model. The central Comptonization y_0 is set to 10^{-4}.

8.5 Results

Figures 8.2 and 8.3 indicate how the uncertainties in v_r and T_e depend on the input values of these parameters themselves. It is assumed that the sensitivity of the fiducial SZ measurements is 10 mK$_{\text{CMB}}$ at each frequency (cf. chapters 3 and 7). An important result is that while the radial velocity uncertainty is highly dependent on both T_e and v_r, the uncertainty in temperature is independent of v_r. For both frequency setups considered, the "optimal cluster" for constraining v_r has a high electron temperature and a negative peculiar velocity (i.e. an approaching cluster) of a few hundred km/s.

Although setup II has five frequencies, the setup including the low (30 GHz) frequency

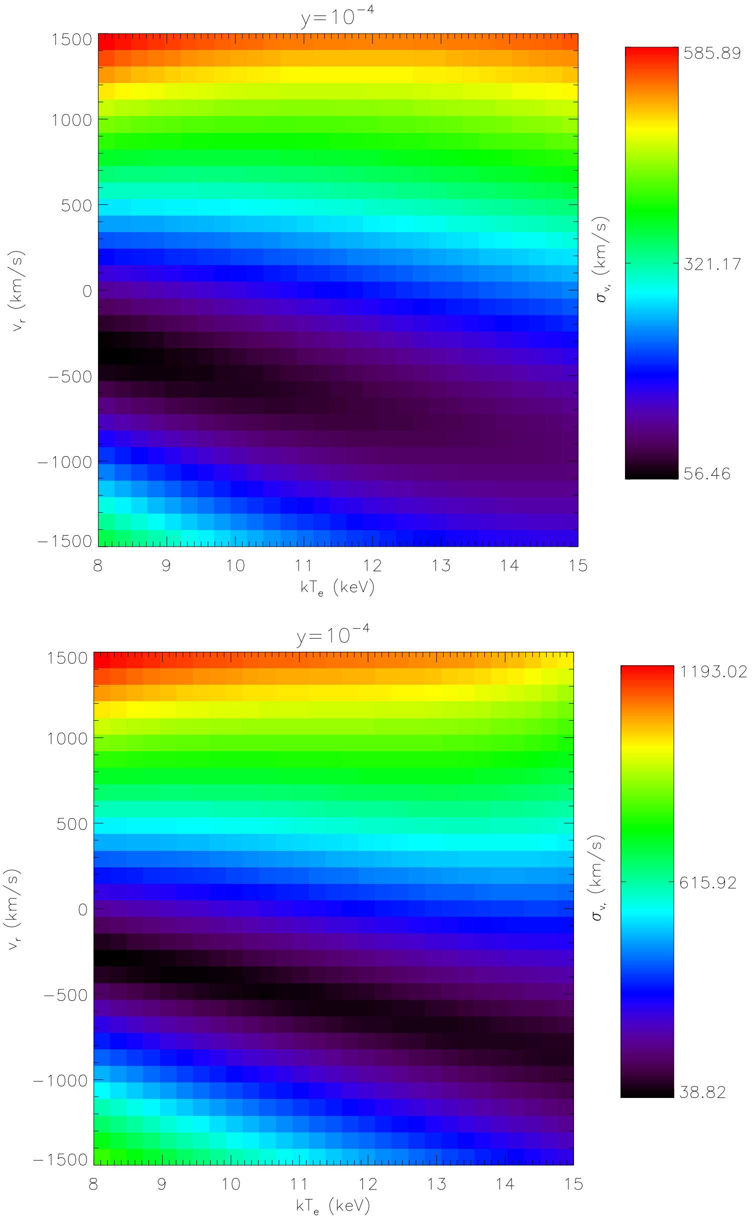

Figure 8.2: Estimated 1σ errors in v_r as a function of cluster parameters for two different frequency setups with a constant $y = 10^{-4}$: $\{30, 150, 300$ GHz $\}$ (setup I, *top*) and $\{90, 150, 217, 250, 345$ GHz $\}$ (setup II, *bottom*).

does better in recovering both T_e and v_r. In particular, the errors on T_e are about twice as large for setup II as for setup I. As pointed out by Holder (2004), measurements at the null point of the thermal SZ effect (∼217 GHZ, see § 2.2.3) are not well suited for determining cluster parameters. Indeed, removing this frequency from setup II has little effect on the results. Adding a frequency at or below 30 GHz to setup II greatly improves the constraints, but makes them only marginally better than with setup I.

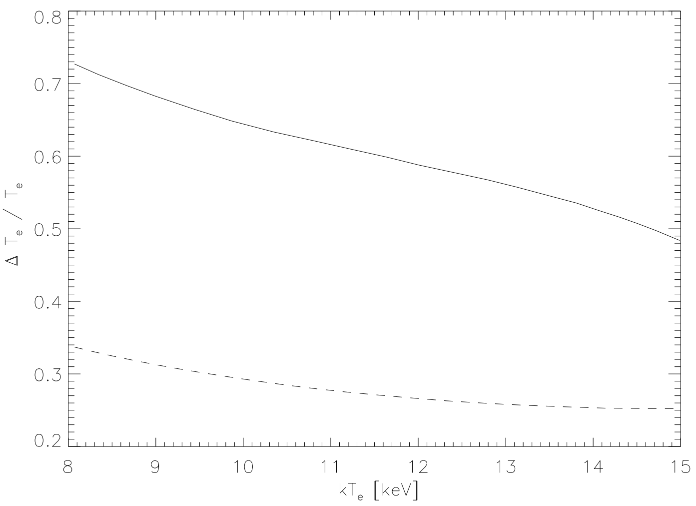

Figure 8.3: Estimated 1σ relative uncertainties in T_e as a function of T_e (independent of v_r) for $y_0 = 10^{-4}$ with frequency setups I (dashed line) and II (solid line)
.

Thus far the influence of the Compton parameter has not been considered. Since the thermal SZ spectrum scales linearly with y, the relative uncertainties in the data will also scale linearly with this parameter. This induces errors in the estimated parameters, roughly scaling as the inverse of y. It is thus important to note that the absolute uncertainties in T_e and v_r described in this section must be related to the value of $y_0 = 10^{-4}$.

The relative uncertainties $\Delta T_e/T_e$ and $\Delta v_r/v_r$ are both found to scale linearly with the detector noise level, as is shown in Figure 8.4. Figure 8.5 shows the estimated 68% and 95% confidence contours in the $T_e - v_r$ parameter subspace for setups I and II, as well as for two additional setups.

8.6 Conclusion

Although the simultaneous temperature and velocity derivation from multi-frequency SZ data is in principle possible, the leverage of current data on the problem is poor. Most individual current measurements are still limited by statisical errors (chapters 7 and 9), nevertheless systematic effects pose fundamental limits on the accuracy with which an ICM temperature measurement can be made. In particular, the sub-mm background limits the effective signal-to-noise level that can be reached for freqeuencies above 100 GHz, and at lower frequencies radio point sources are a problem (chapter 3). Furthermore, current uncertainties in the absolute calibration of mm and sub-mm data (cf. chapter 7) severely complicates any simulatenous extraction of T_e and v_r for any cluster of galaxies.

Realistically, SZ data must to be combined with data from other wavelengths to yield meaningful constrains. In the next chapter, SZ data from APEX-SZ is combined with X-ray data to yield separate constraints on temperature and density.

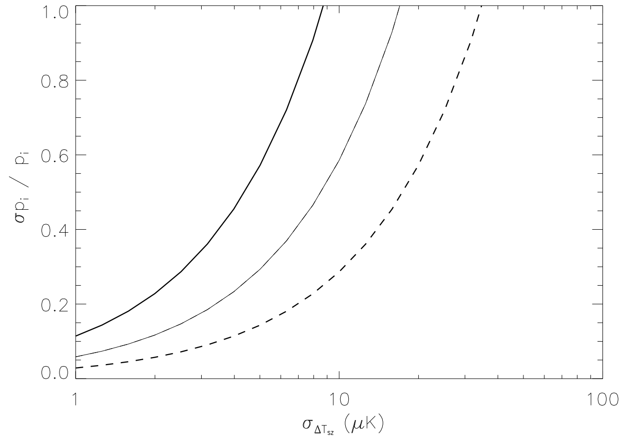

Figure 8.4: Uncertainties in cluster parameters p_i as a function of detector noise (setup II). The thin curve shows $p_i = T_e$, and the two thick curves $p_i = v_r$, of which the solid curve represents a "true" cluster velocity of 500 km/s and the dashed curve is for $v_r = 100$ km/s. The input Compton parameter and the ICM temperature are $y_0 = 10^{-4}$ and $T_e = 10$ keV.

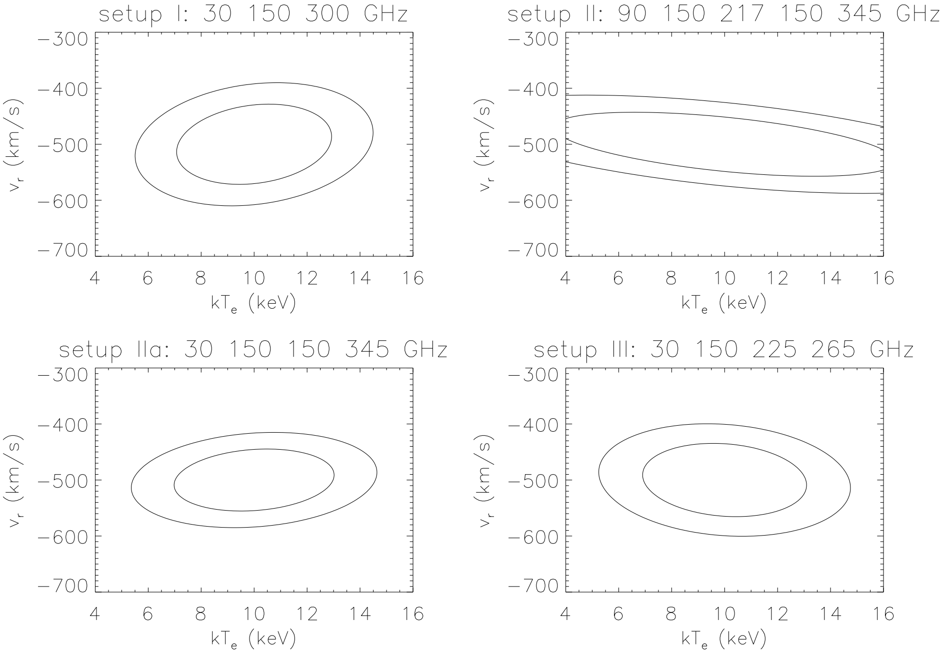

Figure 8.5: Estimated confidence regions in T_e and v_r for a number of different frequency setups, assuming an uncertainty of 10 $\mathrm{mK_{CMB}}$ at all frequencies. As previously, $y_0 = 10^{-4}$.

Chapter 9

Multi-Frequency Observations of Abell 2163

9.1 Introduction

With sufficiently high resolution, the SZ effect can be used to map the pressure structure of individual clusters; once combined with information on the X-ray surface brightness, the SZ provides constraints on gas temperatures and total mass distributions inside clusters. Such constraints are free from the potential biases of X-ray spectroscopy. A further comparison with weak-lensing maps yields insight into the dynamical state of the cluster by checking the validity of the hydrostatic equilibrium condition. Joint de-projection methods using X-ray and SZ maps have been widely discussed (e.g. Lee & Suto 2004, Puchwein & Bartelmann 2006), but so far their implementation using real SZ data has been limited to unresolved or barely resolved SZ maps (e.g. De Filippis et al. 2005) or have been limited by parametric models (Kitayama et al. 2004, Yuan et al. 2008). A main objective of this chapter is to show the potential of non-parametric de-projection analysis using high signal-to-noise resolved SZ maps in conjunction with X-ray data.

Abell 2163 (henceforth A2163) is a hot, X-ray luminous galaxy cluster at $z = 0.203$, with a mean X-ray temperature in the central region of $T_{\mathrm{X}} = 12^{+1.3}_{-1.1}$ keV (Markevitch & Vikhlinin 2001). It has a relatively large angular extent, with a virial radius estimated from weak-lensing mass modeling to be on the order of 15 arcminutes (Radovich et al. 2008), making primary CMB anisotropies a major source of systematic uncertainty in the SZ measurements. Detailed X-ray observations suggest that A2163 is a merger system (Elbaz et al. 1995, Govoni et al. 2004), with asymmetric X-ray temperature structures and strong radio halos. The merger scenario is also supported by optical observations, most notably from the presence of two bright cD galaxies (BCG; Maurogordato et al. 2008). The cluster has been observed in the SZ at 30 GHz with OVRO/BIMA (Reese et al. 2002), and at 142, 217, and 268 GHz using SuZIE (Holzapfel et al. 1997a,b). During the commissioning observation of the APEX-SZ camera in 2007, A2163 was detected with high significance ($\sim 12\sigma$) at 150 GHz with arcminute resolution. The cluster was observed in the SZ increment at 345 GHz using the LABOCA bolometer camera (chapter 5) on APEX, providing images with an angular resolution of $19.5''$.

With a map larger than $12'$ across, the present LABOCA data on A2163 provide the first large-area imaging of a galaxy cluster at sub-mm wavelengths. High-resolution SZ increment imaging is important in view of planned future observations of clusters at sub-mm wavelengths, and for controlling potential foregrounds. However, due to limitations in constraining the SZ emission at large radii, the use of the sub-mm data in this study is limited to the application of the multi-frequency SZ measurement to model the SZ spectrum and derive constraints on the thermal and kinematic SZ components.

In sections 9.2 and 9.3, the observations and data reduction algorithms used to obtain maps at 150 and 345 GHz are described. In section 9.4, a simple isothermal model of the cluster gas density distribution, similar to the analysis of chapter 7, is presented. A non-parametric joint SZ/X-ray de-projection of the cluster temperature and density structure is performed in section 9.5. Finally, all available SZ observations of A2163 are incorporated in section 9.6 to derive the best-fit line-of-sight peculiar velocity and central Comptonization from the SZ spectrum. A summary of the results is given in section 9.7.

Note that this chapter relates the same results that are presented by Nord et al. (2009), and is very similar to the latter in its content.

9.2 Observations

9.2.1 APEX-SZ Observations at 150 GHz

Observations of A2163 at 150 GHz were carried out in April 2007 with the APEX-SZ camera. At the time of observation, 280 of the 330 bolometers were read out, and of these about 160 were used for the map making after applying a noise cutoff (cf. chapter 5).

To obtain a uniform coverage over the extended emission of the cluster, horizontal raster scans were made with a $15' \times 15'$ scan pattern, tracking the central cluster position. The median scan speed was $230''\,\mathrm{s}^{-1}$, and the total integration time was 7.6 hours. The observing conditions were good to moderate for the site, with 150 GHz zenith opacities in the range 0.04-0.09.

0.7 hours of additional observations were carried out in August 2007, in drift circle mode (see chapters 6 and 7), scanning in circles of radius 6 arcseconds.

9.2.2 LABOCA Observations at 345 GHz

After producing a high signal-to-noise detection with APEX-SZ, five hours of follow-up observations at 345 GHz with LABOCA were completed in September 2007. Seven further hours of observations at this frequency were carried out in May 2008.

At the time of observation, LABOCA had 268 optically active bolometer channels, of which around 240 were used for mapping of A2163. The observing conditions were stable in both observing periods, with a typical atmospheric zenith opacity of 0.2-0.3 at the observing frequency. A2163 was observed in an elevation range of 40-70 degrees.

For the LABOCA observations, a spiral pattern was used with inner and outer radii of 120 and 180 arcseconds, respectively (cf. § 5.3.3). Each scan was made up of four such spirals, separated by 140 arcseconds in azimuth and elevation, to make the coverage close to constant over the central part of the cluster.

9.2.3 X-ray Data

To determine the X-ray brightness distribution of A2163, archival XMM data of A2163 from August 2000 are used. Due to the large size of the target, as compared to the XMM field of view, a mosaic of five pointings was required to fully cover the cluster: one "on-source" pointing[1] and four offset pointings[2] to probe the outskirts of the cluster and the surrounding cosmic background. The nominal exposure time of each observation was about 30ks.

9.3 Data Reduction and Mapping

A reduction of the APEX-SZ data of A2163 has already been described in chapter 7. However, as this generic reduction was common to all cluster fields, a reduction more specialized for the purposes of this chapter is described here. In addition, the reduction of the LABOCA 345 GHz data of A2163 is described in this section. The calibration of the data at both frequencies is described in chapter 5. The reduction of the XMM-Newton X-ray data is described in Nord et al. (2009).

9.3.1 General Sky Noise Considerations

The SZ signal from Abell 2163 is extended over more than 20 arcminutes, which is comparable to the field-of-view of APEX-SZ ($23'$ across) as well as that of LABOCA ($11.4'$ across). This makes the subtraction of atmospheric noise very difficult; subtracting common-mode signals across the array and applying polynomial baselines (corresponding to large-scale Fourier modes) in this case has the side effect of also removing astronomical signals on scales comparable to the field-of-view of the array, as discussed in chapter 6.

In general, the APEX-SZ observations were carried out in poorer observing conditions than the LABOCA observations, with relatively high levels of precipitable water vapor. For this reason, the APEX-SZ data suffers from excess low-frequency noise correlated on scales much smaller than the array (cf. § 5.2.4), requiring high-pass filtering of individual bolometer time streams to be applied after removing the correlated atmospheric signal. While this step enhances the signal-to-noise ratio of the detection, it also removes additional astrophysical signal. To account for this, the point source transfer function, as described in § 6.5, is used in two ways: (i) for the isothermal analysis the parameterized cluster model is convolved with the transfer function for comparison with the reduced map; and (ii) for the non-parametric non-isothermal analysis, the reduced map is de-convolved with the transfer function, as described in § 6.6.4.

In spite of the higher frequency band, there is no excessive low-frequency atmospheric noise component in the time streams of the LABOCA data. However, because of the lower sensitivity of this instrument with respect to the SZ signal, a smaller scan pattern was used, compared to the APEX-SZ observations, to maximize the signal-to-noise ratio in the limited time available. The small scan pattern fundamentally limits the scale on which the SZ emission can be recovered. In addition, the details of the LABOCA data reduction limits the use of a transfer function since the latter cannot be constructed to be linear in the sense discussed in § 6.5; in other words, the reduction pipeline acts differently on a point source and an extended source. To recover as much of the SZ increment signal as possible, the iterative map-making algorithm discussed in § 6.6.3 is used.

9.3.2 APEX-SZ Data Reduction

The APEX-SZ reduction is slightly different for raster scans and circular drift scans, but identical for each scan within these two subsets.

---

[1] Observation Id: 0112230601

[2] ObsId: 0112230701, 0112230801, 0112230901, 0112231001

After flagging detectors with low optical response, correlated (atmospheric and electronic) noise is removed by subtracting the median signal from across the good channels of the array at each time sample (§ 6.2.2). Individual time streams are then despiked by flagging and removing data that deviates from the baseline by more than 5σ, which typically corresponds to less than 0.1% of the data. Electronic glitches are recognizable because they occur with durations shorter than the detector response time. These features, seen only in a negligible amount of data, are removed as well.

To baseline the data of a raster scan, the scan is divided into subscans of constant elevation, resulting in subscans extending over $30'$ in azimuth. Turnarounds in the scan pattern, where the scan speed is significantly lower, are flagged and removed. A fifth order polynomial is fitted to and subtracted from each constant-elevation subscan, effectively high-pass filtering the time streams.

Circular drift scans are baselined by defining subscans consisting of 2.5 full circles and applying a fifth order polynomial, after flagging the first full circle of the scan (which usually contains intervals of high scan acceleration). This polynomial baseline corresponds to a spatial filter similar to that applied to the raster scans. Simultaneously, an airmass correction is applied as described in § 7.2.

For each scan, a map with $10'' \times 10''$ pixels is constructed, weighting the data by the inverse rms of each reduced time stream. All maps are then co-added. In parallel with the reduction of the data, a beam-shaped source, without noise and translated into time stream data, is passed through an identical pipeline to obtain the point source transfer function (§ 6.4). All flags and weights on the data are carried over to the artificial data.

The resulting transfer function is used to deconvolve the high significance co-added map of Abell 2163 to the intrinsic resolution of the instrument, using the algorithm described in § 6.6.4. The de-convolved APEX-SZ map of Abell 2163 is shown in Figure 9.1.

To compute the noise on the beam scale, the final map is smoothed with the APEX-SZ beam, and the rms is estimated by taking the standard deviation in square regions with side five times the beam FWHM. In this way, a noise rms value of 32 $\mu\mathrm{K}_{\mathrm{CMB}}$ on the beam scale is found, corresponding to 0.013 MJy sr^{-1}, in the central region of the de-convolved map.

9.3.3 LABOCA Data Reduction

Because the LABOCA time streams are more stable at low frequencies than those from APEX-SZ, the data do not have to be further filtered after standard correlated-noise removal. Aside from this difference, the time stream reduction sequence used in each iteration is quite similar to that used for the APEX-SZ data, and basically follows the method outlined by Weiss et al. (2008) and detailed by Siringo et al. (2009). Maps are constructed with $6'' \times 6''$ pixels, and co-added in the same way as for the APEX-SZ data.

To account for sky signal attenuation in the time stream reduction, the the iterative approach described in § 6.6.3 is followed. Eight iterations are required before convergence is reached. In each iteration, an identical time series reduction is performed.

Because the iterative mapping technique is non-linear, it is not straightforward to characterize it by a filter function. In place of a transfer function, the instrument beam is used when fitting a model to the 345 GHz data. Significant loss of signal is expected using the iterative approach. To quantify the level of bias, the best-fit β model from the APEX-SZ measurement (§ 9.4) is passed through the complete LABOCA data reduction pipeline. Although more than 30% of the signal is lost beyond r_{500} (the radius at which the enclosed average matter overdensity is 500 times the density of the cosmic background), the signal loss within r_{2500} (defined analogously) is negligible in comparison with statistical errors. The central rms in

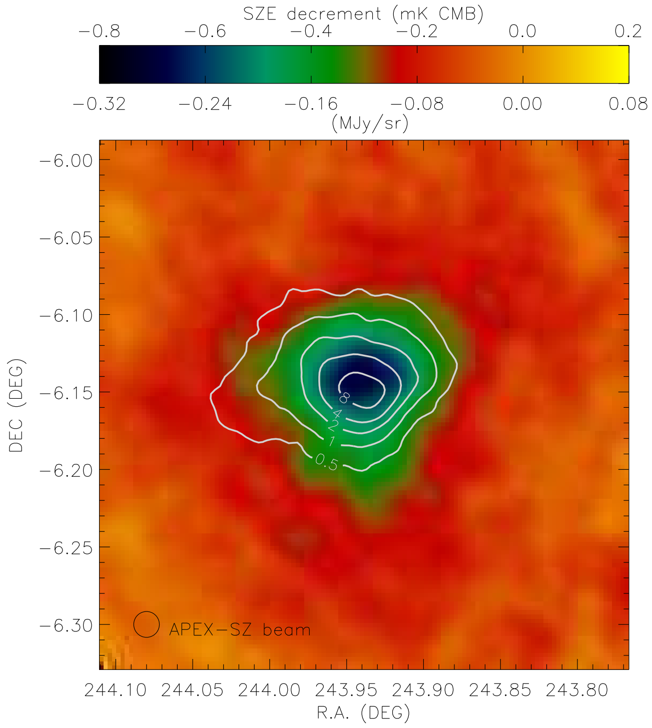

Figure 9.1: Map of Abell 2163 at 150 GHz, overlaid with XMM-Newton X-ray contours. in units of $10^{-13}\,\mathrm{erg\,s^{-1}\,cm^{-2}\,arcmin^{-2}}$. Because the correlated-noise removal has attenuated the source signal, the map has been de-convolved using the point source transfer function (see text).

the LABOCA map, computed on a scale of five times the LABOCA FWHM (19.5″), is 1.9 mJy/beam, corresponding to 0.24 MJy sr^{-1}.

One significant point source is found in the final map (Fig. 9.2), likely thermal emission from a cluster galaxy or a background source lensed by the cluster. After high-pass filtering the map to remove structures larger than two beams (such as the cluster emission), a peak flux density of 11.8 ± 1.9 mJy/beam is found for this source.

9.4 Isothermal Modeling of the Intra-Cluster Gas

9.4.1 Elliptical β model fit to the SZ data

In order to assess the SZ measurements quantitatively and compare them with the X-ray data, the well-known isothermal β model (§ 2.2.4) is used, as in chapter 7. Because of the significant ellipticity in the X-ray surface brightness profile, Eqn. (2.18) is generalized to an elliptical form given by (e.g. Halverson et al. 2008)

$$\Delta T_{\mathrm{SZ}} = \Delta T_0 \left(1 + A + B\right)^{(1-3\beta)/2}, \tag{9.1}$$

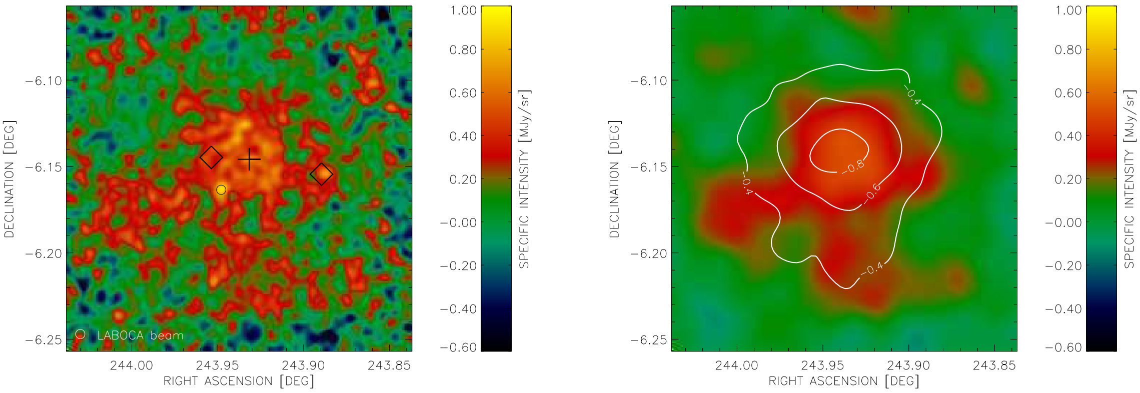

Figure 9.2: *Left:* Final 345 GHz LABOCA map of Abell 2163, smoothed with the 19.5″ beam. The cross marks the position of a bright flat-spectrum radio source (Cooray et al. 1998). The diamonds mark the positions of two BCG (Maurogordato et al. 2008). The circle marks the position of the bright point source found in the present data. *Right:* LABOCA map smoothed to the APEX-SZ resolution of 1 arcminute. The bright point source described in the text has been removed. The APEX-SZ 150 GHz map is shown as contours.

where

$$A = \frac{(\cos(\Phi)(X - X_0) + \sin(\Phi)(Y - Y_0))^2}{\theta_{\rm c}^2},$$

$$B = \frac{(-\sin(\Phi)(X - X_0) + \cos(\Phi)(Y - Y_0))^2}{(\eta\theta_{\rm c})^2}.$$

Here $(X - X_0)$ and $(Y - Y_0)$ are angular offsets on the sky in the right ascension (RA) and declination (DEC) directions, respectively, with respect to the centroid position (X_0, Y_0). The axial ratio, η, is the ratio between the minor and major axis core radii and Φ is the angle between the major axis and the RA (X) direction.

An elliptical β profile is fitted to the 150 GHz data by convolving each model function with the point source transfer function and minimizing a χ^2 statistic weighted by the inverse square of the local map rms. Note that the raw, not the de-convolved, map is used for this fit in conjunction with the transfer function. All map pixels within a $10'$ radius of the X-ray center (§ 9.4.2) are considered for the fit. The results of the fit are given in Table 9.1.

For comparison, a spherical β profile is also fitted, with roughly consistent results. At 345 GHz, the detection of Abell 2163 is less significant. For this reason, the centroid position and the value of β are kept fixed at the values found in the 150 GHz fit.

Errors in the fitted profiles are estimated using a Monte Carlo approach. The map data is bootstrapped (cf. § 6.5.3) by inverting the sign of half the individual scan maps (randomly chosen), and the maps are co-added to generate a pure noise map. After convolving the best-fit model with the transfer function and adding the result to the noise map, the χ^2 statistic is again minimized to find the best set of parameters for the new map. The entire procedure is repeated 1000 times, upon which the errors in the respective parameters are taken as the scatter in the distributions of their fitted values. It is verified that the mean of the distributions of fitted parameters are consistent with the best-fit model.

9.4.2 Elliptical β-model fit to the X-ray data

To allow for a basic comparison of the SZ and X-ray data in the context of the isothermal β model, an isothermal fit to the X-ray data, similar to that used for the SZ data, is also performed. As for the SZ analysis, the spherical β model is generalized to an elliptical form, as

$$\Delta S_{\mathrm{X}} = \Delta S_0 \left(1 + A + B\right)^{1/2-3\beta} . \tag{9.2}$$

This model is fitted to the raw X-ray images using the Cash statistic (Cash 1979). The Poisson nature of the data does not allow for a direct background subtraction; instead a simple two-component background model (described in Nord et al. 2009) is added to the fitted components. The results of the fit are presented in Table 9.1.

9.4.3 Systematic uncertainties

Galactic dust

The effect of galactic dust emission on the SZ measurement of Abell 2163 has been estimated by Lamarre et al. (1998) for the PRONAOS balloon experiment and by LaRoque et al. (2002) for the SuZIE experiment (Holzapfel et al. (1997a,b)). However, because these two estimates apply to scan strategies and spatial filtering functions very different from ours, it is not appropriate to extrapolate from either of them. Instead the approach of § 7.5.2 is taken, and corrections of -0.6% to the SZ decrement at 150 GHz and -1.8% to the SZ increment at 345 GHz are found. Note that the corrections are substantially smaller than the 5% absolute calibration uncertainty. Effects on the other fitted parameters are negligible. It is assumed that contamination on angular scales smaller than four arcminutes (i.e. not resolved by IRAS) are also negligible.

Point source contamination

After subtracting a preliminary (possibly point source contaminated) β model from each of the SZ maps, the maps are smoothed to the respective beam scales and searched for point source detections above 3σ. One source (cf. Fig. 9.2) is found in the LABOCA map at 345 GHz. No sources are found in the APEX-SZ 150 GHz map. Any point source detected with sufficient S/N in either map can in principle be removed by subtracting a fitted Gaussian. Here a somewhat more conservative approach is taken; a region with a $1'$ radius around the 345 GHz point source is simply disregarded in a subsequent fit with a new β model.

As already stated in § 7.5, effects of lensing only becomes important when faint sources are raised above the detection limit and removed. It is not clear whether the bright point source found in the 345 GHz map is a lensed background source; however, it is verified that the effect in the central SZ increment of excluding the region around this source for the fit is no more than 4%, i.e. smaller than both the derived statistical errors and the absolute calibration uncertainty.

Radio sources are expected to correlate strongly with clusters of galaxies (e.g. Reddy & Yun 2004). The NVSS catalog (Condon et al. 1998) has been searched for sources brighter than 5 mJy at 1.4 GHz. The flux of each source is extrapolated to 150 GHz using the spectral index maps of Feretti et al. (2004). With this simple approach, even the brightest source has an estimated peak flux density considerably lower than the rms in the APEX-SZ map. Cooray et al. (1998) report an inverted-spectrum non-thermal source of 3 mJy at 30 GHz, indicated in Figure 9.2. No counterpart can be seen in either SZ map. High-pass filtering the APEX-SZ map, after subtracting the best-fit model of the cluster, to remove all structure larger than $3'$ results in an effective rms of 30 $\mu\mathrm{K_{CMB}}$ at the position of this source. The fact that the source is not seen in this filtered map allows to set a lower limit on the spectral index as $\alpha_{30}^{150} \gtrsim 0.5$ ($S_\nu \propto \nu^{-\alpha}$). Subtracting the corresponding signal from the APEX-SZ map before the β model fit results in a systematic shift in the central SZ decrement of less than 1%. Based on these considerations, systematic effects from radio sources are considered negligible in comparison with primary CMB anisotropies and absolute calibration.

Primary CMB contamination

The effects of primary CMB contamination are estimated by generating 100 realizations of the CMB sky in a one square degree field with a resolution of $1.7'$ as in § 7.5.1.

Each primary-CMB map is re-sampled as time streams corresponding to a typical scan of the SZ observations at the two frequencies and run through the reduction pipelines to account for filtering. The β model fit is repeated after adding each of the thus filtered primary-CMB realizations. The scatter in the results of each parameter is taken as the 68% systematic marginal error from primary CMB contamination. The fractional errors are 3.4% at 150 GHz and 2.9% at 345 GHz.

9.4.4 Results of the isothermal modeling

Figure 9.3 shows the radial profile of the best-fit spherical β profile to the 150 GHz data and the same profile convolved with the transfer function, as well as the profiles of the raw and de-convolved maps. The best-fit β model parameters, corrected for systematic effects as described above, are given in Table 9.1. The radial profile of the de-convolved map, not used for any fitting, is consistent with the beam-smoothed best-fit model within the $10'$ truncation radius used for the fit.

Comparing the results of the X-ray and SZ fits, a significant offset ($27 \pm 9''$), possibly caused by an asymmetric temperature distribution near the center, appears between the two centroid position. The other fitted parameters show an overall consistency as to the global shape of the emission. Note that in spite of the significant ellipticity in the X-ray surface brightness, the elliptical model of the SZ emission is only barely inconsistent with the spherical one (the axial ratio deviates from 1 by only 1.7σ). The most likely explanation for this is the poorer resolution of the SZ data which results in a larger uncertainty on the ellipticity.

9.5 Non-Isothermal Modeling of the Intra-Cluster Gas

Several authors have discussed the joint modeling of SZ and X-ray data for de-projecting ICM parameters (see, e.g., Yoshikawa & Suto 1999, Zaroubi et al. 2001, Puchwein & Bartelmann 2007, Ameglio et al. 2007). However, most of these analyses have been limited to analytic (parameterized) cluster models (e.g. Kitayama et al. 2004) or numerical simulations. This is the first attempt at a non-parametric de-projection of cluster density and temperature profiles using actual SZ image data (rather than fitted profiles) in combination with X-ray data.

Given the large angular size of Abell 2163, the arcminute resolution of APEX-SZ is sufficient to carry out a joint radial density and temperature modeling of the ICM in combination with the XMM-Newton X-ray data. Although the LABOCA map has more than a factor of two

Table 9.1: β model fit results. For the fit at 345 GHz, the centroid position and β have been fixed to the results of the 150 GHz measurement. Parentheses indicate that parameters were fixed for the fit.

Parameter	150 GHz (elliptical)	150 GHz (spherical)
X_0 (Central R.A. [J2000])	$16^{\mathrm{h}}15^{\mathrm{m}}45.1^{\mathrm{s}}\pm9''$	$16^{\mathrm{h}}15^{\mathrm{m}}45.6^{\mathrm{s}}\pm8''$
Y_0 (Central DEC. [J2000])	$-06^\circ08'31''\pm8''$	$-06^\circ08'28''\pm8''$
Peak signal[a]	-0.317 ± 0.035	-0.318 ± 0.035
θ_c (core radius)	$85\pm18''$	$98\pm21''$
β (power-law index)	0.69 ± 0.14	0.70 ± 0.14
Φ (inclination angle)	$133\pm22^\circ$	(0.0)
η (axial ratio)	0.80 ± 0.12	(1.0)

Parameter	345 GHz (spherical)	X-ray (elliptical)
X_0 (Central R.A. [J2000])	$(16^{\mathrm{h}}15^{\mathrm{m}}45.6^{\mathrm{s}})$	$16^{\mathrm{h}}15^{\mathrm{m}}46.6^{\mathrm{s}}\pm1.5''$
Y_0 (Central DEC. [J2000])	$(-06^\circ08'28'')$	$-06^\circ08'44.1''\pm1.4''$
Peak signal[a]	0.633 ± 0.094	$1.075\times10^{-12}\pm7\times10^{-15}$
θ_c (core radius)	$65\pm26''$	$90.7\pm2.8''$
β (power-law index)	(0.70)	0.639 ± 0.03
Φ (inclination angle)	(0.0)	$1.2\pm6^\circ$
η (axial ratio)	(1.0)	0.850 ± 0.05

[a] For the SZ measurements, the peak signal is the brightness ΔB_ν in units of MJy sr^{-1}; for the X-ray measurement, brightness is in units of erg s^{-1} cm^{-2} arcmin^{-2}.

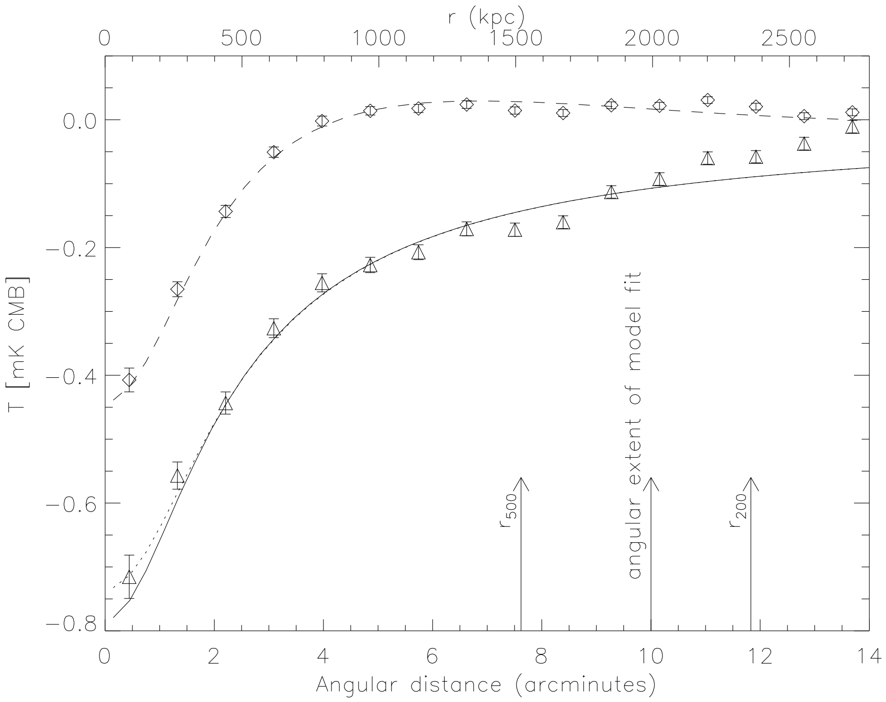

Figure 9.3: Radial SZ profile of Abell 2163 at 150 GHz. Diamonds indicate the profile computed from the reduction-attenuated raw map (before deconvolution; this is the map used for the parametric fit) while triangles represent the profile from the map deconvolved to the beam resolution (note that this map is *not* used for any parametric model fitting). The solid line shows the profile of the best-fit isothermal β model, fitted to the raw map using the transfer function to convolve the model. The dotted line is the profile of the same best-fit β model convolved with the APEX-SZ *beam*, while the dashed line is that profile convolved with the *transfer function.* The vertical arrows indicates the radial cut of $10'$ used for the model fit, as well as r_{200} and r_{500}.

better resolution, due to its high noise level and small field of view the analysis in this section is restricted to the APEX-SZ data.

9.5.1 Method

De-projection Method

The non-parametric de-projection analysis employs a direct inversion technique based on the Abel integral. This technique was first proposed by Silk & White (1978; see also Yoshikawa & Suto 1999). Apart from the assumption of spherical symmetry, there are no additional theoretical constraints (e.g. hydrostatic equilibrium or a polytropic gas index), making this is a natural method for extracting ICM parameters, assuming that spherical symmetry indeed provides a good estimate of the structure. X-ray spectroscopic measurements have shown that Abell 2163 has a complicated temperature structure at the center and is most likely a merging system (Elbaz et al. 1995, Govoni et al. 2004). Nevertheless, the de-projection analysis with spherical symmetry implemented here shows how resolved SZ images of clusters can immediately be used in combination with X-ray data to gain a better understanding of the gas and mass distributions.

The SZ temperature decrement can be written as the integral over the line of sight;

$$\Delta T(R) = 2A_{\rm SZ} \int_R^\infty g(x, T_e)\; n_e(r)\; T_e(r)\; \frac{r{\rm d}r}{\sqrt{r^2 - R^2}} \tag{9.3}$$

where the cluster is assumed to be spherically symmetric, $A_{\rm SZ} = T_{\rm CMB}\ (k\sigma_{\rm T}/m_e c^2)$, r is the physical radius from the cluster center, $R = D_A\theta$ (where θ is the projected angular distance on the sky and D_A is the angular diameter distance; to calculate D_A the cosmology of Komatsu et al. 2008 is assumed). $T_e(r)$ and $n_e(r)$ are the electron gas temperature and density radial profiles. The small T_e dependence in $g(x, T_e)$ is neglected for this analysis ($\sim 5\%$ at 150 GHz) and $g(x, T_e{=}10\ {\rm keV})$ is incorporated into the factor $A_{\rm SZ}$.

The X-ray surface brightness profile can be written as (Yoshikawa & Suto 1999)

$$S_{\rm X}(R) = \frac{2A_{\rm X}}{(1+z)^4} \int_R^\infty n_e^2(r)\; \Lambda_H(T_e(r))\; \frac{r{\rm d}r}{\sqrt{r^2 - R^2}}. \tag{9.4}$$

The APEC code (Smith et al. 2001) is used to compute the cooling function for Abell 2163 assuming an abundance value of $0.5Z_\odot$. In the [0.5-2] keV XMM band used in this analysis, the temperature dependence of the cooling function can be approximated as $\Lambda_H(T_e(r)) \propto T_e(r)^{-1/6}$ (see Ettori 2000), assuming the bulk of the cluster gas has a temperature in the range 2-16 keV. The normalization of the power law approximation is absorbed into the coefficient $A_{\rm X}$.

Using Abel's integral equation, equations (9.3) and (9.4) can be inverted to obtain joint radial density and temperature profiles as

$$T_e(r)\; n_e(r) = \frac{1}{\pi A_{\rm SZ}} \int_\infty^r \frac{{\rm d}\Delta T(R)}{{\rm d}R}\; \frac{{\rm d}R}{\sqrt{R^2 - r^2}}; \tag{9.5}$$

$$T_e^{-1/6}(r)\; n_e^2(r) \; = \frac{(1+z)^4}{\pi A_{\rm X}} \int_\infty^r \frac{{\rm d}S_{\rm X}(R)}{{\rm d}R}\; \frac{{\rm d}R}{\sqrt{R^2 - r^2}}. \tag{9.6}$$

Following Yoshikawa & Suto (1999), equations (9.5) and (9.6) are integrated numerically by summing in radial bins from $i_{\rm min}$ to $i_{\rm max}$, where $i_{\rm max}$ is the index for the outermost bin, and $i_{\rm min}$ corresponds to r/D_A. Uncertainties in the derived density and temperature profiles are propagated using a Monte-Carlo method similar to that described in § 9.4.1.

Profile Extraction

The SZ profile is derived as a radial average of the data and errors are estimated using the method of Halverson et al. (2008). In order to combine the SZ and X-ray data sets, the X-ray raw mosaic is smoothed to the APEX-SZ resolution of $1'$. Effects of the XMM point spread function (PSF) and its variation over the field are negligible compared to the APEX-SZ beam and are not considered. An X-ray source mask is used to remove the numerous AGN in the field. A count profile is then extracted from the background subtracted mosaic and corrected for the local exposure time, thus converting to surface brightness. The Poisson error bars on the counts profiles are re-scaled accordingly. Since the background and source counts in each annulus are large, the noise can be considered as Gaussian which justifies the direct background subtraction. The centroid position from the best-fit isothermal beta model to the X-ray data is taken to be the common center in the X-ray/SZ joint analysis because of the much better signal-to-noise ratio in the X-ray map.

Mass Estimation Method

Using the SZ and X-ray measurements, the gas mass within a certain radius can be estimated. Total masses can be estimated under the additional assumption of hydrostatic equilibrium. Thus the gas-to-mass ratio as a function of radius can be computed.

Computing the gas mass and total mass profiles from isothermal β models is straightforward (e.g. LaRoque et al. 2006). The gas mass is obtained directly from the electron density profile as

$$M_{\rm gas}(< r) = 4\pi \; \mu_e n_e(0) m_p D_A^3 \int_0^{r/D_A} \left(1 + \frac{\theta^2}{\theta_c^2}\right)^{-3\beta/2} \theta^2 {\rm d}\theta, \tag{9.7}$$

where μ_e is the mean molecular weight per electron, assumed to be equal to 1.17 (taking cosmic abundances of H and He). For the non-isothermal analysis, the de-projected electron density profile is used to compute the gas mass directly as $\rho_{\rm gas}(r) = \mu_e m_p n_e(r)$.

The total mass, $M_{\rm total}$, is obtained by solving the hydrostatic equilibrium (HSE) equation, assuming spherical symmetry, as

$$M_{\rm total}(< r) = -\frac{k_{\rm B} T_e(r) \; r}{G \mu m_p} \left[\frac{d \ln n_e(r)}{d \ln r} + \frac{d \ln T_e(r)}{d \ln r}\right]. \tag{9.8}$$

In the isothermal case, the simple analytic form

$$M_{\rm total}(< r) = \frac{3\beta \; k_{\rm B} T_e}{G \mu m_p} \frac{r^3}{r^2 + r_c^2} \tag{9.9}$$

obtained from Eqn. (9.8) (e.g. Grego et al. 2001) can be used, while for the non-isothermal modeling Eqn. (9.8) must be solved directly. The gas mass fraction is in both cases computed as $f_{\rm gas}(< r) = M_{\rm gas}(< r)/M_{\rm total}(< r)$.

9.5.2 Systematics

Deconvolution and Filter Function

The dominating systematic effect in the non-parametric de-projection analysis comes from uncertainties in the de-convolved SZ map. To address this issue, a series of simulations similar to those presented in § 6.5.3 are carried out, passing artificial models through the reduction pipeline. While in § 6.5.3 it was considered only how the signal is affected by the pipeline in terms of fitting a parametric function out to a certain radius using the transfer function, systematic effects from using the transfer function to *deconvolve* the map must be considered here. Lacking a more complete model of the cluster emission, the spherical β model is again used, and the best-fit parameters from section 9.4 are varied within their 1σ errors to test the robustness of the final result. After passing the models through the pipeline, the resulting maps are de-convolved using the transfer function. The resulting profiles are then compared with the input models. While the systematic errors estimated from this method are comparable to the random errors on the SZ profile inside r_{500}, the signal is systematically lowered by as much as 40% of the input signal at r_{200}, indicating that the results are likely to be highly unreliable at this radius. It should be stressed that these error estimates are only meaningful in the context of the isothermal model. They are justified, however, by the results of section 9.4, which indicate that this model indeed provides a very reasonable fit to the SZ data of A2163 out to r_{500}.

Note that, in contrast to the isothermal analysis, there is no attempt to *correct* for this systematic. Instead, it is treated as an added uncertainty in the SZ profile.

Primary CMB and Galactic Dust

The systematic uncertainties from primary CMB anisotropies and galactic dust are estimated using methods analogous to those described in § 9.4.3. Although the contributions are found to be small compared to the effects of the deconvolution, the incurred uncertainties are included in the subsequent analysis.

9.5.3 Results of the Non-Isothermal Modeling

Density and Temperature Profiles

The radial profiles of the ICM density and temperature, obtained from equations 9.5 and 9.6, are shown in Figure 9.4. The results give a slight indication of a drop in temperature within r_{500}, where the systematic errors on the SZ profile are expected to be small (§ 9.5.2). A drop in temperature beyond this radius is expected both from theory (e.g. Frenk et al. 1999) and numerical simulations of clusters (e.g. Roncarelli et al. 2006, Hallman et al. 2007). The current results are not statistically significant enough to reliably indicate the existence of such a drop in Abell 2163, particularly in the light of large systematics at the relevant radii.

The density profile shows very little deviation from an isothermal β model inside r_{500} (roughly 1500 kpc), which is expected since the density values are mostly constrained by the X-ray surface brightness map. In the [0.5-2] keV energy band the X-ray surface brightness depends weakly on the gas temperature; for this reason the de-projected density profile using this band has a weak dependence on temperature variations. Beyond r_{500} the density drops more quickly than predicted from the isothermal β model. Inside r_{500} the temperature can be fitted with a constant (i.e. isothermal) value, at 9.6 ± 0.3 keV, marked by the horizontal dashed line in Fig. 9.4. Inside r_{2500} the best-fit isothermal value is 10.0 ± 0.4 keV.

To compare the results with spectroscopic temperature profiles derived from X-ray data alone, the mean weighted value of the gas temperature is computed along the line of sight as $T_{\mathrm{proj}} \equiv \int WTdV \ / \int WdV$, where T is the de-projected gas temperature and W is the weight function. As expected, the effect of projection is small compared to the errors in the temperature profile. Two different weighing schemes are used: the standard emission weight with $W = n^2\Lambda(T)$ (using $\Lambda(T) \propto T^{-1/6}$ as discussed earlier), and the weighing for a "spectroscopic-like" temperature as discussed by Mazzotta et al. (2004), using $W = n^2 T^{-3/4}$. The difference between these two weighing schemes is negligible, as can be expected considering the slowly varying temperature profile of A2163. The projected temperatures are consistent, within the stated uncertainties, with those derived from the spectroscopic X-ray measurements. A clear signature of a drop in temperature in the core region of the cluster (if present) is not expected to be seen, given the resolution and uncertainly of the current APEX-SZ measurement.

Gas mass and total mass

The mass analysis is limited to within r_{500} (approximately 1500 kpc) due to the large systematic uncertainties at the outer radii. The results are shown in Figure 9.6. The errors in the total mass and gas mass fraction profiles reflect the combined random and systematic errors in the present analysis.

The cumulative mass profile obtained from the temperature and density profiles, under the assumption of HSE with spherical symmetry, is in good agreement with the weak-lensing mass estimates obtained in previous studies (Squires et al. 2007), and extends the mass measurement to r_{500}. The cumulative gas mass fraction f_{gas} profile from the best-fit β model is consistent with a previous SZ-only analysis inside r_{2500} (LaRoque et al. 2006), which is approximately

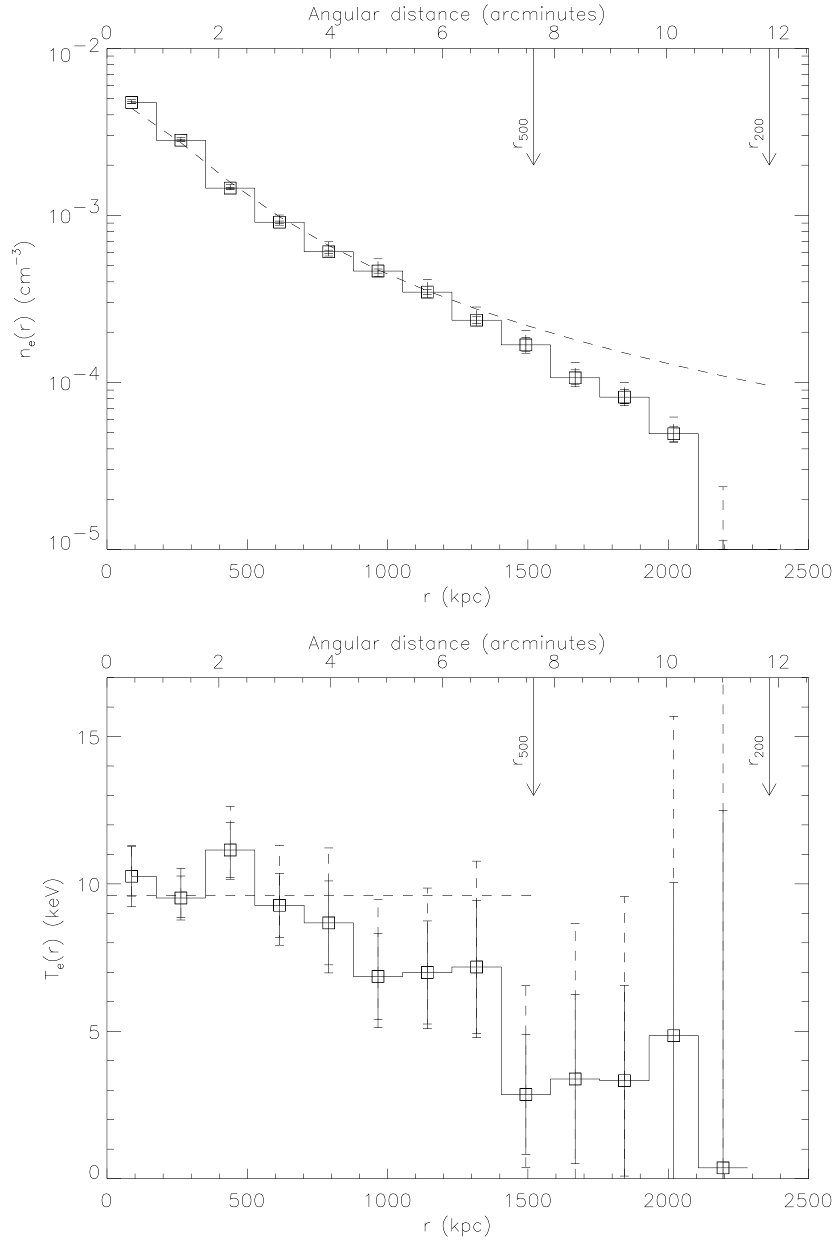

Figure 9.4: *Top:* De-projected radial density profile from X-ray (XMM-Newton) and APEX-SZ data. The dashed line is the SZ derived spherical β profile ($\beta = 0.70$ and $\theta_c = 98''$), normalized to the derived central electron density value. *Bottom:* De-projected temperature profile. The horizontal dashed line shows the best-fit isothermal value of 9.6 ± 0.3 keV within r_{500} ($\sim$7.6$'$). Vertical arrows in both plots mark the estimated values of r_{200} and r_{500}. Dashed error bars are derived including the systematic effects discussed in section 9.5.2.

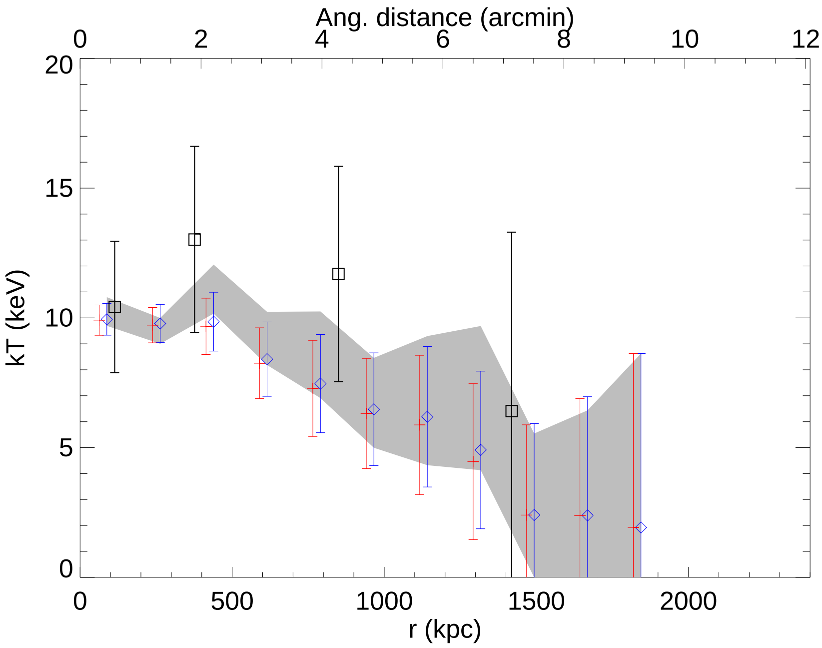

Figure 9.5: Comparison of the projected radial temperature profile with spectroscopic X-ray measurements (Markevitch & Vikhlinin 2001, black squares). The grey shaded region shows the de-projected temperature profile from Figure 9.4. Two different weighing schemes are used to derive the projected temperature: standard emission weight (blue diamonds) and the "spectroscopic-like" weight discussed by Mazzotta et al. (2004) (red crosses, slightly shifted in the distance axis).

25% lower than what is predicted from the X-ray/SZ joint β fit value of the same work. This bias may partly be the result of gas clumping near the center of this merging system (e.g. Mathiesen et al. 1999). The results from the de-projection analysis match the isothermal gas mass fraction values throughout, except at the very center of the cluster.

It should be noted that the plotted mass and gas mass fractions are cumulative functions, and hence their values in the outer bins are correlated with the data in bins closer to the center. Furthermore, the errors in $f_{\rm gas}$ are derived from the errors in the total mass and gas mass profiles, which are not independent. For these reasons, the errors in $f_{\rm gas}$ are strongly correlated.

9.6 Constraints from the SZ spectrum

To compare the SZ decrement/increment values at different frequencies, they are written in terms of the relative change to the background CMB intensity, as described in chapter 2. The intensity shift is related to a change in thermodynamic temperature by

$$\Delta B_\nu \;=\; B_0 \; h(x) \; \Omega_{\rm beam} \, \frac{\Delta T}{T_{\rm CMB}}, \tag{9.10}$$

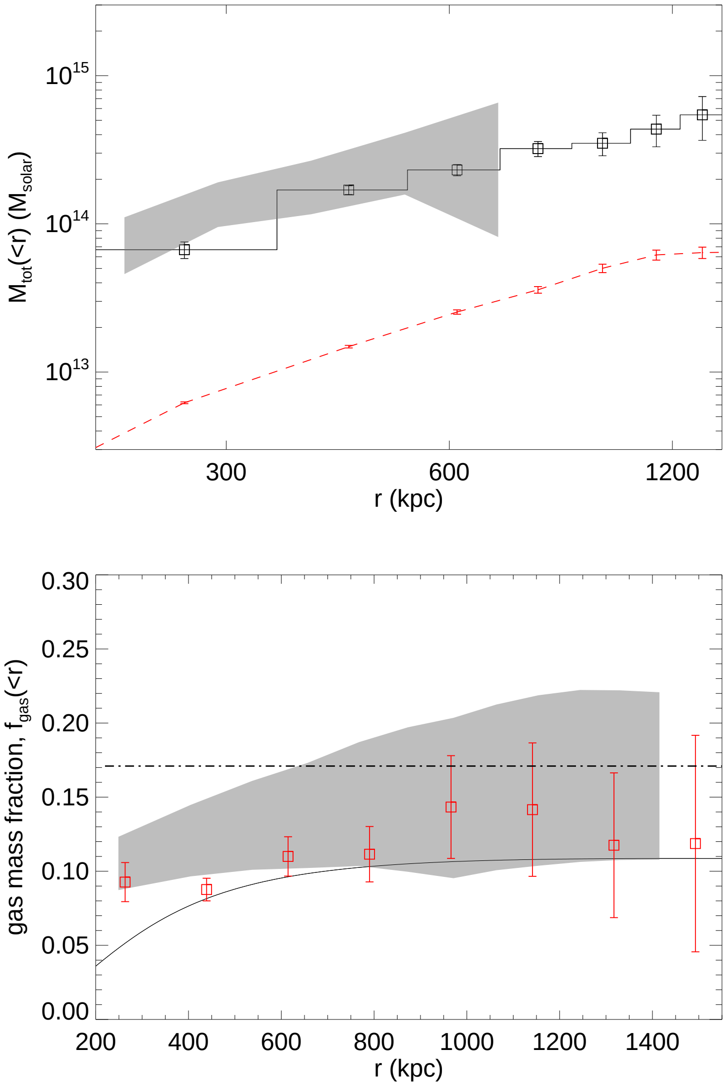

Figure 9.6: *Top:* Gas mass and total mass in Abell 2163 within r_{500} (∼1500 kpc), obtained from the de-projected density and temperature profiles. The total mass is computed under the assumption of hydrostatic equilibrium. The solid line shows the total mass and the dashed line the gas mass. The shaded region indicates the weak-lensing mass profile from Squires et al. (1997). *Bottom:* The gas mass fraction in A2163. The error bars indicate the estimates from the non-isothermal analysis, and the solid line is the gas mass fraction computed using the best-fit isothermal β model to the SZ data. The shaded region represents the results of the X-ray analysis of Squires et al. (1997), and the horizontal dot-dashed line represents the cosmic baryon fraction from the WMAP 5-year result (Dunkley et al. 2008).

where $x \equiv h\nu/kT_{\rm CMB}$, $B_0 \equiv 2(kT_{\rm CMB})^3/(hc)^2$, $h(x)$ is given by Eqn. (2.9) and $\Omega_{\rm beam}$ is the equivalent solid angle of the instrument beam (cf. the equations of § 2.2). The total change of intensity is written as the sum of the thermal and kinematic components of the SZ as

$$\Delta B_\nu \;=\; \Delta B_\nu^{\mathrm{T}} \;+\; \Delta B_\nu^{\mathrm{K}}. \tag{9.11}$$

Using the results of Sazonov & Sunyaev (1998), the two components are approximated by

$$\Delta B_\nu^{\mathrm{T}} = B_0 \; y \; f(x) \;\; [(-4 + F) + \delta_\times + \delta_T] \tag{9.12}$$

and

$$\Delta B_\nu^{\mathrm{K}} = -B_0 \; y \; f(x) \; (m_e c^2/k_{\mathrm{B}} T_e) \; \frac{v_r}{c}, \tag{9.13}$$

with v_r the radial (line-of-sight) peculiar velocity, which as usual is defined to be positive for a receding cluster. These equations include relativistic corrections to third order in $k_{\mathrm{B}}T_e/m_e c^2$. The term δ_T in Eqn. (9.12) is the correction due to temperature only, $\delta_\times$ is the cross-term between velocity and temperature, and $F \equiv x \coth(x/2)$. Higher order relativistic corrections are negligible given the precision of the current measurements. The Comptonization parameter y is defined by Eqn. (2.5). For the purpose of fitting the SZ spectrum, the Comptonization is parameterized in terms of its central value, y_0 (cf. chapter 8), allowing for a simple model where different resolutions can be accounted for. All spectral data are obtained with azimuthally symmetric fits using the isothermal β model, and accounting for beam dilution at each frequency. For APEX-SZ and LABOCA, the central decrement/increment values, derived from the spherical isothermal modeling of section 9.4 and corrected for dust contamination, are used. All data used for the fit to the SZ spectrum are given in Table 9.2.

Due to the degeneracies between velocity, temperature and Comptonization (discussed in the previous chapter), the present data is not sufficient for a simultaneous constraint of all three parameters. Instead, the ICM temperature is fixed to 9.6 keV from the joint X-ray and SZ analysis of section 9.5, and a least squares fit is performed in y_0 and v_r. These parameters are also fit using alternative values of the temperature in the range 8-14 keV.

To estimate the errors in the fitted parameters, a Monte Carlo simulation is performed, in which 10,000 artificial data sets are created from the actual spectral data, adding random Gaussian offsets with the amplitude of the statistical noise at each frequency. To model the effect of the systematics, random offsets from the most important systematic components from section 9.4.3 are also added, with the proper correlations between the different frequencies taken into account. Dust and primary CMB signals are scaled to the estimated levels derived in section 9.4 at 150 and 345 GHz and to the levels derived by LaRoque et al. (2002) at the other frequencies. To account for primary calibration uncertainties, a 5% calibration uncertainty is assumed across the spectrum.

The resulting error estimates, including systematics, are shown in Figure 9.7. The fitted radial velocity of the cluster is consistent with zero, in agreement with and marginally improving the constraints of LaRoque et al. (2002). Specifically, $v_r = -140 \pm 460$ km/s and $y_0 = 3.42 \pm 0.32 \times 10^{-4}$, excluding systematic uncertainties. The fit is dominated by random noise; including the systematic errors in the modeling increases the error in y_0 by 12% and in v_r by 18%. The SZ spectra resulting from the various fits are indicated in Figure 9.8.

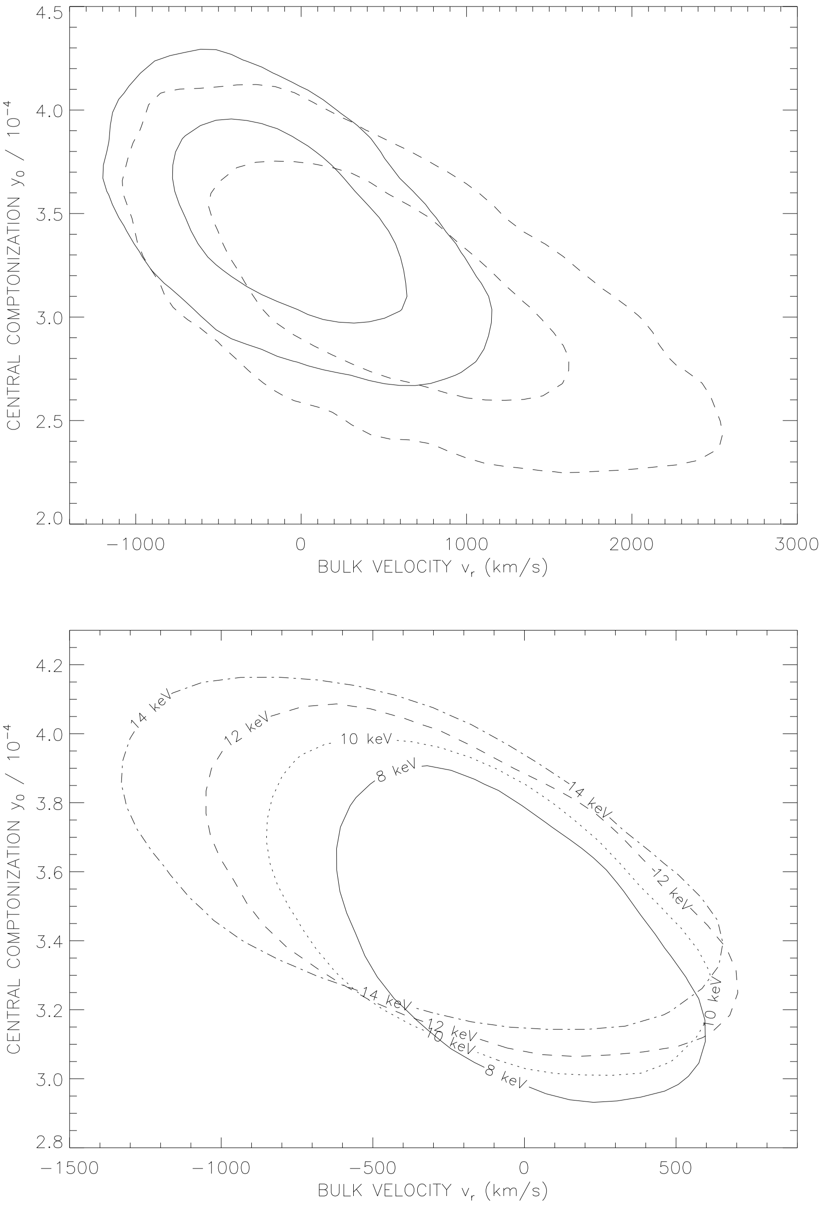

Figure 9.7: Constraints in the $v_r - y_0$ parameter space for Abell 2163 with priors on the ICM temperature, including systematic uncertainties. *Top:* solid contours indicate the 68% and 95% confidence regions using all available data and assuming $kT_e = 9.6$ keV. The dashed contours correspond to excluding the present (APEX-SZ and LABOCA) measurements. *Bottom:* 68% confidence regions for a range of ICM temperatures (indicated) using all available data.

Table 9.2: SZ decrement/increment measurements used for the spectral fit.

Wavelength (mm)	Instrument	ΔI (MJy sr^{-1})
10	OVRO/BIMA[1]	-0.043 ± 0.005 [4]
2.1	SuZIE[2]	-0.342 ± 0.033 [3,4]
2.0	APEX-SZ	-0.317 ± 0.035
1.4	SuZIE[2]	-0.093 ± 0.069 [3,4]
1.4	SuZIE[2]	0.266 ± 0.095 [3,4]
0.86	LABOCA	0.633 ± 0.094

[1] LaRoque et al. (2002)
[2] Holzapfel et al. (1997)
[3] dust-corrected intensities from LaRoque et al. (2002)
[4] calibration corrected according to Hill et al. (2008)

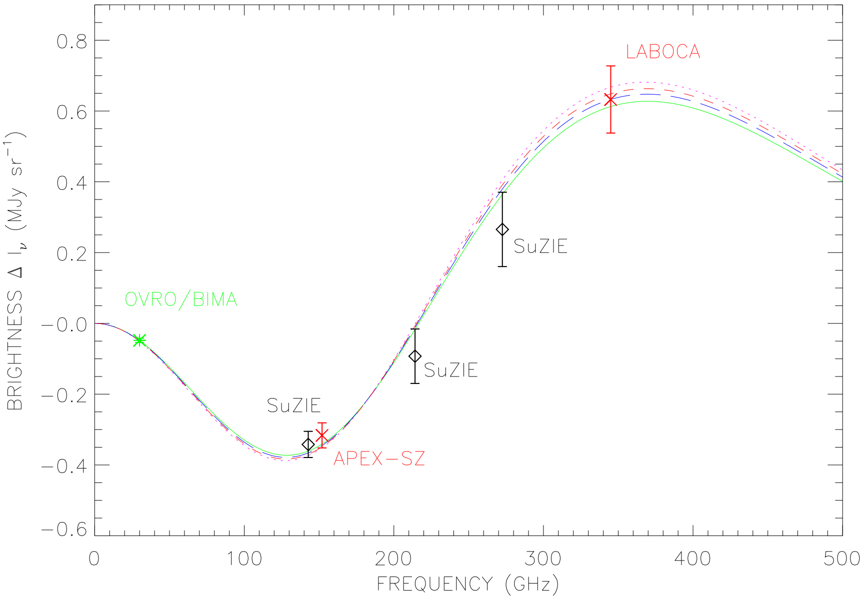

Figure 9.8: SZ spectrum of Abell 2163 (points) and best-fit models using different priors on the ICM temperature: 8 keV (solid line), 10 keV (long-dashed line), 12 keV (short-dashed line) and 14 keV (dotted line).

9.7 Conclusions

1. SZ maps of the galaxy cluster Abell 2163 at two frequencies have been presented, showing the SZ decrement at 150 GHz from observations with the APEX-SZ bolometer camera, and the SZ increment at 345 GHz from observations with the LABOCA bolometer camera. The 345 GHz measurement is the highest resolution SZ image for this cluster to date, and the first large-area ($> 10'$) imaging of a galaxy cluster at sub-mm wavelengths.

2. An isothermal modeling of the SZ yields results consistent with the X-ray derived isothermal model fits, implying that the large-scale properties of the cluster, under the assumption of spherical symmetry, are well represented by such models.

3. Using the APEX-SZ map in conjunction with XMM-Newton X-ray data, de-projected radial density and temperature profiles of the ICM are derived under the assumption of spherical symmetry. Inside r_{500}, the de-projected temperature profile is consistent with an isothermal value of 9.6 ± 0.3 keV. There is an indication of a drop in temperature at larger radii, but the detection is not firm given the combination of statistical and systematic errors at radii beyond r_{500}. The *re*-projected temperature profile is found to be consistent, within statistical errors, with the X-ray spectroscopic measurements of Markevitch & Vikhlinin (2001).

4. The total mass profile of the cluster is obtained under the assumption of hydrostatic equilibrium. The resulting profile agrees well with the weak-lensing mass profiles from previous works (Squires et al. 1997, Radovich et al. 2008), and extends the profile out to r_{500}.

5. The gas mass and the fraction of baryonic mass obtained from the de-projected density and temperature profiles are consistent with the SZ-only isothermal analysis of LaRoque et al. (2006), but approximately 25% lower than what is derived from X-ray measurements only. In particular, a significant increase in the baryon fraction from r_{2500} to r_{500} of the cluster is not seen.

6. Using isothermal fits to the LABOCA and APEX-SZ measurements, the line-of-sight peculiar velocity of the cluster and the central optical depth to inverse Compton scattering are derived, using the temperature obtained from the de-projection analysis. A peculiar velocity $v_r = -140 \pm 460$ km/s and a central Comptonization $y_0 = (3.42 \pm 0.32) \times 10^{-4}$ are found.

Chapter 10

Conclusion

Two years of observations of the Sunyaev-Zel'dovich (SZ) effect with the APEX-SZ bolometer array on the APEX telescope have been summarized. Crucial concepts leading up to a meaningful interpretation of the results have been considered; in particular, contaminants have been discussed, and the analysis of bolometer data has been described.

Through a simulated SZ survey at 150 GHz, the effects of numerous contaminants to the signals from clusters of galaxies have been estimated. Although the sub-mm background is not expected to contribute systematically to SZ measurements (except in very rare cases), the source population sets a strict limit on sensitivity around $5 - 10$ μK by acting as a source of excess noise that cannot be integrated down. The absolute level of the sub-mm background is poorly constrained at 150 GHz, but better constraints are foreseen with upcoming APEX-SZ observations of fields that already have deep sub-mm data. A project is in progress to statistically constrain the spectral slopes of radio point sources, which can potentially offset the SZ decrement. The volume averaged radio luminosity function has long been known to exhibit a redshift evolution. The present study has for the first time shown a similar evolution in galaxy cluster environments, up to a redshift of $z = 0.3$. It has also been found that the source density profile is much narrower than previously believed, even after taking into account that the cluster center in an optically selected cluster often coincides (by definition) with the brightest cluster galaxy (BCG). While the luminosity and number density evolutions presented in this thesis are relatively insensitive to the normalization of the chosen cluster radius, they rely heavily on the adaptive radius measure computed from the optical richness parameter.

The APEX-SZ and LABOCA (large APEX bolometer camera) bolometer arrays have been described, and it has been discussed how different scan strategies can be used in recovering emission on different spatial scales. The basic steps in characterizing the basic properties (array parameters) of a bolometer array have also been described.

The point source transfer function has been discussed as a means to model the emission of sources, in particular clusters of galaxies. It has been shown conclusively, using simulated sources, that a "linear" reduction scheme can be constructed, which preserves the property that the signal in the reduced map can be modeled as the sky signal convolved with the transfer function. The transfer function is not a point-spread function in the traditional sense, since it does not necessarily integrate to zero; its purpose is to not only quantify the brightness redistribution due to the instrument beam, but also the effects of the data reduction, which generally do not conserve integrated flux.

From a sample of thirteen clusters of galaxies targeted in the first two years of science observations with APEX-SZ, nine have been detected at high significance and modeled assuming isothermality. In addition, one marginal detection of a non-targeted cluster has been presented. The results of the isothermal analysis are in agreement with the predictions from X-ray measurements (XMM-Newton). Although the cluster yield after nearly two years of observation with APEX-SZ is much lower than expected, the instrument has been demonstrated as capable of ground-breaking science in detailed SZ measurements of massive clusters. In particular, this has been demonstrated for the Bullet cluster (see Halverson et al. 2008 for details) and in this thesis for the cluster A2163, for which a non-isothermal model has been presented. For the first time, SZ and X-ray data have been used jointly for a non-parametric de-projection of the three-dimensional structure of a galaxy cluster, albeit assuming spherical symmetry. The fact that the results are in overall agreement with those of X-ray analyses and weak lensing measurements alone, shows the usefulness of the method. Its application to future observations of relaxed clusters is foreseen.

Appendix A

Correction Factor from Rayleigh-Jeans to Thermodynamic Temperature

In radio astronomy, the *brightness temperature* is the temperature corresponding to a given intensity (or brightness), B_ν, if inserted to the Rayleigh-Jeans (RJ) relation:

$$B_\nu = \frac{2\nu^2 k_B T_b}{c^2}. \tag{A.01}$$

The definition couples a temperature to a given brightness at a given frequency.

Although the RJ approximation does not hold at low temperatures (as for the CMB), the brightness temperature is still a valid measure of brightness through this definition. We seek a conversion factor to easily go from a small change in brightness temperature due to the SZ effect to actual thermodynamic temperature, such that the change in *thermodynamic* temperature from the SZ effect can be written

$$\Delta T_{\text{thermal}} = \mathcal{F}(x)\frac{c^2}{2k_B\nu^2}\Delta B_\nu, \tag{A.02}$$

i.e. we seek the factor $\mathcal{F}(x)$.

Differentiating (A.01) with respect to T_b yields

$$\frac{\partial B_\nu}{\partial T_b} = \frac{2\nu^2 k_B}{c^2}, \tag{A.03}$$

which in the case of a small but finite temperature change ΔT_b we will write as

$$\Delta B_\nu = \frac{2\nu^2 k_B}{c^2}\Delta T_b. \tag{A.04}$$

We will now carry out the same differentiation on the brightness expressed in terms of thermodynamic temperature, given by the Planck formula:

$$B_\nu = \frac{2h}{c^2}\frac{\nu^3}{e^{\frac{h\nu}{k_B T}} - 1}. \tag{A.05}$$

The derivative of this equation with respect to the temperature T can be written, using the chain rule and making the substitution $x = h\nu/k_B T$,

$$\frac{\partial B_\nu}{\partial T} = \frac{\partial B_\nu}{\partial x}\frac{\partial x}{\partial T}, \tag{A.06}$$

where the derivatives are

$$\frac{\partial B_\nu}{\partial x} = \frac{2h\nu^3}{c^2}\frac{e^x}{\left(e^x - 1\right)^2}; \tag{A.07}$$

$$\frac{\partial x}{\partial T} = -\frac{h\nu}{k_B T^2}, \tag{A.08}$$

and thus

$$\frac{\partial B_\nu}{\partial T} = \frac{2\nu^2 k_B}{c^2}\frac{x^2 e^x}{\left(e^x - 1\right)^2}. \tag{A.09}$$

In the finite case, the thermodynamic counterpart of (A.04) is now

$$\Delta B_\nu = \frac{2\nu^2 k_B}{c^2}\frac{x^2 e^x}{\left(e^x - 1\right)^2}\Delta T, \tag{A.010}$$

where we recognize the first term from the definition of the brightness temperature. In terms of the latter, a change in thermodynamic temperature can now be expressed as

$$\Delta T = \Delta T_{\text{thermodynamic}} = \mathcal{F}(x)\Delta T_b, \tag{A.011}$$

with the correction factor

$$\mathcal{F}(x) = \frac{\left(e^x - 1\right)^2}{x^2 e^x}. \tag{A.012}$$

References

Abell, G. O., 1958, ApJS, 3, 211

Abell, G. O., Corwin, H. G., Jr., Olowin, R. P., 1989, ApJS, 70, 1

Afshordi, N., Lin, Y.-T., Nagai, D., Sanderson, A. J. R., 2007, MNRAS, 378, 293

Aghanim, N., Hansen, S. H., Pastor, S., Semikoz, D. V., 2003, JCAP, 5, 7

Aghanim, N., Hansen, S. H., Lagache, G., 2005, A&A, 439, 901

Allen, S. W., 2000, MNRAS, 296, 392

Allen, S. W., Schmidt, R. W., Fabian, A. C., 2001, MNRAS, 328, L37

Allen, S. W., Schmidt, R. W., Fabian, A. C., 2002, MNRAS, 334, 11

Allen, S. W., Schmidt, R. W., Ebeling, H., et al., 2004, MNRAS, 353, 457

Alpher, R. A., Bethe, H., Gamow, G., 1948, Phys. Rev., 73, 803

Ameglio, S., Borgani, S., Pierpaoli, E., Dolag, K., 2007, MNRAS, 382, 397

Andreani, P., Pizzo, L., dall'Oglio, G., et al., 1996, ApJL, 459, 49

Andreon, S., Willis, J., Quintana, H., 2004, MNRAS, 353, 353

Andreon, S., Valtchanov, I., Jones, L. R., et al., 2005, MNRAS, 359, 1250

Astier, P., Guy, J., Regnault, N., et al., 2006, A&A, 447, 31

Bahcall, N. A., Lubin, L. M., ApJ, 426, 513

Bartelmann, M., Schneider, P., 2001, Phys. Reports, 340, 291

Battistelli, E. S., De Petris, M., Lamagna, L., et al., 2002, ApJL, 580, 101

Battye, R. A., Weller, J., 2003, Phys. Rev. D, 68, 3506

Becker, R. H., White, R. L., Helfand, D. J., 1995, ApJ, 450, 559

Bennett, C. L., Banday, A. J., Gorski, K. M., et al., 1996, ApJL, 464, 1

Bennett, C. L., Hill, R. S., Hinshaw, G., et al., 2003, ApJS, 148,1

Benson, B. A., Church, S. E., Ade, P. A. R., et al., 2003, ApJ, 592, 674

Benson, B. A., Church, S. E., Ade, P. A. R., et al., 2004, ApJ, 617, 829

Bertin, E., Arnouts, S., 1996, A&AS, 117, 393

Bertoldi, F., 2000, *Correlated Noise Global Extraction.* MPIfR Internal memo

Best, P. N., von der Linden, A., Kauffmann, G., et al., 2007, MNRAS, 379, 894

Birkinshaw, M., Laing, R., Scheuer, P., Simon, A., 1978, MNRAS, 185, 245

Birkinshaw, M., 1999, Phys. Reports, 310, 97

Böhringer, H., Voges, W., Huchra, J. P., et al., 2000, ApJS, 129, 435

Böhringer, H., Schuecker, P., Guzzo, L., et al., 2004, A&A, 425, 367

Bolzonella, M., Miralles, J.-M., Pello, R., 2000, A&A, 363, 476

Bonamente, M., Joy, M., et al. 2008, ApJ, 675, 106

Borys, C., Chapman, S., Scott, D., 1999, MNRAS, 308, 527

Borys, C., Chapman, S., Halpern, M., Scott, D., 2003, MNRAS, 344, 385

Calabretta, M. R., Greisen, E. W., 2002, A&A, 395, 1077

Carlberg, R. G., Yee, H. K. C., Ellingson, E., 1997, ApJ, 478, 462

Carlstrom, J. E., Holder, G. P., Reese, E. D., 2002, ARA&A, 40 643

Carlstrom, J. E., 2006, ASPC, 356, 35

Cash, W., 1979, ApJ, 228, 939

Cavaliere, A., Fusco-Femiano, R., 1976, A&A, 49, 137

Cavaliere, A., Fusco-Femiano, R. 1978, A&A, 70, 677

Clowe, D., Bradac, M., Gonzalez, A. H., et al., 2006, ApJL, 648, 109

Coble, K., Bonamente, M., Carlstrom, J. E., et al., 2007, AJ, 134, 897

Coles, P., Luccin, F., 2002, Cosmology - *The Origin and Evolution of Cosmic Structure.* Chichester: John Wiley & Sons

Condon, J. J., 1984, ApJ, 287, 461

Condon, J. J., Cotton, W. D., Greisen, E. W., et al., 1998, AJ, 115, 1693

Condon, J. J., Cotton, W., Broderick, J., 2002, ApJ, 124, 675

Cooray, A. R., Grego, L., Holzapfel, W. L., et al., 1998, AJ, 115, 1388

Da Silva, A. C., Barbosa, D., Liddle, A. R., Thomas, P. A., 2000, MNRAS, 317, 37

Da Silva, A. C., Barbosa, D., Liddle, A. R., Thomas, P. A., 2001, MNRAS, 326, 155

Dahle, H., Kaiser, N., Irgens, R. J., et al., 2002, ApJS, 139, 313

David, L. P., Jones, C., Forman, W., 1995, ApJ, 445, 578

De Filippis, E., Sereno, M., Bautz, M. W., Longo, G., 2005, ApJ, 625, 108

De Grandi, S., Böhringer, H., Guzzo, L., et al., 1999, ApJ, 514, 148

De Petris, M., D'Alba, L., Lamagna, L., et al., 2002, ApJL, 574, 119

Demarco, R., Rosati P., Lidman C., et al., 2007, ApJ, 663, 164

Desert, F.-X., Benoit, A., Gaertner, S., et al., 1998, NewAR, 3, 655

Dobbs, M., Halverson, N. W., et al., 2006, NewAR, 50, 960

Dunkley, J., Komatsu, E., et al. 2008, arXiv:0803.0586

Dunlop, J. S., Peacock, J. A., 1990, MNRAS, 247, 19

Edge, A. C., 1991, MNRAS, 250, 103

Eisenstein, D. J., Hu, W., Tegmark, M., 1999, ApJ, 518, 2

Elbaz, D., Arnaud, M., Böhringer, H., 1995, A&A, 293, 337

Enoch, M. L., Young, K. E., Glenn, J., et al., 2006, ApJ, 638, 293

Ettori, S., 2000, MNRAS, 311, 313

Evrard, A. E., 1997, MNRAS, 292, 289

Fabbri, R., 1981, Ap&SS, 77, 529

Feretti, L., Brunetti, G., Giovannini, G., Kassim, N., Setti, G., 2004, A&A 423, 111

Fixsen, D. J., Cheng, E. S., Gales, J. M., et al., 1996, ApJ, 473, 576

Freedman, W. L., Madore, B. F., Gibson, B. K., et al., 2001, ApJ, 553, 47

Frenk C. S., White, S. D. M., Bode, P. et al. 1999, ApJ, 525, 554

Gear, W. K., Cunningham, C. R., 1995, ASPC, 75, 215

Geisbüsch, J., Kneissl, R., Hobson, M., 2005, MNRAS, 360, 41

Gildemeister, J. M., Lee, A. T., Richards, P. L., 1999, App. Phys. Lett., 74, 868

Gladders, M. D., Yee, H. K. C., 2000, AJ, 120, 2148

Gladders, M. D., Yee, H. K. C., 2005, ApJ, 157, 1

Glenn, J., Bock, J. J., Chattopadhyay, G., et al., 1998, Proc. SPIE, 3357, 326

Gorski, K. M., Hivon, E., Banday A. J., et al., 2005, ApJ, 622, 759

Govoni, F., Markevitch, M., et al., 2004, ApJ, 605, 695

Grego, L., Carlstrom, J. E., Reese, E. D., et al., 2001, ApJ, 552, 2

Griffin, M. J., Ade, P. A. R., Orton, G. S., et al., 1986, ICARUS, 65, 244
Griffin, M. J., Orton, G. S., 1993, ICARUS, 105, 537
Güsten R., Nyman, L. Å., Schilke, P., et al., 2006, A&A, 454, L13
Hallman, E. J., Burns, J. O., Motl, P. M., Norman, M. L., 2007, ApJ 665, 911
Halverson, N. W., Lanting T., et al., 2008, arXiv:astro-ph/0807.4208
Hansen, S. H., Pastor, S., Semikoz, D. V., 2002, ApJ 573, L69
Hansen, S. H., 2004, MNRAS 351, L5
Herbig, T., Lawrence, C. R., Readhead, A. C. S., Gulkis, S., 1995, ApJL, 449, 5
Hill, R. S., Weiland, J. L., et al., 2008, arXiv:astro-ph/0803.0570
Hoekstra, H., Franx, M., Kuijken, K., Squires, G., 1998, ApJ, 504, 636
Högbom, J. A., 1974, A&AS, 15, 417
Holdaway, M., Owen, F., Rupen, M., 1994, MMA Memo 123
Holdaway, M., Owen, F., 2005, ALMA Memo 520
Holder, G., Haiman, Z., Mohr, J. J., 2001, ApJL, 560, 111
Holder, G. P., 2004, ApJ, 602, 18
Holzapfel, W. L., Ade, P. A. R., Church, S. E., et al., 1997a, ApJ 481, 35
Holzapfel, W. L., Arnaud, M., Ade, P. A. R., 1997b, ApJ, 480, 449
Horellou, C., Nord, M., Johansson, D., Lévy, A., 2005, A&A, 441, 435
Hu, W., White M., 1997, ApJ, 479, 568
Hu, W., Dodelson S., 2002, ARA&A, 40, 171
Hu, W., Kravtsov A. V., 2003, ApJ, 584, 702
Huffenberger, K. M., 2005, NewAR, 10, 491
Irwin, J. A., Bregman, J. N., 2000, ApJ, 538, 543
Itoh, N., Kohyama, Y., Nozawa, S., et al., 1998, ApJ, 502, 7
Jenkins, A., Frenk, C. S., White, S. D. M., et al., 2001, MNRAS, 321, 372
Jones, C., Forman, W., 1984, ApJ, 276, 38
Jones, W. C., Ade, P. A. R., Bock, J. J, et al., 2006, NewAR, 50, 945
Joy, M., LaRoque, S., Grego, L., et al., 2001, ApJ, 551, L1
King, I., 1962, AJ, 67, 47
Kitayama, T., Suto, Y., 1996, ApJ, 469, 480
Kitayama, T., Komatsu, E., Ota, N., et al., 2004, PASJ, 56, 17
Knop, R. A., Aldering, G., Amanullah, R., et al., 2003, ApJ, 598, 102
Knox, L., Holder, G. P., Church, S. H., ApJ, 612, 96
Koester, B. P., McKay, T. A., Annis, J., et al., 2007, ApJ, 660, 239
Komatsu, E., Kiatayama, T., 1999, ApJL, 526, L1
Komatsu, E., Dunkley, J., Nolta, M. R., et al., 2008, arXiv:astro-ph/0803.0547
Kosowsky, A., 2006, NewAR, 50, 969
Kotov, O., Vikhlinin, A., 2006, ApJ, 641, 752
Kuo, C. L., Ade, P. A. R., Bock, J. J., et al., 2007, ApJ, 664, 687
Kreysa, E., Bertoldi, F., Gemuend, H.-P., et al., 2003, SPIE, 4855, 41
Lamarre, J. M., Giard, M., Pointecouteau, E., et al., 1998, ApJ, 507, 5L
Lanting, T., et al., 2007, *APEX-SZ Performance Summary*

LaRoque, S. J., Carlstrom, J. E., Reese, E. D., et al. 2002, arXiv:astro-ph/0204134

LaRoque, S. J., Joy, M., Carlstrom, J. E., et al., 2003, ApJ, 583, 559

LaRoque, S. J., Bonamente, M., Carlstrom, J. E., et al., 2006, ApJ, 652, 917

Ledlow, M., Owen, F., 1996, AJ, 112, 1

Lee, A. T., Richards, P. L., et al., 1996, Appl. Phys. Lett., 69, 1801

Lee, J., Suto, Y., 2004, ApJ, 601, 599L

Lin, Y.-T., Mohr, J., 2007, ApJS, 170, 71

Loeb, A., Refregier, A., 1997, ApJL, 476, 59

Luppino, G. A., Gioia, I. M., 1995, ApJL, 445, 77

Machalski, J., Godlowski, W., 2000, A&A, 360, 463

Markevitch, M., Vikhlinin, A., 2001, ApJ, 563, 95

Markevitch, M., 2006, in ESA Special Publ. vol. 604: *The X-ray Universe*, ed. Wilson A.

Mason, B. S., Myers, S. T., Readhead, A. C. S., 2001, ApJL, 555, 11

Massardi, M., De Zotti, G., 2004, A&A, 424, 409

Mathiesen, B., Evrard, A. E., Mohr, J., 1999, ApJ, 520, L21

Maurogordato, S., Cappi, A., Ferrari, C., et al., 2008, A&A, 481, 593

Mazzotta, P., Rasia, E., et al. 2004, MNRAS, 354, 10

Miller, C. J., Nichol, R. C., Reichart, D., et al., 2005, AJ, 130, 968

Mo, H. J., White, S. D. M., 2002, MNRAS, 336, 112

Motl, P. M., Hallman, E. J., Burns, J. O., Norman, M. L., 2005, ApJ, 623L, 63

Muders, D., et al., 2005, *Multi-Beam FITS Raw Data Format*, APEX-MPI-IFD-0002

Mullis, C. R., McNamara, B. R., Quintana, H., et al., 2003, ApJ, 594, 154

Myers, S. T., Baker, J. E., Readhead, A. C. S., et al., 1997, ApJ, 485, 1

Nolta, M. R., Dunkley, J., Hill, R., et al., 2009, ApJS, 180, 296

Nord, M., Basu, K., Pacaud, F., et al., 2008, arXiv:astro-ph/09032.2131

Novicki, M. C., Sornig, M., Henry, J. P., 2002, AJ, 124, 2413

Nozawa, S., Itoh, N., Kohyama, Y., 1998, ApJ, 507, 530

Ota, N., Mitsuda, K., 2004, A&A, 428, 757

Pacaud, F., Pierre, M., Adami, C., et al., 2007, MNRAS, 382, 1289

Partridge, R. B., 1995, *3K: The Cosmic Microwave Background Radiation*, Cambridge Univ. Press

Peebles, P. J. E., 1980, *The Large-Scale Structure of the Universe*, Princeton: Princeton Univ. Press

Peebles, P. J., Ratra, B., 2003, RvMP, 75, 559

Penzias, A. A., Wilson, R. W, 1965, ApJ, 142, 419

Perlman, E. S., Horner, D. J., Jones, L. R., et al., 2002, ApJS, 140, 265

Perlmutter, S., Aldering, G., Goldhaber, G., et al., 1999, ApJ, 517, 565

Peterson, J. B., Radford, S. J. E., Ade, P. A. R., et al., 2003, PASP, 115, 383

Pointecouteau, E., Giard, M., Barret, D., 1998, A&A, 336, 44

Pointecouteau, E., Giard, M., Benoit, A., et al., 2001, ApJ, 552, 42

Pratt, G. W., Arnaud, M., 2002, A&A, 394, 375

Press, W. H., 1978, ComAp, 7, 103

Press, W. H., Schechter, P., 1974, ApJ, 187, 425

Puchwein, E., Bartelmann M., 2006, A&A, 442, 405

Radovich, M., Puddu, E., Romano, A., et al., 2008, A&A, 487, 55

Reddy, N. A., Yun, M. S., 2004, ApJ, 600, 695

Reese, E. D., Mohr, J. J., Carlstrom, J. E., et al., 2000, ApJ, 533, 38

Reese, E. D., Carlstrom, J. E., Joy, M., et al., 2002, ApJ, 581, 53

Reichardt C. L., Ade, P. A. R., Bock, J. J., et al., 2009, ApJ, 694, 1200

Reiprich, T., 2001, PhD thesis

Reiprich, T., Hudson, D., et al., 2008, arXiv:astro-ph/0806.2920

Rajguru, N., Myers, S. T., Battye, R. A., et al., 2005, MNRAS, 363, 1125

Rephaeli, Y., 1995, ApJ, 445, 33

Roncarrelli, M., Ettori, S., Dolag, K., et al., 2006, MNRAS, 373, 1339

Rosati, P., Tozzi, P., Ettori, S., 2004, AJ, 127, 230

Ruhl, J. E., Ade, P. A. R., Carlstrom, J. E., et al., 2004, SPIE, 5498, 11

Sachs, R. K., Wolfe, A. M., 1967, ApJ, 147, 73

Sanders, J. S., Fabian, A. C., Taylor, G. B., 2005, MNRAS, 356,1022

Sarazin, C. L., 1988, *X-ray emission from clusters of galaxies*, Cambridge: Cambridge Univ. Press

Sazonov, S. Y., Sunyaev, R. A., 1998a, Astron. Lett., 24, 643

Sazonov, S. Y., Sunyaev, R. A., 1998b, ApJ, 508, 1

Schechter, P., 1976, ApJ, 203, 297

Schindler, S., Hattori, M., Neumann, D. M., Böhringer, H., 1997, A&A, 317, 646

Schlegel, D., Finkbeiner, D., Davis, M., 1998, ApJ, 500, 525

Schwan, D., Bertoldi, F., Cho, S., et al., 2003, NewAR, 47, 933

Schwarz, U. J., 1978, A&A, 65, 345

Scott, K. S., Austermann, J. E., Perera, T. A., et al., 2008, MNRAS, 385, 2225

Sehgal, N., Kosowsky, A., Holder, G., 2005, ApJ, 635, 22

Sereno, M., De Filippis, E., Longo, G., Bautz, M. W., 2006, ApJ, 645, 170

Sheth, R. K., Tormen, G., 1999, MNRAS, 308, 119

Silk, J., White, S., 1978, ApJ, 226L

Siringo, G., Weiss, A., Kreysa, E., et al., 2007, Msngr., 129, 2

Siringo, G., Kreysa, E., Kovacs, A., et al., 2009, arXiv:astro-ph/0903.1354

Smail, I., Ivison, R. J., Blain, A. W., 1997, ApJL, 490, 5

Smith, R., Brickhouse, N., et al., 2001, ApJ, 556, 91

Spergel, D. N., Verde, L., Peiris, H. V., et al., 2003, ApJS, 148, 175

Springel, V., White, M., Hernquist, L., 2001, ApJ, 549, 681

Squires, G., Neumann, D., et al., 1997, ApJ, 482, 648

Stanford, S. A., Romer, A. K., et al., 2006, ApJL, 646, 13

Staniszewski, Z., Ade, P. A. R., Aird, K. A., Benson, B. A., et al., 2008, arXiv:astro-ph/0810.1578

Stocke, J., Perlman, E. S., Gioia, I. M., Harvanek, M., et al., 1999, ApJ, 117, 1967

Struble, M. F., Rood, H. J., 1999, ApJS, 125, 35

Sunyaev, R. A., 1980, SvAL, 6, 213

Sunyaev, R. A., Zeldovich, Y. B., 1970a, Ap&SS, 7, 3
Sunyaev, R. A., Zeldovich, Y. B., 1970b, Ap&SS, 7, 20
Sunyaev, R. A., Zeldovich, Y. B., 1972, A&A, 20, 189
Tang, J., Fan, Z., 2003, ChJAA, 3, 191
Tegmark, M., 1995, arXiv:astro-ph/9511148
The, L. S., White, S. D. M., 1986, AJ, 92, 1248
Toffolatti, L., De Zotti, G., Argüeso, F., Burigana, C., 1999, ASPC, 181, 153
Tucker, W., Blanco, P., Rappoport, S., et al., 1998, ApJL, 496, 5
Tyson, J. A., Wenk, R. A., Valdes, F., et al., 1990, ApJL, 349, 1
Ulich, B. L., 1981, AJ, 86, 1619
Valtchanov, I., Pierre, M., Willis, J., et al., 2004, A&A, 423, 75
Viana, P. T. P., Liddle A. R., 1999, MNRAS 303, 535
Vikhlinin, A., Forman, W., Jones, C., 1999, ApJ, 525, 47
Voit, G. M., Evrard, A. E., Bryan, G. L., 2001, ApJL, 548, 123
Voit, G. M., 2004, arXiv:astro-ph/0410173
Voss, H., Bertoldi, F., Carilli, C., et al., 2006, A&A, 448, 823
Wang, L., Steinhardt, P. J., 1998, ApJ, 508, 483
Weiss, A., Kovacs, A., et al., 2008, A&A, 490, 77
White, D. A., 2000, MNRAS, 312, 663
White, D. A., Fabian, A. C., 1995, MNRAS, 273, 72
White, M., Scott, D., Silk, J., 1994, ARA&A, 32, 319
White, M., Hernquist, L., Springel, V., et al., 2002, ApJ, 579, 16
White, M., Majumdar, S., 2004, ApJ, 602, 565
Willis, J. P., Pacaud, F., Valtchanov, I., et al., 2005, MNRAS, 363, 675
Wilson, G. W., Aretxaga, I., Hughes, D., et al., 2008, arXiv:astro-ph/0803:3462
Wright, E. L., 1976, ApJ, 210, 250
Wright, E. L., 1979, ApJ, 232, 348
Yee, H. K. C., Ellingston, E., 2003, ApJ, 585, 215
York, D. G., Adelman, J., Anderson, J. E., Jr., et al., 2000, AJ, 120, 1579
Yoshikawa, K., Suto, Y., 1999, ApJ, 513, 549
Yuan, Q., Zhang, T.-J., Wang, B.-Q., 2008, ChJAA, 8, 671
Zaldarriaga, M., Seljak, U., 2000, ApJS, 129, 431
Zaroubi, S., Squires, G., de Gasperis, G., et al., 2001, ApJ, 561, 600
Zeldovich, Y. B., Sunyaev, R. A., 1969, Ap&SS, 4, 301
Zemcov, M., Halpern, H., Borys, C., et al. 2003, MNRAS, 346, 1179
Zhang, Y.-Y., Böhringer, H., Finoguenov, A., et al., 2006, A&A, 456, 55
Zwicky, F., 1933, AcHPh, 6, 110
Zwicky, F., 1937, ApJ, 86, 217